Real-Time Measurement of Wide-Area Near-Surface Ocean Current

by

©Samareh Attarsharghi

A dissertation submitted to the School of Graduate Studies

In partial fulfillment of the requirements for the degree of

Doctor of Philosophy in Electrical Engineering

Faculty of Engineering and Applied Science

Memorial University of Newfoundland

May 2017

St. John's, Newfoundland and Labrador

Abstract

Of all of the physical parameters of the ocean realm, the speed and direction of the movement of ocean water, otherwise referred to as ocean "current," is one of the most problematic to characterize. Currents influence the global climate, used for producing power, are crucial in determining the oil spill trajectories and ocean contaminant control, can either work against or with the movement of ships at sea and govern the movements of icebergs. Icebergs are a threat to offshore industries and marine transportations, particularly in places like the Northwest Atlantic, because of damages they can cause once they strike the oil platforms or ship hulls. They are steered by the near-surface current and not the surface current. Therefore, measurment of the real-time ocean currents at desired depths is valuable for the industries or researchers who are dealing with or studying the oceanographic data.

Ocean current measurment methods that are currently being employed for ocean monitorings, are not able to measure the real-time current at certain desired depths over a larg area of the ocean. Thus, the existing current measurement methods need improvements. Limitations of the existing methods are as follows. Acoustic dopler current profilers (ADCP), are one of the most popular methods employed by most of the industries dealing with the oceanograghy. ADCPs are capable of measuring the current at any desired depth; however, their measurement method is of a point nature and they cannot measure an area averaged current data. Other techniques such as high frequency radio detecting and ranging systems (HF-RADAR) are also used to measure the surface currents (down to 15 m). These shore-based current meters with radio antenna, follow the same premise of the ADCP. In other words their measurement is dependant on the Doppler effect to determine the direction and velocity of the currents; however, they are capable of evaluating

only the surface currents and not the near-surface currents (70-100 meter of depth is considered in this thesis as this is the depth oil structures are deployed in the Northwest Atlantic Ocean). Another group of instruments used for current measurement are floats and drifters which report their data to a centre device which is usually a satelite. The current data obtained with these instruments are fed into modeling systems, e.g. in (Chassignet, Hurlburt et al. 2006), for the ocean forcasting. The problems that exist with the available real-time current data from the satelite is that it is the very shallow current data (down to 15m that can be called surface). The data from other devices like floats is very sparse to include the horizontal information. Hence, Chassignet *et al.* use data assimilation of the past knowledge and ocean dynamics in order to predict the ocean features. Therefore, it is important to develop a method by which adequate data could be provided for the ocean prediction and modeling system. Thus, the focus of this thesis is on designing a method which is real-time and measures the near-surface current.

On the other hand, energy suplies to the instruments in open water is limited as they work mainly rely on batteries and it is difficult to access the instruments in harsh condition to replace the batteries. Moreover, in cold regions the solar power is very limitted and thus using solar cells is not practical. Therefore, in order to measure the ocean current in real time, a novel method along with a sustainable architechture design is being proposed in this dissertation. The new method is based on transit time with the difference that in transit time method waves need to travel in both directions; up- and down-stream. But with a modification in the newly designed architeture; which is adding an extra node in the center of the network's cells, sound waves need to travel on only one direction. This helps with saving a great amount of energy and covering a larger area in comparison with the networks which are developed using transit time method. Experimental results as well as simulations verify that the new proposed method is both efficient and practical.

Acknowledgements

Table of Contents

Co-authorship Statement

This thesis consists of three papers; two published and one in press. I am the first author in all of them and performed the study, development, design, experiments, data collection, data analysis, and interpretation of the results. I also performed all of the underwater simulations and analyses and finally, I prepared the draft of all of the manuscripts.

Contributions of the co-author, Dr. Vlastimil Masek, on the manuscripts are as below:

Dr. Masek provided guidance and supervision on the studies. He contributed insight into the synchronization of the nodes and cross correlation technique. Also Dr. Masek provided experimental supplies such as acoustic transducers, microcontrollers, WiFi boards and other instruments as well as the funding of the project. He also commented on the manuscripts and helped with the editing.

Chapter 1: Introduction

1.1 Introduction

A significant part of oceanographic research is concerned about the measurement of current. One of the pioneer researchers is Thomas Rossby who has been using underwater sound, in oceanographic instruments such as floats, for measuring and tracking ocean currents since 70's (Rossby and Webb 1970). His main interests have been the Gulf Stream (Fofonoff 1981) and Meddy (Peter M. D. 2001) (brief definition found in the Appendix). In his interview with *The Discovery of Sound in the Sea* (DOSTIS 2016) (descriptions found in the Appendix) he indicates that ocean features including the two above mentioned currents are highly structured features. As a result many efforts have been done on ocean current measurements and researchers have been trying to monitor the sea movements (NCOM n.d.; SmartAtlanticAlliance n.d.; NOAA n.d.F.) These measurements are especially useful for purposes such as oil spill mitigation (Cheng, Li et al. 2011; Liu, Weisberg et al. 2011; Mariano, Kourafalou et al. 2011; Ehrhardt 2015) or icebergs drift modeling (De Margerie 1986; Dmitriev and Nesterov 2007; Broström, Melsom et al. 2009; Eik and Gudmestad 2010; Hunke and Comeau 2011). Both deep circulation and surface currents of the ocean are considered in mitigation process of the oil spills (Liu, Weisberg et al. 2011), whereas icebergs are mainly driven by the near-surface shallow currents.

In the North Atlantic Ocean an accurate prediction of the iceberg trajectory is extremely important in order to prevent potential collisions. Movements of icebergs are specifically important because of the fact that ninety percent of the iceberg mass is under the water and is invisible. Hence it can easily strike floating objects in the sea, such as oil platforms and ships, and cause damages to them. Therefore, predicting the iceberg trajectories helps to avoid the collisions.

As authors in (Eik 2009; Turnbull, Fournier et al. 2015) indicate, main factors that drive the icebergs are the wave, wind and the ocean currents. As an example in Equation (1.1) Trurnbull formulates the force that is drifting the iceberg which is compromised of four elements: air draw ($\overrightarrow{F_a}$), water drag ($\overrightarrow{F_w}$), Coriolis force ($\overrightarrow{F_c}$) and water pressure gradient force ($\overrightarrow{F_{wp}}$). Mass of the water is represented by M and V is representing the velocity of the mass.

$$M\frac{d\vec{V}}{dt} = \overrightarrow{F_a} + \overrightarrow{F_w} + \overrightarrow{F_c} + \overrightarrow{F_{wp}} \tag{1.1}$$

Water drag is defined to be the sum of the forces water applies to the iceberg, and as it can be seen from the modeling, which is more or less the same across all literatures, water drag (current) plays an important role in the movements of the icebergs. Drag is a result of oceanic current and other factors; therefore, measurement of a real-time in-situ data of the current is very important for the iceberg trajectory modeling. However, reliable data of the current is hard to achieve as Turnbull and Eik report in (Turnbull, Fournier et al. 2015) and (Eik 2009). Also Chassignet *et al.* in (Chassignet, Hurlburt et al. 2006) use data assimilation and modeling in order to overcome the lack of current data. Therefore, it is necessary to develop appropriate measurement tools and monitoring techniques. Before presenting the solution for measuring the current in this thesis, main categories of the current measurement techniques are briefly reviewed first.

Current measurement techniques are basically divided into two groups: Eulerian and Lagrangian methods (Klemas 2012). In Eulerian methods, anchored (moored) instruments, deployed at a given depth, measure the water movement. On the other hand, Lagrangian methods involve drifters that are released in the ocean to be tracked by radio waves, acoustic methods or visually. Drifters are moved by the water flow and measure the speed and direction of the water. Since locating instruments is easier in Eulerian methods than finding drifters in Lagrangian methods,

Eulerian techniques are more popular (Klemas 2012). In this dissertation, anchored electroacoustic transducers are employed for current measurement. Thus, the developed method could be classified as a subset of Eulerian technique. In order to find the limitations of the existing measurement techniques, an overview of the most common current measurement methods is presented in the following section.

1.2 Ocean Current Measurement Methods

As it was mentioned previously, the most popular methods for measuring the ocean current (Klemas 2012; NOAA n.d.C.) are mainly divided into three groups: ADCPs, shore-based current meters and satellite remote sensing floats.

ADCPs use ultrasonic pulses to measure the speed of the current. Using ultrasonic techniques for flow measurement has mostly been developed and implemented for pipes (Tan, Cao et al. 2012; Rajalakshmy 2013) and water channels (Crabtree 2009). However, ADCPs are able to measure the velocity of a column of water in the open water (Deines 1999; Zedel and Hay 1999; Dinehart and Sacramento 2003). The principle employed in ADCPs is the Doppler shift principle. As ADCPs are still the most popular instruments for oceanographers to gather oceanic data, (NASA n.d.A.) and also RADAR measurements are based on Doppler effect fundamentals of the Doppler measurement is briefly reviewed. Equations (1.2) and Figure 1.1 describe the Doppler shift where f_0 is the emitted frequency, f is the observed frequency, v_s is source velocity and v_r is the received velocity relative to source. In Figure 1.1, the arrow pointing to the right shows the direction of the current. Transmitted and received pulses are marked with the f_0 and f

4

respectively. Signals I and II are the backscattered signals with f_I and f_{II} respectively. They have undergone a Doppler shift with a frequency of: $f_I < f_0$ and $f_{II} > f_0$.

$$\Delta f = \frac{\Delta v}{c} f_0 \qquad\qquad (1.2)$$

$$\Delta f = f - f_0$$

$$\Delta v = v_r - v_s$$
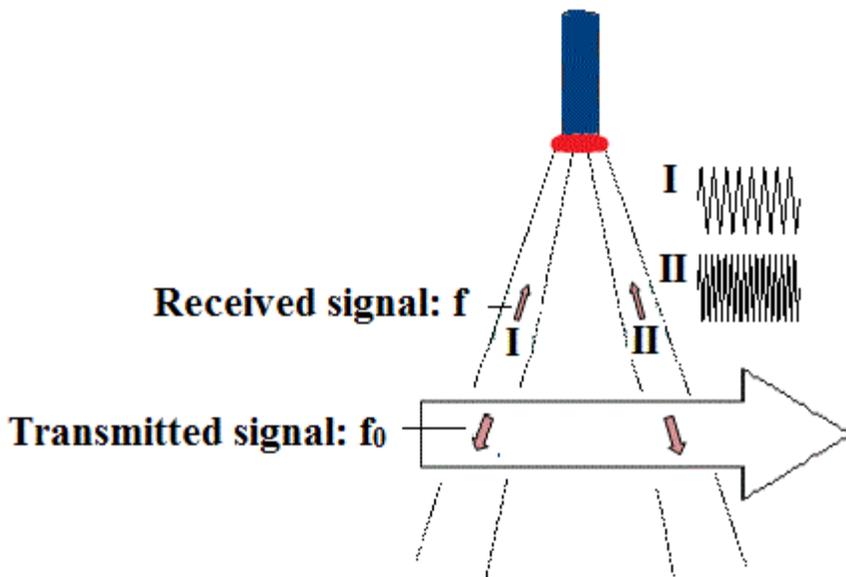
Figure 1.1 – Acoustic Doppler Current Profiler (ADCP).

Although ADCPs are very common for measuring the ocean currents, they have their own limitations. The most sever limitation of the ADCPs is being only a point measurement device. ADCPs provide a localized ocean current vector whose directional accuracy is very much derived from the accuracy of the associated compass reading. Point measurements are relatively easy to make using the ADCPs and these instruments can reveal current patterns at the measurement locations over time, yet they cannot be considered as a real-time method for measuring area-averaged current data.

The other group of measurement methods which is widely used (Klemas 2012) for ocean current measurement is Shore-based Current Meters, among which RADAR is very popular, with a similar principle to that of the ADCPs. In the RADAR approach transmitted electromagnetic waves, which can be reflected from the slightly rough sea surface, are processed in order to provide the speed of the current (Lurton 2002). Disadvantage of the electromagnetic remote method(s) is that they can only monitor the surface current and cannot observe deeper currents of the upper columns in the ocean (Klemas 2012).

Another group of current measurement techniques is satellite remote sensing current measurements. In this type of measurements buoys and (sub)surface drifters and floats transmit the measured data to the passing satellite (Joseph 2013; NOAA n.d. A). According to NOAA (NOAA n.d. A) the maximum depth at which real-time measurements are done is 15 meters beneath the surface which is not deep enough for some special purposes such as for the currents steering icebergs (70-100m). Other floats called Argo are designed to measure deeper currents but the current data is not real-time because they travel deep under the water for several days before the data stored in them can be downloaded (Fossette, Putman et al. 2012). Another problem with the floats and drifters could be locating these devices and collecting them from the see which seems to be very difficult and problematic.

According to the above mentioned limitations of the existing measurement techniques, real-time characterization of the complex movements of near-surface ocean water masses over broad areas still remains an issue for scientists and ocean industry alike. As a result, in this thesis a novel method is proposed for real-time broad area ocean current monitoring by employing acoustic transducers.

1.3 Research Objectives

In order to measure the real-time subsurface current a new method along with a large-scale network of acoustic sensors has been designed and proposed in this thesis. The new method is a modified version of the transit time method which is explained in details in Chapter 4.

Also, new architecture designs of Underwater Acoustic Sensor Networks (UASNs) are proposed. In the design of the UASN, the first and most important factor is the provision of energy in underwater environment. In fact in underwater environment, transmitters' power consumption is very high (Erol-Kantarci, Mouftah et al. 2011) and access to the node for battery replacement is difficult. Therefore, in this thesis, efforts have been made to optimize the energy consumption of the UASNs.

Authors in (Jurdak, Lopes et al. 2005) offer an energy optimization model for underwater networks. They consider three factors affecting their optimization design: first nodes' load needs to be balanced; second for each sensor, the number of descendant nodes is important; third each node's role (being a listener, forwarder, etc.) is subject to change during the process of transmitting the data. These three aspects are integrated in a policy in (Jurdak, Lopes et al. 2005) in order to yield a better energy-efficient data transmission in underwater environment. The main target in this paper is data transmission which is different than a network designed for underwater environmental monitoring.

Another work on underwater power optimization is presented in (Casari and Zorzi 2011) that focuses on the routing in a multihop network in which an optimal transmission frequency for various node distances is proposed. At the optimal transmission frequency, the acoustic signals undergo the least attenuation and are less affected by the noise. Also, according to the distances

between the nodes, they propose a protocol scheduling a delay for transmission so that the signals at the receiver never overlap. The other protocol that they have offered in their work is the one that adjusts the sleep-awake time of the nodes in order to save the energy within the network. Link distances are then balanced based on the nodes' energy consumption. Simulation results have been presented in (Guerra, Casari et al. 2009) using Word Ocean Simulation System. Authors in (Zorzi, Casari et al. 2008) are another example working on routing schemes and have investigated the effect the routing on the performance of an underwater communication protocol. Again, the focus of the two above mentioned papers is on data transmission.

 The other paper that has worked on the optimization of the underwater power consumption of a network deployed in near-surface depth is (Jurdak, Lopes et al. 2004) in which authors present designs of network topologies. In this paper four factors are considered that will affect the energy usage: inter-node distances, transmission frequency, number of nodes and the frequency of uploading data. Their paper offers a technique for estimating the life of batteries by examining the effect of distances between the nodes, frequencies and numbers of nodes. The authors report that their Constant Inter-node Distance method (setting a fixed distance between the nodes) is a more feasible configuration of the network as it is less dependent on the nodes' locations. On the other hand, their Variable Inter-node Distance (with increasing distances after some point) leads into a less energy consumption and is more suitable for data delivery applications.

The above methods are all concentrated on data transmission applications of the underwater networks which impose different requirements for the energy management than the management needed for the underwater monitoring network. According to Appendix 4, which is a comparison done between the networks designed in this dissertation for monitoring purposes and a recent work done on optimization of the energy consumption of an UASN for data transaction (Su,

Venkatesan et al. 2015), it is shown that monitoring networks use less energy because of the fact the rate of transactions are much lower in them Therefore, this open area in the research has become the focus of this thesis. For this reason the following reviews have been investigated.

Authors in (Jurdak, Lopes et al. 2004; Pompili, Melodia et al. 2009; Jha, Wettergren et al. 2015) have conducted reviews on UASNs' topologies, architectures and deployment. Erol-Kantarci et al. (Erol-Kantarci, Mouftah et al. 2011) classify the network architectures based on two criteria: mobility and coverage. As they mention, for monitoring purposes stationary networks are preferred because they are mainly two dimensional. In stationary networks, localization is done with Global Positioning System (GPS). Since the focus of this thesis is on monitoring applications as well, two-dimensional stationary networks has been researched and developed. Three-dimensional networks, on the other hand, have some other applications such as target detection and tracking (Pompili, Melodia et al. 2009) which is out of the scope of this study.

On the topology designs, power consumption and practical deployment concerns, an overview has been given by Wang et al. (Wang, Liu et al. 2012; XB24-Z7WIT-004 2016). They conclude that topology designs are based on important objectives such as energy consumption and investigate deployment challenges in two-dimensional UASNs which mainly include minimization of the number of hops in order to minimize the power consumption. They also referenced some previous efforts on maximization of the coverage area. However, most of these debates are on three-dimensional networks with data transmission purposes.

The multipath effect is another concern in UASNs that has been addressed in this thesis as well and is briefly explained in this section. Therefore, the main objectives of this thesis can be listed as follows:

1) To design a real-time energy efficient method for measuring the subsurface ocean current. This will enable the provision of data to be used for modeling and prediction of the ocean current patterns. Also the proposed novel architecture designs of the UASNs are based on previous works in this area such as (Jurdak, Lopes et al. 2004; Jha, Wettergren et al. 2015) with the difference that almost all of the previous efforts on underwater network developments have been on underwater data transmission and not for ocean environmental monitoring. In this thesis, two main topologies have been designed: hexagonal and square topology. For each topology, two configurations have been proposed: with-centre-node and without-centre-node configuration. These architecture designs are aiming at large-scale area-averaged ocean current measurements while keeping the energy demand of the whole network at its minimum level. In this thesis, in order to save the energy, effort has been done to reduce the node density in each of the topologies and at the same time increase the area covered by the network (Chapter 4). As previously mentioned, other similar works have been done on network architecture or protocol designs with the goal of minimizing the network's energy consumption (Tilak, Abu-Ghazaleh et al. 2002; Jurdak, Lopes et al. 2004; Jornet, Stojanovic et al. 2010; Casari and Zorzi 2011; Etter 2013; Jha, Wettergren et al. 2015) but the application in the previous works has all been data transmission and not environmental monitoring. The network architecture design for monitoring and data transmission demand different criteria because data transmission applications need high rate of data while monitoring applications need the whole network to be run less frequently (e.g. once or twice an hour or even less). This leads into differences between the networks with measurement or data-transmission applications. In the network with measurement application, the inter-node distance could be greater as it only suffices that the sensors' signal (both acoustic and wireless signal which are explained in Chapter 3) reaches each other and the system does not

necessarily need to cover the whole area because the current which is being measured is an area averaged (Attarsharghi 2016).

The principle of the measurements in the designed UASNs is based on a modified version of the transit time method. The novel technique leads into new energy efficient architecture designs of UASN and various features of the novel architecture designs are compared to each other in Chapter 4.

2) The second objective of this thesis is to investigate the feasibility of the network designs for the large-scale ocean current measurement using the results from a prototype developed and tested in an experimental set-up (Attarsharghi and Masek 2014) in (Chapter 2). A small-scale prototype tests the feasibility of node synchronizations, underwater and in-air communication with signal processing and current computations. This setup helps to understand the practical issues of a large-scale deployment in the ocean. Underwater sensor networks are different from terrestrial communication networks. Terrestrial networks are based on Radio Frequency (RF) signals. Based on skin depth effect (Vander Vorst, Rosen et al. 2006) ($\delta=503\sqrt{\rho.}(/\mu_r.f)$ where δ is skin depth in meter, ρ is resistivity in $\Omega.m$, μ_r is relative permeability of medium, f is frequency in Hz) the electromagnetic RF waves cannot propagate in underwater environment because the medium is conductor while they can propagate in their air. For the underwater medium acoustic signals (Xiao 2010) are the appropriate waves and acoustic instruments and sensors are much more expensive than the radio-based sensors. Therefore, due to the high costs of doing an open water experiment along with deploying transducers in the sea, conducting the experiment in the sea has been out of the budget of this project. Instead, the results achieved with the lab prototype along with simulation results (done with Bellhop which is an acoustic toolbox in Matlab) were the foundations for incorporating the practical complications into a large-scale deployment

11

(Attarsharghi 2016). Underwater simulation softwares are widely used in scientific oceanographic studies (Guerra, Casari et al. 2009; Petrioli, Petroccia et al. 2011; Porter 2011) in order to pre/evaluate the performance of the UASNs and thus it was considered in this dissertation (Chapter 3) in order to examine and expand the lab observations and incorporate them into large scale system designs as well as deployment strategies in the Northwest Atlantic ocean.

3) Since multipath effect is one of the most problematic issues in deploying underwater acoustic sensors (Etter 2013), the third objective of this thesis is to propose a solution in order to reduce the multipath effect in practice (Chapter 3). Multipath effect can interfere with signal processing at the receiver (Xiao 2010) and cause error in computations (Attarsharghi and Masek 2013A). Therefore, In order to minimize the multipath effect and sound reflection, an optimal positioning scheme for acoustic nodes is proposed in Chapter 3. The multipath effect has also been investigated in the lab-scale experiment (Attarsharghi and Masek 2014) and has been minimized by proper positioning in Chapter 2. A brief introduction to the multipath effect and how it interferes with the calculations is presented below.

Multipath effect is the phenomenon caused by the rays' reflections and refractions. Reflection happens once sound beams reflect from the surface or bottom while refraction happens when sound rays bend due to a change in the sound speed caused by changes in temperature, salinity or pressure in underwater channels. In the refraction, rays bend towards the channel or the layer of water with a lower speed of sound (Xiao 2010). Figure 1.2 is showing the reflection effect (Lurton 2002). Top figure is multipath trajectories in an isovelocity channel. Path *A* is the direct path, *B* is the wave reflecting on the surface, *C* is reflection on the bottom, *D* is reflection on the surface and bottom, *E* is the reflection on the bottom and surface. Bottom figure is also showing

the effect of multipath but in the time domain. It shows that the reflected signals mostly have lower amplitude than the direct signal.
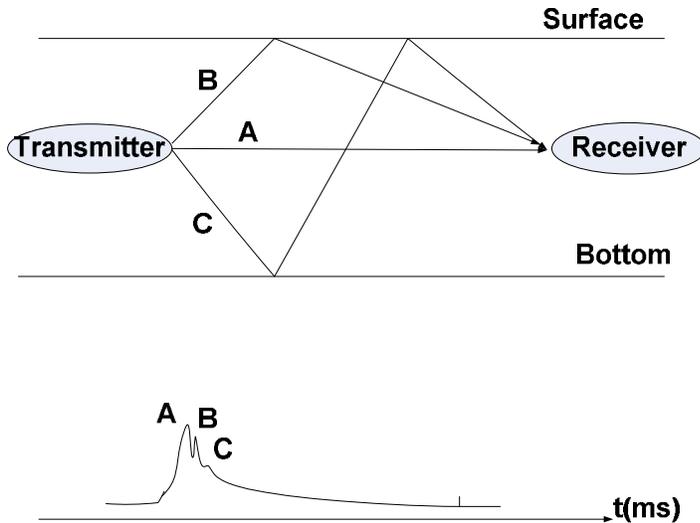
Figure 1.2. Reflections causing the multipath effect. Top: Multipath trajectories. Bottom: Multipath effect in time-domain (adapted from (Lurton 2002)).

Figure 1.3 is showing the spatial sound variability which causes the refraction. Temperature, salinity and pressure that vary with depth, are factors affecting the underwater sound speed and a sound ray always tends to bend towards the region where the propagation speed is lower.
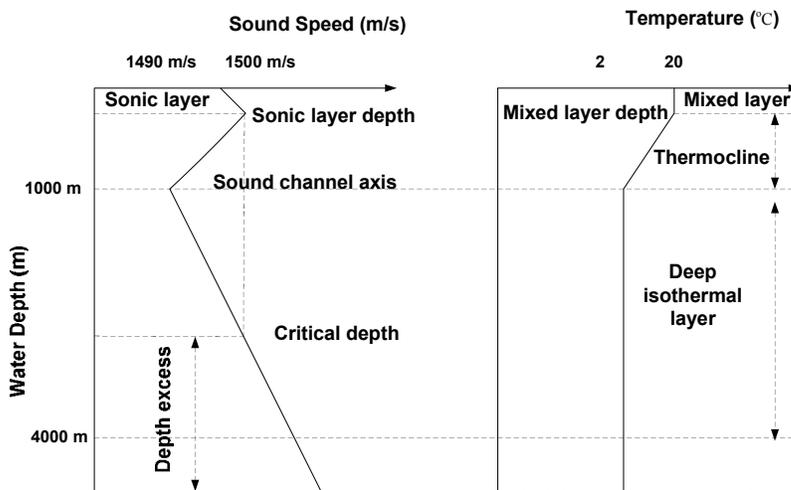
Figure 1.3. Left: Sound speed profile. Right: Temperature profile adapted from (Etter 2013; DOSTIS 2016).

13

Figure 1.3 shows the sound speed being constant near the surface where temperature and pressure are constant as well. But in thermocline region the temperature decreases with depth while the pressure increases; however the increase of the pressure cannot compensate the effect of temperature on the sound speed. Thus, sound speed decreases in the thermocline region. Beneath the thermocline region temperature remains constant but the pressure increases with depth. So the sound speed increases accordingly. These variations in the sound speed cause sound channels in the ocean and thus sound rays will go under refraction and multipath effect happens. In order to explain the error caused by the multipath effect in the measurement of the velocity of the current by the transit time method, an error model is offered in the following.

In transit time method (Lynnworth and Liu 2006) (Figure 1.4) velocity of the water is measured using Equations (1.3) and (1.4) where t_{up} is the time it takes the ultrasound beam to travel from emiter1 (E_1) to reciever2 (R_2) or simply the upstream travel time, t_{down} is the traveling time from E_2 to R_1 or downstream travel time, V is the velocity vector, α is the angle between acoustic path and the velocity vector direction, C is the speed of sound and L is path length between transducer 1 and transducer 2.

$$t_{up} = \frac{L}{cos\beta.(C-V)}$$ (1.3)

$$t_{down} = \frac{L}{cos\beta.(C+V)}$$ (1.4)

The difference between the upstream and downstream transit times are used to measure the average velocity of the liquid or gas. So, by having t_{up} and t_{down} and distance between receiving and transmitting transducers L, the Equation (1.5) gives the velocity:
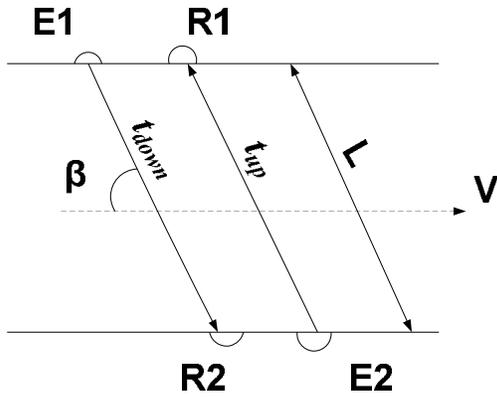
Figure 1.4. Transit time flowmetering.

$$v = \frac{L}{2Cos\beta} \ (t_{up} - t_{down})/(t_{up} \cdot t_{down}) \tag{1.5}$$

Now by having Equation (1.5) as the equation that is used to measure the velocity of water, the error caused by the multipath effect can be modeled (Attarsharghi and Masek 2013; Attarsharghi and Masek 2013A). In Figure 1.5, L is the length of the channel or direct path. The sound wave is supposed to travel from point A to point B and return from B to A. If multipath is formed, the ray may go under the multipath effect and travel through the path 1 (equivalence of the path whit three reflections in path 2) or path 3 (equivalence of the path with one reflection) instead of the direct path (L) and the velocity is measured with error. The measurement error is actually resulted by the extra distance that is travelled because of several reflections and is explained in the following.
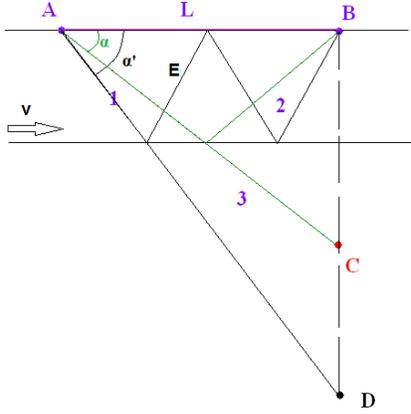
Figure 1.5. Multiple path schematic diagram

According to (1.5) and Figure 1.5, when multipath phenomenon happens for example in the path 2, the velocity of water (v) should be calculated by equation (1.6) with the angle α' and the path E which is the distance the sound ray travels with three reflections. Also in the case with just one reflection (path 3) the actual path, which is the path with one reflection, replaces the distance E in Equation (1.6), which can be expressed as if the wave has traveled between A and C with angle α.

$$v = \frac{t_{1up} - t_{1down}}{t_{1up} \cdot t_{1down}} \cdot \frac{E}{2cos\alpha'} \tag{1.6}$$

Since the number of reflections and consequently the actual path is unknown to the microprocessor at the receiver, in which calculations is performed, the assumed path length would be L with the angle α=0. Thus, the velocity (v') is mistakenly calculated with the distance considered to be L as in (1.7).

$$v' = \frac{t_{1up} - t_{1down}}{t_{1up} \cdot t_{1down}} \cdot \frac{L}{2} \tag{1.7}$$

However, a correct value for velocity should be calculated by considering the actual path, which is given by mapping L onto the line connecting A and C which is equal to $L/cos\alpha$. Substituting this into (1.7), gives (1.8) which is the actual velocity.

16

Since traveling time is same for both cases (*v'* and *v*), of error in velocity measurement is calculated with (1.9).

$$v'' = \frac{t_{1up} - t_{1down}}{t_{1up} \cdot t_{1down}} \cdot \frac{\frac{L}{cos\alpha}}{2cos\alpha} \tag{1.8}$$

$$\varepsilon_v = \frac{\Delta v}{v''} = \frac{|v' - v''|}{v''} = |cos^2\alpha - 1| = sin^2\alpha \tag{1.9}$$

The error in equation (1.9) is only dependant on the angle of the sound beam and is independent of the number of reflections; e.g. by considering the case that the wave travels with three reflections (via path 2 which has an equal length as path 1), the path length seen by the wave is similar to the path traveled between *A* and *D*. In this case *L* should be mapped on the line connecting *A* to *D* and the difference is only the angle in (1.9) which becomes α' in this case, as it is depicted in the Figure 1.5.

Therefore, in order to minimize the unwanted effects of the multipath phenomenon, positioning of the acoustic sensors has been studied in Chapter 3. Also Chapter 2 describes the positioning technique for open water environment and presents simulation results.

As an introduction to the Chapter 2 which addresses the experimental results, section below is devoted to explaining the instrumentation and hardware designs which has been used in the lab. See Appendix 6 for an example of relation between beamwidth of transducer and error.

1.4 Instrumentation and Hardware Design

In the laboratory experimental setup, a driver was designed for the transmitter, plus an amplifier and a filter for the receiver (Attarsharghi and Masek 2013; Attarsharghi and Masek 2013B) with the designed details explained in the following.

The transmitter setup includes a signal generator, power amplifier, impedance matching module and the transducer. Signal generator can produce a low-voltage signal which should be amplified by the driver in order to reach a proper level needed for stimulating the transmitter. The impedance matching module maximizes the transmission of the power to the transducer. In most cases, in order to improve the electrical efficiency, an inductance with a value dependant on the frequency is used in parallel with the transducer in order to make the input electrical impedance purely resistive. This dependency to the frequency is posing a limitation and this method of improving the efficiency suits narrow-band applications (Lurton 2002). Therefore, in order to remove this limitation, a transformer is used for impedance matching. Since the turns-ratio in transformers is constant and independent of the frequency, impedance matching is consistent as well. In the following sections, first the theory of the sound field is briefly reviewed in 1.4.1 and then the details of the design of the driver and amplifier in section 1.4.2 are addressed.

1.4.1 Sound Field

The first subject to be discussed is the wave interaction as this is important in proper placement of the ultrasonic transducers. Transducers' surface is like a source of many individual points from which the sound wave originates. As a result of the interaction between these waves, a sound field is formed. The waves superimpose while interacting and the sum of the amplitude of individual waves gives the amplitude of the particle displacement at each point. If two waves are in phase, they will combine to double the effect of each other on the point. On the other hand, if they are completely out of phase, they combine to cancel each other (Boyce 2014). Constructive and destructive interferences of the waves, originating from the transducer surface, cause significant fluctuations in sound intensity in the near field which is close to the transmitter

(Figure 1.6). Due to acoustic variations in this field, flaws cannot be evaluated accurately. While in the far field the ultrasonic beam is more uniform and well behaved. Wave contribution from different points on the transmitter is constructive and the field intensity tends to decrease similar to a spherical trend in distance and falls monotonously. Therefore, a receiver transducer should be placed in the far field distance from the transmitter (Figure 1.6).
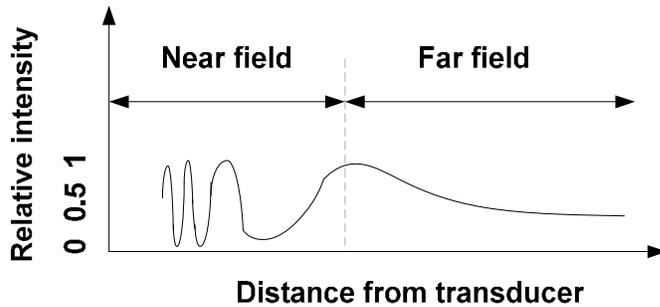
Figure 1.6. Sound field: Intensity vs. distance (adapted from (Baldev 1999)).

In order to place the receiver transducer in the far zone of the projector (transmitter), Equation (1.10) is used to calculate the proper distance where d is the distance between transducers, a is the largest radius of the transmitter and λ is the shortest wavelength used (Baldev 1999).

$$d \geq a^2/\lambda \tag{1.10}$$

Cylindrical transducers which are used in the experiments of this research are AquaTrans hydrophones (Figure 1.7) with a brass plate located at one end of the transducer preventing the waves produced by the piezoelectric ceramic to propagate backward.

Figure 1.7. AquaTrans hydrophone

For *AquaTrans*, *a* is 0.07*m*, *c* is 1480 m/s and for the range of frequency used in the tests f≤25*KHz* the wavelength is λ≥ 0.0592*m*. So that the distance is *d*≥0.0827*m*. Based on this minimum distance that is calculated, the receiver transducers was placed in the far field of the transmitter in all experiments

1.4.2 Design of the Driver and the Amplifier

A common emitter configuration circuit in Figure 1.8 along with a transformer is designed to be the driver that amplifies the signal of the source, which is a signal generator in this case, for the projector. The common emitter gain is given by the ratio of $-Rc/R_E$ (Sedra and Smith 2013) in which *Rc* is the equivalent impedance/resistance of the transducer multiplied by the square of the inverse turns-ratio of the transformer ($Z_{transducer}.(\frac{N_1}{N_2})^2$)). Resistor in emitter is shown by R_E, electrical impedance of the transducer is represented by $Z_{transducer}$, N_1 is the transformer's primary number of turns and N_2 is the secondary. The transformer is playing an important role in impedance matching between the transducer and the generator. D_1 is a freewheeling diode eliminating the flyback across the primary inductor of the transformer and D_2 and D_3 are protecting the transducer from high voltages spikes of the secondary inductor of the transformer.

The driver in the experiments is designed so that the impedances of the circuit and loading transducer match in a relatively wide range of frequencies (by using transformer instead of a simple inductor) in order to maximize the power transmission into the load. Figure 1.9 is a parallel representation of the transducer. Considering this representation, two types of electrical power exist for a piezoelectric transducer: the active power (P_{act}) corresponding to the resistance-dissipated energy which is considered in the transducer radiation, and the reactive power (P_{reac}) corresponding to the capacitance-stored energy (which is not considered as the useful power)

(Schavemaker and Van Der Sluis 2008). And the power supplied to the circuit is called $P_{apparent}$.

Equations (1.11) (Schavemaker and Van Der Sluis 2008) are formulating the active and reactive

powers:

$$P_{act} = \frac{V^2}{R} \qquad (1.11)$$

$$P_{reac} = \omega C V^2$$

$$P_{apparent}^{\ 2} = P_{act}^{\ 2} + P_{reac}^{\ 2}$$

$$Q_e = \frac{P_{act}}{P_{apparent}}$$

Electrical quality factor is called Qe. To improve the electrical efficiency, reactive power needs

to be decreased by modifying the transducer's impedance. This, as previously mentioned, could

be achieved by adding a parallel inductance with a value of $1/(\omega^2 C)$, then the input electrical

impedance is purely resistive. But this efficiency is completely dependent on the frequency. In

order to have a larger band width, another solution is considered which is an adaptive

transformer used for matching the transducer's impedance with the generator's (Lurton 2002) in

Figure 1.8. Since the turns-ratio in transformers is constant and is independent of frequency,

impedance matching is independent of the frequency and consistent as well.

Figures 1.10 left the pre-test set up environment which is a plexi glass tank in which transceivers

are appropriately placed to sense each other and Figure 1.10 right demonstrates the voltage at the

secondary of the transformer. This voltage is the output of the driving circuit along with the

transformer, and justifies that the amplifier and the matching unit is properly designed to transfer

an amplified voltage of the source to the load.
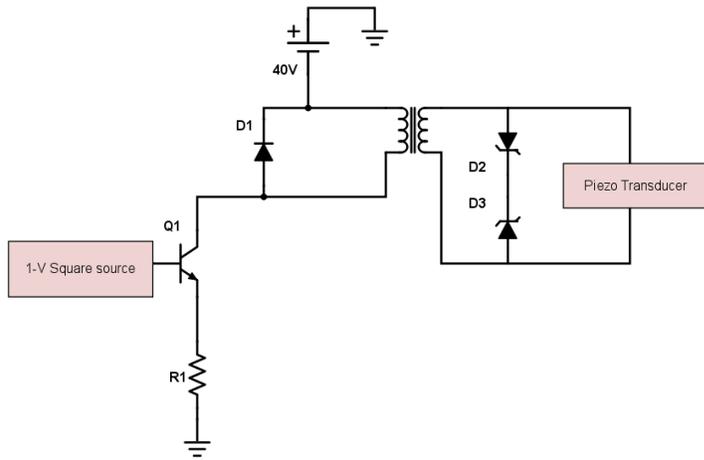
Figure 1.8.Power amplifier design with impedance matching unit (transformer).
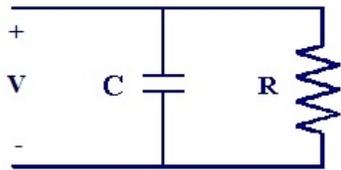
Figure 1.9.Electrical equivalent circuit of electroacoustic transducer Parallel representation of a transducer.
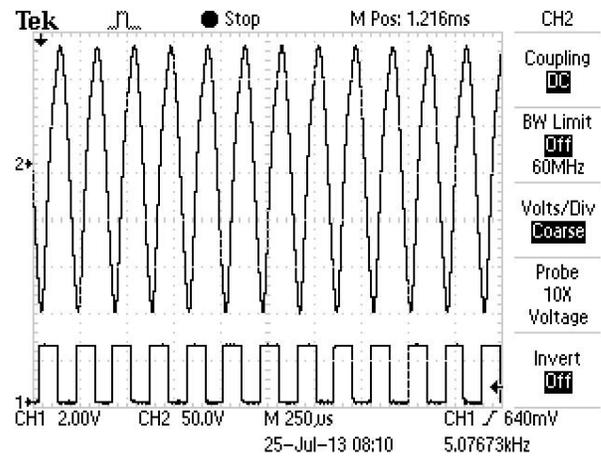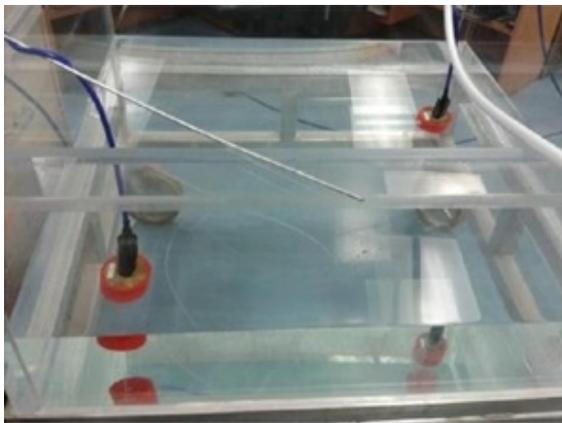
Figure 1.10. Left: Plexiglass tank setup with cylindrical AquaTrans receiver placed in the far field (1m) of the transmitter. Right: input and output voltage of the driver at the frequency of 5.08KHz; Ch1: Vinpulse= 0-2.5V, Ch2: VSecondary = 270 VPK-PK loaded with a transducer.

22

At the receiver (1m apart from transmitter), also, weak signals need to be amplified. In the experimental setup LM1875 (Figure 1.11 left) is used which is specifically designed for acoustic applications having a very low distortion, high gain (A_{VO} typically 90 dB), wide power bandwidth: 70 kHz, wide supply range 16V-60V and ripple rejection). In the case of very weak received signals, two units of these amplifiers are cascaded. The response at the receiver is shown in Figure 1.11 right.
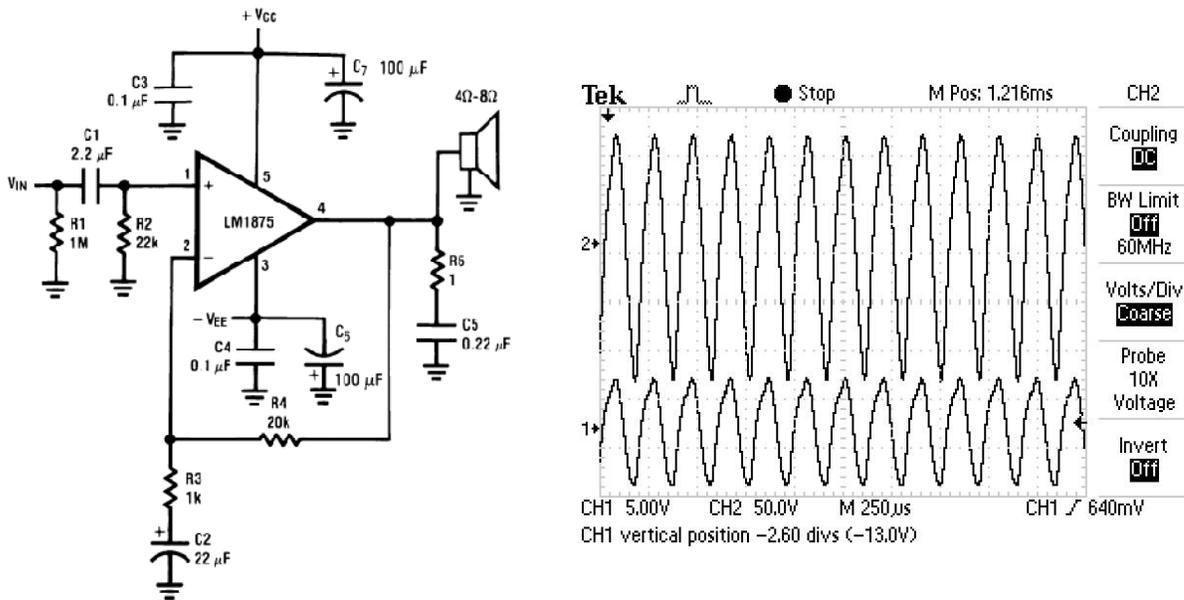
Figure 1.11. Left: Amplifier at the receiver. Right: Receiver signal in the Plexiglass Tank Setup With an input pulse of 0-2.5V and 5KHz applied to the transmitter's driver: Ch2 is the signal at the secondary of transformer. Ch1 received amplified signal with the LM1875.

1.5 Thesis Format

This thesis follows a manuscript style, with three papers, as well as the introduction and concluding chapter. All of the references appear at the end of thesis rather than after each chapter. The reader will notice that there is some repetition in the papers, specifically description

of the laboratory experimental setup, design and results, description of transit time method and some figures explaining the fundamentals of the current measurement method in Chapters 2-4. A summary of each paper is listed below:

Paper 1
Ocean Current Monitoring via Cross-Correlation Technique and Node Synchronization
Samareh Attarsharghi, Vlastimil Masek

This paper is co-authored and is published in the Proceeding of *OCEANS-St. John's* (2014, 1-7). S. Attarsharghi designed and implemented the lab-scale experimental prototype, conducted the experiment and calculated the results.

The experimental results in this paper show feasibility of measuring the current between synchronized acoustic transceivers using cross correlation technique. This paper is significant as it provides the details of the design of the current measurement setup and the computations as well as addressing the positioning technique for the transducers in order to minimize the multipath effect. In addition, by defining a suitable time-window at the receiver the unwanted effects of sound reflections, which can interfere with the calculations, has been eliminated. Furthermore, it is shown in this paper how to overcome the practical limitations of the hardware in order to achieve an accurate result.

Paper 2

Design Criteria and Practical Insights into an Underwater Current Measurement System along with the Simulation Results of a Real-Case Scenario in Northwest Atlantic

Samareh Attarsharghi

This paper is sole-authored and is published in *The Journal of Ocean Technology* (2016, 11(1): 94-116). S. Attarsharghi has done the analysis on the practical complications and has proposed the solutions. Also she has performed simulations and analyzed the simulated and experimental results and has incorporated them into a large-scale UASN system design.

This paper addresses the first systematic investigation of the practical aspects in deploying an UASN for ocean environmental monitoring. Understanding the limitations of the techniques and tools in practice has a considerable impact on the feasibility of the designs. In this paper underwater acoustics software has been used as a tool for assimilating the lab-scale results into a large-scale open water current measurement system. A new positioning technique, based on the variation of temperature and salinity, results in the minimization of the multipath phenomenon at sea.

Paper 3

Energy Efficient Architecture Designs Of An Underwater Acoustic Sensor Network For Ocean Current Monitoring

Samareh Attarsharghi, Vlastimil Masek

This co-authored manuscript is in press in *The Journal of Ocean Technology* (2016, 11(3)). It proposes a new energy efficient method based on transit time technique for ocean current monitoring. In this paper S. Attarsharghi outlines the first attempt of designing energy efficient underwater networks for measuring the speed of the near-surface current. The new proposed

current measurement technique is employed in the UASNs with novel architecture designs to show how it helps in saving the energy. All UASN architectures' performance are then compared to each other in terms of the energy demand of the whole network and also the coverage area and the results are graphically presented.

Chapter 2: Ocean Current Monitoring via Cross-Correlation Technique and Node Synchronisation

Samareh Attarsharghi, Vlastimil Masek

A version of this chapter was published in:

2.1 Abstract

In the North Atlantic Ocean, accurate prediction of the trajectory of icebergs would enable optimization of shipping routes and offshore production processes. In this paper, we investigate the practical aspects of the proposed current measurement technique which is based on transit time method and cross correlation signal processing in a flow tank. The experiments are carried out as a prototype of a larger network of acoustic transducers to investigate the feasibility and/or limitations of this system for measuring the average-shallow depth current in the ocean.

2.2 Introduction

Ocean current measurement is a subject of interest to oceanography, weather forecasting and many other fields. Therefore, efforts have been made in this area but the present methods are either using the point measurement data, like data collected from the Acoustic Doppler Current Profilers (Dinehart and Sacramento 2003), which is not always providing the average magnitude of the ocean current across a wide area; or remote sensing techniques, such as radar (Paduan and Graber 1997), which measures only the surface current and not the current at certain depth. A limited study has been conducted simulating the average current by combining the radar and point measurement techniques to reconstruct the shallow current data, though the final reported values are simulated ones and not the in-situ or actual average current (NOAA n.d.D.).

In this paper, we propose a technique which is the basis of a system of distributed acoustic transducers and is based on the measurement of transit time method and the cross correlation signal processing. Practical aspects of implementing the prototype are investigated to prove the

feasibility of conducting the test in a large scale in the ocean as well as the existing limitations which is caused by the electronic devices.

So in order to elaborate the details, design of the components is discussed in the section II of this paper and the practical aspects of implementing the prototype are explained. Then, in section III, results of the deployment of the system are presented and following that, in section IV, a conclusion opens a discussion about the next steps.

2.3 System Components

The system is composed of an ultrasonic transmitter and receiver, a driver which amplifies the power of the transmitted acoustic signal and an amplifier that amplifies the received signal. GPS precise clock is used to synchronize the two units of transceiver with each other and the experiments are carried out in a flow tank.

2.3.1 Transducers

A pair of omnidirectional (toroidal) beam pattern, cylindrical shape transducers (Figure 2.1.) is used in the experiments with a brass plate located at one end of the transducer which prevents the waves, produced by the ceramic, to propagate backward.

Figure 2.12. Omni-directional electroacoustic transducer

In ultrasonic transducers the near field and far field distance depends on the design of the transducer. Therefore a proper placement of the ultrasonic transducers is also important (Lurton 2002).

In near field, waves have constructive and destructive interferences that cause significant fluctuations in sound intensity. Therefore, in a near field distance of an ultrasonic transducer, flaws cannot be evaluated accurately and in contrast, ultrasonic beams are more uniform in the far field. So, a proper distance for the hydrophone (receiver transducer) is in the far field distance from the projector (transmitter) which is shown in Figure 2.2.

The far field distance can be given by Equation (2.1) (Lurton 2002) where d is the distance between transducers, a is the largest radius of the projector and λ is the shortest wavelength used (Baldev 1999).
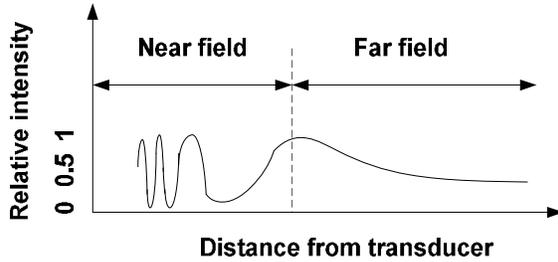
Figure 2.2. Near field and far field

$$d \geq a^2 / \lambda \tag{2.1}$$

For the transducers used in these experiments, dimensions are: $a = 0.07m$, $c = 1480$ m/s, $f_{largest} = 3KHz$ and so $\lambda = 0.592m$. This gives: $d \geq 0.0098m$. According to these calculations, both transmitter and receiver were placed in the far field of each other, in the experiments.

2.3.2 Design of the Driver at the Transmitter

Transducers can be represented with a parallel circuit as shown in Figure 2.3. So, two types of electrical power exist: active power (P_{act}) which corresponds to the resistance and reactive power (P_{reac}) *that* corresponds to the capacitance (Lurton 2002). Reactive power can be reduced by using a transformer with a suitable turns-ratio as an impedance matching unit (making it totally resistive) and in order to achieve a better electrical efficiency. This can be done by matching the transducer's impedance with the driver's (Figure 2.4). Meanwhile, because of its low-to-high turns-ratio, it is playing the role of an amplifier as well.
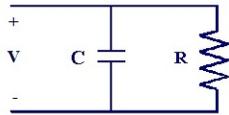
Figure 2.3. Parallel representation of electroacoustic transducer
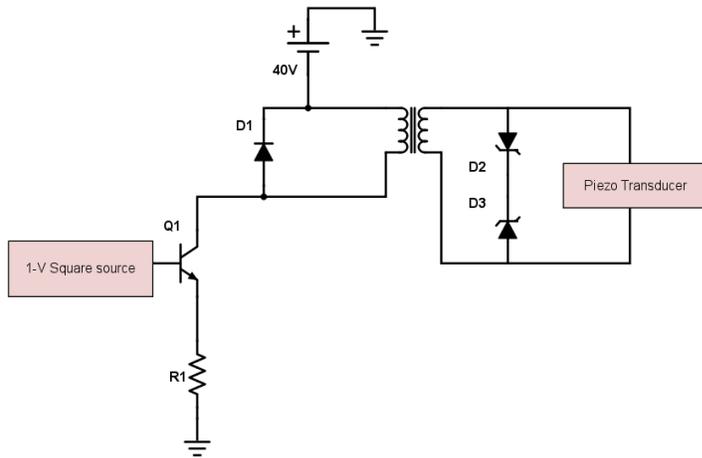
Figure 2.4. Power amplifier design with impedance matching unit (transformer)

2.3.3 Design of the Amplifier at the Receiver

LM1875 (Texas-Instruments 2002) is specific amplifier for acoustic purposes which is used with the circuit design shown in Figure 2.5. and is intended to amplify the weak signals at the

31

receiver. These amplifiers could be cascaded to amplify very weak signals at the receiver and they are advantageous to an analog amplifier as they have very low distortion, high gain of 90 dB (AVO), wide power bandwidth of 70 kHz, wide supply range of 16V-60V and the ripple rejection.
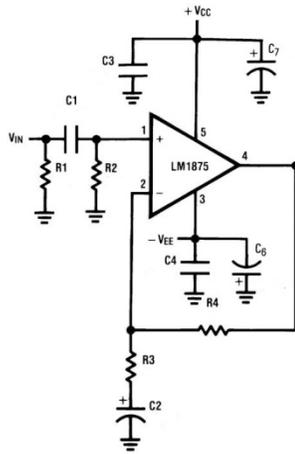
Figure 2.5. Amplifier design at the receiver

The hydrophone, located in the far field (8 meter) of the projector in a flow tank, produces voltage in response to the acoustic sounds, which is amplified by LM1875. In order to minimize reflection of the signal from the walls, surface and bottom of the tank, transducers are positioned properly according to the criteria discussed in the following section.

It should be mentioned that the power of the designed driver/amplifier were practically examined in previous works for larger distances (Attarsharghi and Masek 2013; Attarsharghi and Masek 2013B). So, based on the range of the equipments employed in this system, this prototype would be suitable for larger distances in the open water.

2.3.4 Flow Tank

The velocity of the water is adjusted to 0.4 m/s (using styrofoam and stopwatch to measure it in the flow tank) in a flow tank (Figure 2.6) of height 0.57 m, width 0.45 m and length 10 m.

Figure 2.6. Flow tank in fluid laboratory (Memorial University)

As Figure 2.7 shows, h is height, w is width and L is length of the tank and the pulse duration of the pings (acoustic signals) should be calculated according to the transducers' distances from the reflectors (walls, bottom and surface, each other) in order to prevent or reduce reflection-produced errors in calculations. The following set of Equations (2.2) (Lurton 2002) explains the relations between these parameters.
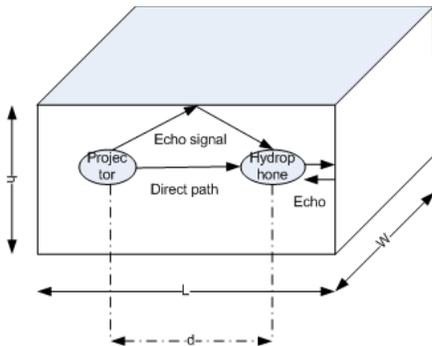
Figure 2.7. Dependence of distance between transceivers to the reflector surfaces

$$\tau \leq \frac{2d}{c} \qquad \text{Reflection between transducers} \qquad (2.2)$$

$$\tau \leq \frac{L-d}{c} \qquad \text{Reflection from wall}$$

$$\tau \leq \frac{\sqrt{h^2+d^2}-d}{c} \qquad \text{Reflection from upper or bottom surface}$$

In the above equations, τ is the period of the signal, h is height, c is velocity of sound in water, L is the length of the tank and d represents the distance between the two transducers.

Because of limitations of the sampling rate imposed by the microcontroller, the design process starts with choosing a suitable value for τ. Meaning that the period was first set to $\tau=3ms$ and then noticing the velocity of the sound in water ($C=1480m/s$), the above equations give $d \geq 2.22m$, $h \geq 4.96m$, $L \geq 6.6m$. As the height of the tank was shallow, the condition for h could not be totally fulfilled. So this might be a partial reason for having some error in the measurement process added to the method used to measure time and other causes of uncertainty.

2.3.5 Filter

The purpose of adding a band pass filter (Figure 2.8, 2.9) is to eliminate low (from the water pump in the current series of experiments) and high frequency noises (for further applications in other environments) and have a clean signal for processing.
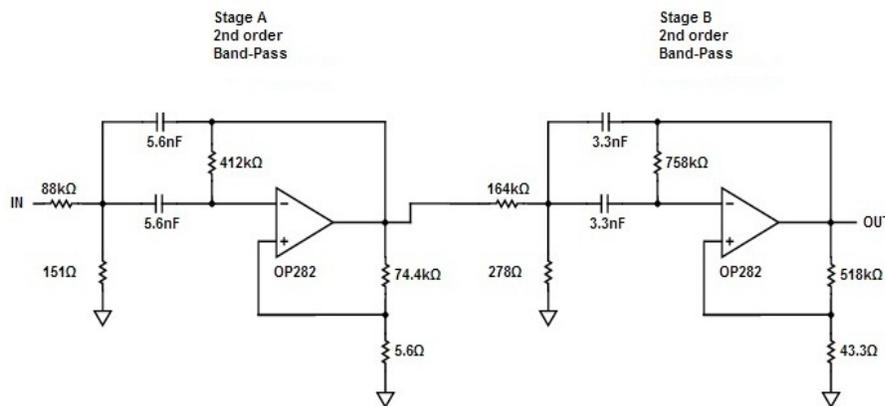
Figure 2.8. Two-stage 4th order Chebyshev band pass filter; circuit design
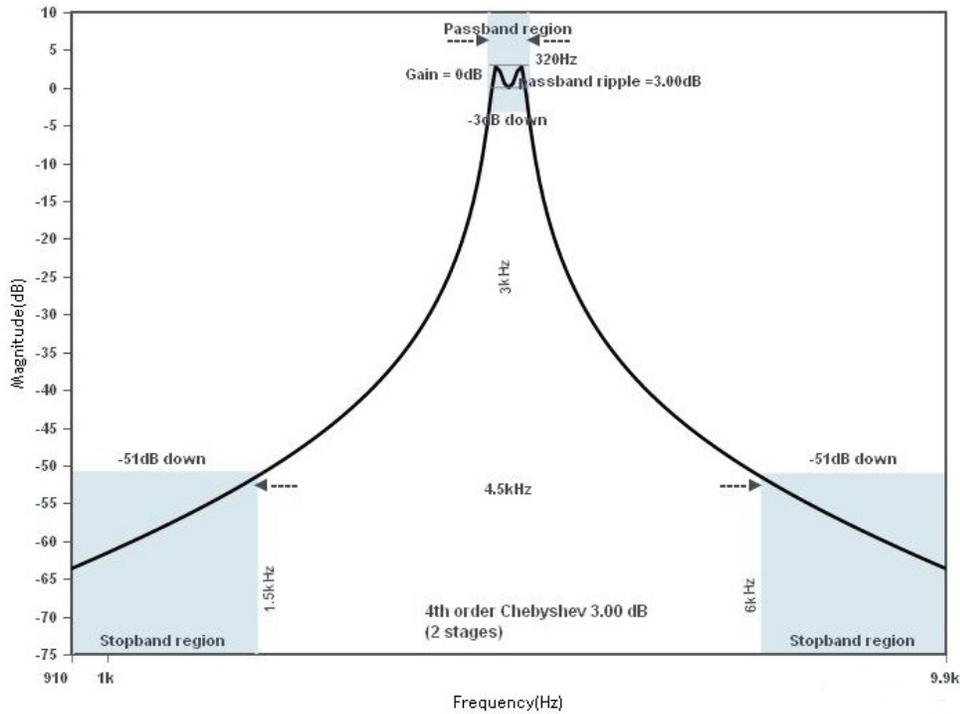
Figure 2.9. Two-stage 4th order Chebyshev band pass filter specification

2.3.6 Synchronization

In order to measure the precise travel time in the transit time method, all the nodes should be synchronized with each other. The following block diagram (Figure 2.10) and also the state machine (Figure 2.11) explain the procedure of measuring delay in our prototype system. Arduino wireless modules (ZigBee module) (Figure 2.12)(Arduino-Uno 2013) perform the wireless communications and GPS modules (Figure 2.13) with a PPS output pulse (Figure 2.14) is used as the synchronization unit.
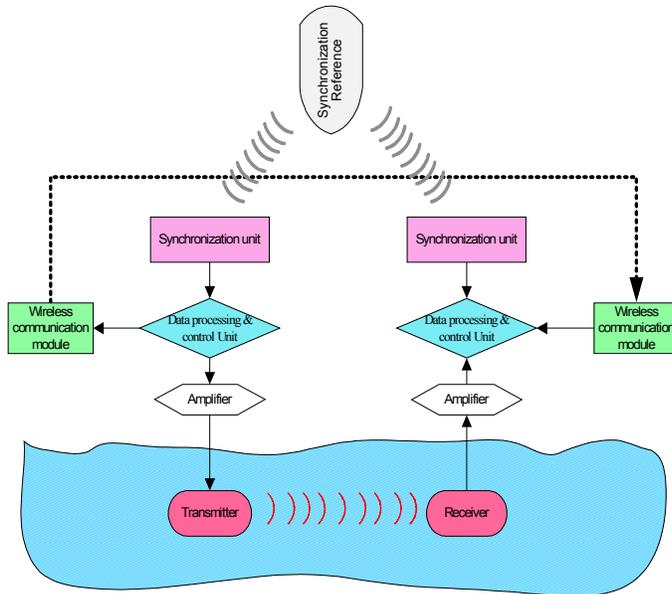
Figure 2.130. Synchronization Block Diagram.

State machine diagram at the receiver

Idle State: The slave node (Receiver Node) stays idle until the issuance of standby command from master node (Transmitter Node).

Standby State: After reception of a predefined command from master node, the slave node enters standby state. In this state the slave node seeks to detect the next rising edge of synchronization signal.

Listening State: Upon detection of the first rising edge of the synchronization signal, the slave node goes to the listening state in which it listens to hear the sonar pulse. As soon as the node begins to listen to its environment, a timer is turned on to measure time delay.

Data Processing State: By detection of the sonar signal, the timer stops counting and some initial processing takes place; and then the slave goes back to the idle state.

Figure 2.11. State machine diagram at the receiver

Figure 2.12. Wireless module

Figure 2.13. GPS module as the synchronization unit
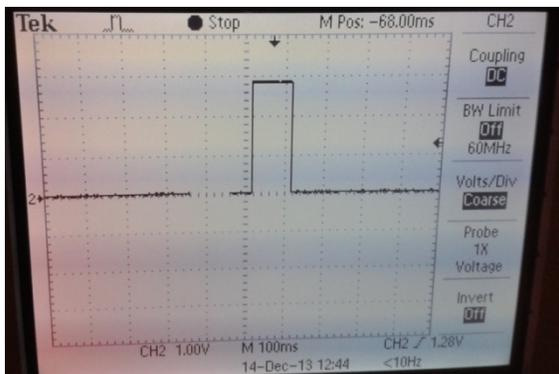
Figure 2.14. PPS output of the GPS

An automated procedure which is implemented in the system of Figure 2.11 is explained here. The wireless module (Figure 2.12) on transmitter side informs the receiver to be ready to receive the acoustic pings. After sending this message, transmitter sends the acoustic pulse at the rising edge of PPS output of the GPS (Figure 2.13 and 2.14). On the other side, the standby-receiver scans the input for the rising edge of synchronization unit's pulse or signal and as soon as the arrival of the PPS, it records the received acoustic signal for a limited time-window. This time limitation is imposed by the hardware as any type of processor has a certain amount of memory which is capable of holding just a limited amount of data. So, in the following experiments, the time-window that is sufficient to capture the whole transmitted acoustic pings at the receiver, is

37

estimated based on the expected time delays for the extreme cases of the velocity of the water as well as the capacity of Arduino's microcontroller memory (Arduino-Uno 2013).

After sampling the received pings and saving them in a vector, microprocessor cross-correlates (described by equation 2.3 and figure 2.15 where x* denotes the complex conjugate of x (Rabiner and Gold 1975). This vector with a reference signal (captured during a calibration phase or in lab test when the flow of the water is zero) which is saved in the memory. This allows the detection of the moment when the signal was thoroughly received. This moment is yield from the sample number at which the maximum amplitude in the cross-correlated signal happens or in other words i_0 in Equation (2.4). In this equation, x is the symbol of the signal which is saved in the memory and y is the one which is received by the hydrophone. Experimental results and Figures in the next section, explain this process.

$$(x * y)[n] \stackrel{\text{def}}{=} \sum_{i=-\infty}^{\infty} x^*[i] y[i + n] \tag{2.3}$$
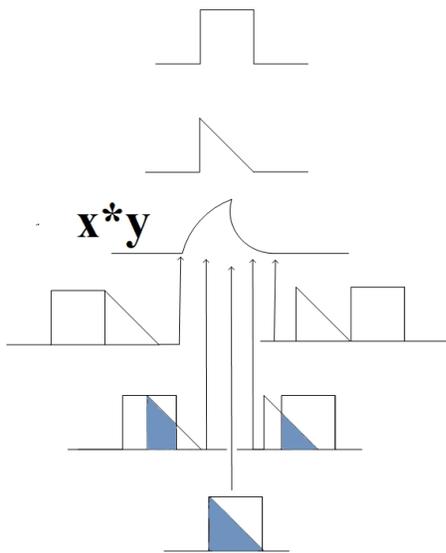
Figure 2.15. Cross correlation method

$$\hat{i}_0 = \max_{i_0} \left(\sum_{i=i_0}^{i_0+M-1} x[i]y[i+i_0] \right) \tag{2.4}$$

By having the sound pings' travel-time between the two transducers and also the distance between the nodes, the speed of the water is calculated with transit time method in Equation (2.5).

$$t_{up} = L / ((C+V).\cos\alpha) \tag{2.5}$$

$$t_{down} = L / ((C-V).\cos\alpha)$$

$$v = L / 2Cos\alpha.(t_{up} - t_{down})/(t_{up}.t_{down})$$

The above equations explain how the difference between upstream and downstream travelling time is used to yield the velocity of water independently from the velocity of the sound in the water. L is the distance between the two transducers, c is the sound speed and v is the velocity of water. Next section sheds more light on the practical points.

2.4 Experimental Results

Arduino Uno boards use ATmega328 microcontrollers which have the advantage of being user friendly and more economical compared to their counterparts, e.g. FPGAs or DSPs. So, this prototype can be easily expanded to several nodes in order to monitor the current in a large area of interest, i.e. the area in which icebergs are more frequently causing problems for the offshore and shipping industries.

Following results have been achieved from a laboratory-scale prototype which will be proved in the next steps of the project that is suitable for a larger ocean-scale current monitoring. Experimental conditions such as the tank's dimensions and etc. were described in the previous

section and the Figures below are the captured signals at the receiver. It should be mentioned that the operational sampling time of the microcontroller, which is the lowest practical sampling period, is measured to 8μs during the tests.

2.4.1 Memory

Figure 2.16 shows the setup. In Figure 2.17 the signal which is saved in the memory of the receiver node in a pretest experiment. This is the signal (x) that is being cross-correlated with the one which is received during the test. In all Figures, signal shown on the channel 2 is the signal received at the receiver before being filtered by the band pass filter (BPF) in Figure 2.8.

Figure 2.16. Automated current measurement system
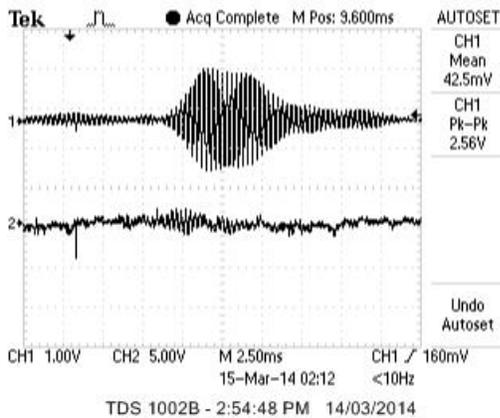
Figure 2.17. Ch1 is the Signal stored in memory of the receiver. Ch2. same signal before BPF

2.4.2 Downstream

2.4.2.1 Transmitted Signal

Figure 2.18 shows the signal before being sampled by the receiver located at the downstream.
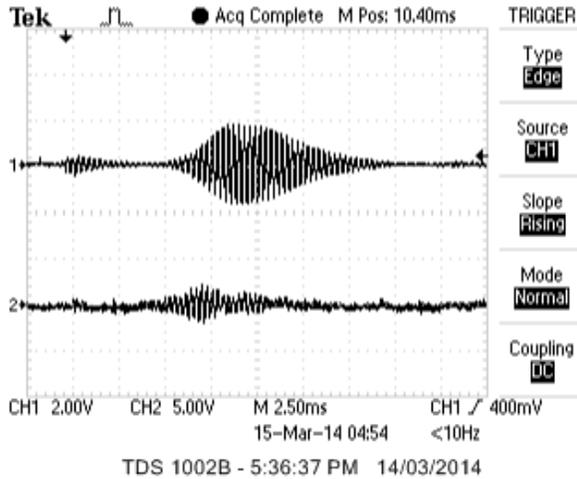
Figure 2.18. Ch.1 downstream signal after BPF. Ch2. same signal before BPF

2.4.2.2 Cross-correlation

Equation (2.4) is used to implement the algorithm of cross-correlation between the two sampled signals of Figure 2.17 and 2.18 in the microcontroller firmware and then finding the desired maximum index. The result is shown in the Figure 2.19.
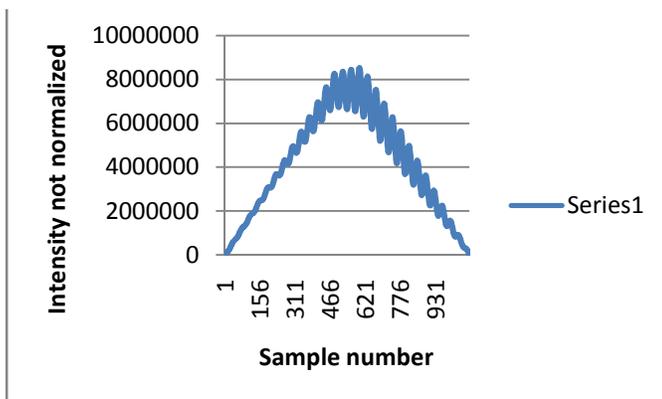
Figure 2.19. Cross-correlated signal: downstream signal with the signal pre-stored in the memory

As it can be seen in the Figure above, the cross-correlated graph has a peak with its respective index. The index shows the sample's number (598), which is an average index achieved from a number of tests, and knowing the sampling time of the microcontroller (8μs), the peak time is given: 4.784ms. The time delay or travel time between the two nodes (transducers) would be the peak time (4.784ms) plus the delay (Toffset=8.48ms) which is necessary in order to stabilize the transmission of the pings from the transmitter to the receiver.

2.4.3 Upstream

Similar to the downstream process, now the receiver which is located in the upstream, receives the signal (Figure 2.20) and samples it to be stored in the microcontroller.
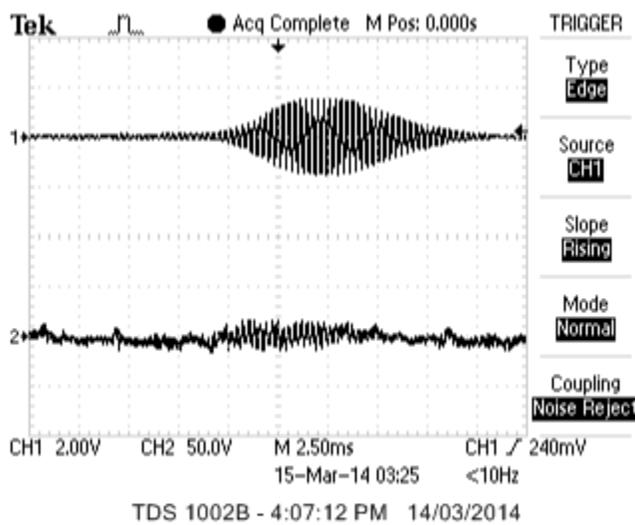
Figure 2.20. Ch.1 upstream signal after BPF. Ch2. Same signal before BPF

2.4.3.1 Cross-Correlation
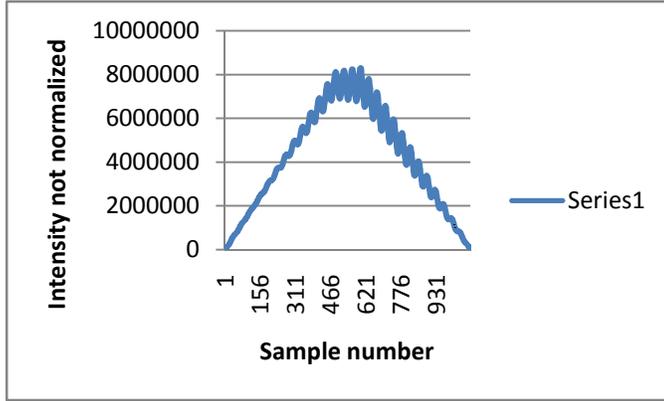
Figure 2.21. Cross-correlated signal: upstream signal with the signal pre-stored in the memory

Figure 2.21 shows a graph which is the resultant of applying cross-correlation between the upstream and memory signals. The sample number (600), which is an average index achieved from a number of tests, is higher in this graph comparing to the previous one and the traveling time with the same sampling time is again the peak time (4.8ms) plus the stabilization time. Equation set (2.6) correlates these times together.

$$T_{offset} = 8.48 \ ms \qquad\qquad (2.6)$$
$$T_{travelup} = 4.8 \ ms$$
$$T_{traveldown} = 4.784 \ ms$$
$$T_{up} = T_{offset} + T_{travelup} = 13.28ms$$
$$T_{down} = T_{offset} + T_{traveldown} = 13.264ms$$

Having the times required for the necessary calculations: $T_{travelup}$ and $T_{traveldown}$ (obtained according to the index achieved from the cross-correlation of the pings traveling upstream and downstream respectively), the velocity of water is given by the equation 2.7.

$$v_{cal} = \frac{T_{up} - T_{down}}{T_{up}.T_{down}} \cdot \frac{L}{2} = 0.36m/s \qquad\qquad (2.7)$$

And in order to assess the operation of the whole system, relative error (Valera, Lee et al. 2009) is calculated by 2.8:

$$E\% = \frac{v_{act} - v_{cal}}{v_{act}} * 100 = \frac{0.4 - 0.36}{0.4}\% = 9.16\% \qquad (2.8)$$

This error could be diminished considerably over distance as the difference in the time of travel between the two direction (up/down stream) will be significantly higher so that there will be higher resolution in calculating the time delay. Therefore, more reliable results with less error for the velocity of water will be achieved. Also the multipath effect in the shallow tank could not be totally avoided. Moreover the reference value of 0.4 m/s hast error in itself as the time was measured using a stopwatch and styrofoam floating on the water.

Narrow width of the tank could have caused reflections and multipath errors (Attarsharghi and Masek 2013A). This was avoided by selecting a suitable period of the transmitted signal and accordingly a correct location of transceivers.

2.5 Conclusion

Our system, in which the synchronization is carried out by a precise clock, consists of the driver at the transmitter and an amplifier at the receiver which are preprocessing the acoustic signals of the piezoelectric transducers. The system is deployed in a flow tank. In the experiments, transducers were located in-line with the flow of the water in the tank and the acoustic pings were traveling in or opposite the direction of the flow. Thus, the velocity of the water could be estimated by knowing the acoustic pings' traveling time and also by knowing the distance of the transducers from each other which can be given by the GPS. According to the adjusted reference value for the velocity of the water, the system measures this value with a reasonable error. This is due to the

proper design of the filter, which eliminates the noise of the ambient, especially from the motor that intervened with the acoustic signals. Also, the possible problems that could have been arisen due to the narrow width of the tank were successfully avoided by selecting a proper period for the transmitted signal and a correct location for transceivers.

Therefore, the design of the filter, amplifiers and the whole system can be easily adjusted to suit the channels of water in the ocean. This will be proved in our future works and will be shown that this technique is a prospective method for the in-situ real-time monitoring of the ocean current.

Contribution of this paper has been the practical proof of the effectiveness of avoiding multipath effect. Comparisons with other methods have been described in the Appendix 4.

Chapter 3: Design Criteria and Practical Insights into an Underwater Current Measurement System along with Simulation Results of a Real-Case Scenario in the Northwest Atlantic Ocean

Samareh Attarsharghi

A version of this chapter was published in:

3.1 Abstract

Acoustics have been used in underwater communication and environmental sensing for a century. Sound waves propagate well in water; however, the marine environment poses many challenges to this phenomenon. Designing and deploying an underwater acoustic sensor network has always been a challenge due to the inhomogeneity of the propagation medium. In this paper, a background theory of the underwater sound propagation is provided followed by practical observations and insights into innovative ideas achieved in a lab-scale prototype which assisted in overcoming these challenges. These observations are used to propose a large-scale deployment strategy in the Northwest Atlantic region. Bellhop simulation results provide evidence of the effectiveness of a large-scale system design. This work is focused on finding optimal positioning of the acoustic sensors in the sea while minimizing the multipath effect at the receiver. In addition, the process for precise current speed measurement in a laboratory environment has been explained which elaborates on the practical aspects of a large-scale network deployment in the ocean. The Doppler effect, caused by the motion of the transducers due to wave motion in the sea, is also considered and analyzed for signal processing needs.

3.2 Introduction

Monitoring the marine environment is a subject of interest to many businesses including offshore and shipping industries. As icebergs are a threat in the North Atlantic region, many researchers have tried to propose solutions to minimize the risk of iceberg collisions. Among these solutions, iceberg trajectory modelling such as Turnbull et al. (Turnbull, Fournier et al. 2015) and Eik (Eik

2009) are examples of iceberg drift predictions so that the related industries manage to avoid collisions.

According to Eik (Eik 2009) currents, specifically, are the most important factor for iceberg drift modelling. Eik also mentions a poor quality of available current velocity data for their model. The importance of a robust real-time in-situ current data is reinforced in Turnbull et al. (Turnbull, Fournier et al. 2015) as they also had difficulty in modelling and collecting data for their iceberg forecasting operation. Thus, it is extremely important to monitor and measure the velocity of the current accurately, as the precise sets of current data provide researchers the ability to model and predict the trajectory of icebergs.

Urick (Urick 1983) reports that the onset of the interest in using underwater acoustics and sonar waves in detecting icebergs was in the early 20th century. Later on, acoustic waves were used to detect submarines or other applications including data communication for ocean monitoring (Groen, Sabel et al. 2001), (Gough and Hawkins 1998) and (Chapman, Wills et al. 1999). Acoustic waves have also been used for ocean monitoring and current measurements. There are a number of methods to measure the currents in the ocean that can be grouped into two major categories. The first category is remote sensing techniques, such as radars (Paduan and Graber 1997). This technique only measures the surface ocean current and not the current at the desired depth. Examples include the National Oceanic and Atmospheric Administration (NOAA n.d. A) and Ocean Motion (NASA n.d.B) section of the National Aeronautics and Space Administration (NASA). These organizations provide online real-time surface current databases freely available to the public on their web sites. Data related to the surface current is usually gathered using buoys, drifters and floats, high frequency radar and satellites. But surface currents are not the

currents moving icebergs. Instead a near surface current, or shallow current, is the data needed for modelling (Turnbull, Fournier et al. 2015).

The second major category of the current measurement technique is point natured methods and is mainly performed by tools called acoustic Doppler current profilers (ADCP) (Dinehart and Sacramento 2003). This method also has the drawback of not being able to provide the average magnitude across an area of interest. According to NASA's report on gathering methods (NASA n.d.A.), the main instrument for profiling the current in depths of several hundred of metres is still the ADCP, which is a single point current meter. NOAA also uses some deep water ocean drifters (NOAA n.d.C.) which go to 2,000 metres under water. Every 10 days, the drifters come to the surface in order to communicate wirelessly with the shore. The main disadvantage of these drifters is that they cannot provide real-time data. Furthermore, drifters can sometimes be lost or difficult to track especially in harsh sea conditions. Woods Hole Oceanography Institution (WHOI n.d.) is another organization that is actively involved in ocean related researches. It has moored profilers that provide an inventory of the current in a column of water using acoustic current meters. The recorded data is only downloadable when the instrument is recovered and again is not a real-time set of current information. Rossby (Rossby 2016) has done a review on the use of ADCP and floats.

As the previous methods of ocean current measurement are not providing data at the desired depths, this paper proposes a technique for measuring the actual real-time value of the average current that can be deployed in a large section of the ocean. It consists of anchored acoustic sensor nodes along with stationary wireless devices for inter-node communications as well as communications with the shore station. With this setup, it would be possible to measure the shallow water current at any desired depth while avoiding the problems encountered with deep

water drifters. A detailed explanation on the function of this setup and how much of the operations are performed under the water or in the air, as wireless signals, can be found in section 3.4 PRACTICAL COMPLICATIONS AND SOLUTIONS FOR IMPLEMENTATION.

As a small-scale prototype, the proposed method was tested at Memorial University's Fluids and Hydraulics Laboratory (FHL). The design of the experimental setup is presented in Attarsharghi and Masek (Attarsharghi and Masek 2014) which uses the transit time method (Liptak 2003; Lynnworth 2013) along with the cross correlation technique (Shin and Hammond 2008). This setup is appropriate for an accurate measurement of shallow water current. Based on this setup, a large-scale system could be deployed in open water. To the best of the author's knowledge and according to the recent researches and reviews on the ocean current measurement techniques (Pandian, Emmanuel et al. 2010; Zuckerman 2014; Wilson, Heitsenrether et al. 2015), the complications of deploying such a system have never been addressed and reported in previous works.

As a result, this paper analyzes the achievements of the laboratory setup that were obtained from previous experiments, investigates deployment complications, and explains how the limitations in a lab-scale design were overcome. Techniques to make the laboratory outcomes applicable for the ocean environment are also proposed.

It should be mentioned that Dushaw et al. (Dushaw 2009) have also investigated the applications of acoustic signals in observing the ocean environment including ocean tomography. In ocean tomography, the average speed of sound is inferred from the time of flight and variations in the speed of sound are measured in order to calculate the changes in ocean temperature. A rule of thumb in this method is that a 1°C change in temperature corresponds to about a 4 m/s change in the sound speed (Valera, Lee et al. 2009). Although this technique also uses the speed of sound

for computations, it is different than the way the underwater sound speed was employed in the measurement discussed in this paper. In tomography, the two acoustic transducers are located very far from each other (100-500 km) and the speed of sound is considered to change over this distance. In this application, transducers are located relatively close to each other (about 3 km) as the wireless devices limit the distance among transceivers, so that the temperature and consequently the speed of sound was considered to be steady and invariable in the target region. According to the ocean global data available in web sites such as NOAA (NOAA n.d.D.), this is a confident assumption.

The rest of this paper is organized as follows. Basic theories of underwater sound propagation are explained in THEORY with specific investigation of transmission loss, noise, multipath and the Doppler effects and solutions to avoid their unwanted effects in the measurements. The research contributions are presented in (section 3.4) PRACTICAL COMPLICATIONS AND SOLUTIONS FOR IMPLEMENTATION. First is the investigation of the practical aspects and limitations (e.g., electronic instrument limitations) faced in the lab-scale prototype and proposition of some solutions in order to make the design expandable and applicable in a large-scale area at desired regions in the sea. In this section, the optimal depth of the acoustic sensors in the target region of the ocean (which is offshore St. John's, NL, Canada, close to oil platforms) is proposed. Also, by means of Bellhop simulations (Porter 2011) both eigenrays and transmission loss of the acoustic signals using actual hydrographic data are plotted. Thus, the effectiveness of the node placement scheme is proven with the simulation results. The Doppler effect, which is negligible in this case, is also discussed in the same section. Finally in CONCLUSION, research results and future steps are discussed.

3.3 Theory

The underwater acoustic communication environment is different than the terrestrial environment with specific characteristics that should be taken into account while designing a network. Underwater acoustic channels are characterized by factors such as transmission loss, noise and multipath effect. Challenges with these phenomena were encountered in the lab-scale prototype and innovative solutions found, which is the basis of the proposal for a large-scale system. Their definitions along with related graphs are explained in the following sections.

3.3.1 Transmission Loss

Transmission loss or propagation loss (TL) is the loss in intensity in decibels (dB) and is described by the Urick (Urick 1983) propagation model in Equation (3.1) and depicted in Figure 3.1. TL is a function of the distance (d [m]) between the transceivers and the frequency (f [kHz]) of the acoustic waves. Medium absorption coefficient is shown by α (dB/km). The geometric spreading loss (χ) is of two types: spherical ($\chi = 20$), that characterizes omni-directional point source in deep water communications, and cylindrical ($\chi = 10$), which characterizes horizontal radiations in shallow water communications. The cylindrical χ is used in the calculations despite the fact that the transducers are omni-directional. Actually in theory, a point source of spreading energy means a source of spherical scattering, but it is not considered as such because, first of all, the area of the ocean where the systems is deployed, which is called Jeanne d'Arc Basin, around the oil platforms is considered as shallow depth (70-80 m) and is not an unbounded medium. Second, this medium is not a homogeneous medium, and the speed of sound varies between the channels because of the varying temperature and energy. Sound channels also trap

energy. So the transducers tend to radiate energy like the surface of a cylinder within the channel of the water.
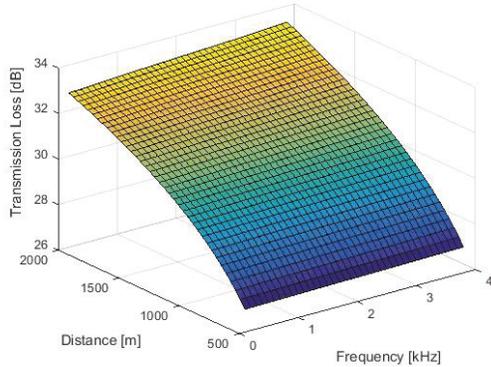
Figure 3.1: Transmission loss of intensity (dB) between transceivers located at various distances (m) from each other.

$$TL(d, f) = \chi . log(d) + \alpha(f). d \times 10^{-3} \tag{3.1}$$

Transmission loss increases with frequency and distance. These facts are used to design the large-scale current measurement system.

3.3.2 Noise

Noise is of two types: first, the ambient noise which is related to hydrodynamics like wind and rain, and second is manmade noise caused by shipping activities and machinery such as pumps (Stefanov and Stojanovic 2011). In the small-scale laboratory experiment (explained in the next section), a pump noise caused by the machine, used to run the water in a tank, was specifically experienced. This noise was successfully removed by proper filtering, which is discussed in (Attarsharghi and Masek 2014). A set of empirical formulae for the power spectral density (psd) of the noise was first defined in Coates (Pompili, Melodia et al. 2009) and is expressed in the set of equations in Equation (3.2) in dB re μPa/Hz in which f is the frequency in kHz. Turbulence noise is N_t (dB re μPa/Hz) which is effective in frequencies lower than 10 Hz; N_s (dB re μPa/Hz) is shipping noise, with shipping activity $0 \le s \le 1$, for a range of frequencies between 10 Hz to

100 Hz; N_w (dB re µPa/Hz) is wind noise, with wind speed in m/s, which is effective in a wide range of frequencies 100 Hz-100 kHz; N_{th} (dB re µPa/Hz) is thermal noise for frequencies higher than 100 kHz; and w is the wind speed (m/s).

$$10logN_t(f) = 17 - 30\log(f) \tag{3.2}$$

$$10logN_s(f) = 40 + 20(s - 50) + 26\log(f) - 60\log(f - 0.03)$$

$$10logN_w(f) = 50 + 7.5w^{0.5} + 20lof(f) - 40\log(f + 0.4)$$

$$10logN_{th}(f) = -15 + 20\log(f)$$

Stojanovic (Han, Zhang et al. 2013) sketched the psd for various wind speed and shipping activity and concluded that there exists a general linear approximation in logarithmic scale to substitute all these four components. The generic linear format that is sketched by the same author can be formulated here by Equation (3.3) and is sketched in Figure 3.2. This approximation is used in the calculations for a large-scale design of the current measurement system.

$$10logN(f) = 95 - 15 * log(f) \tag{3.3}$$
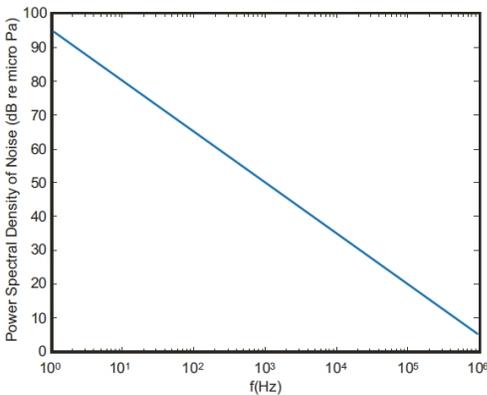
Figure 3.2: Demonstration of the approximation of ambient noise power spectral density (dBre µPa/Hz).
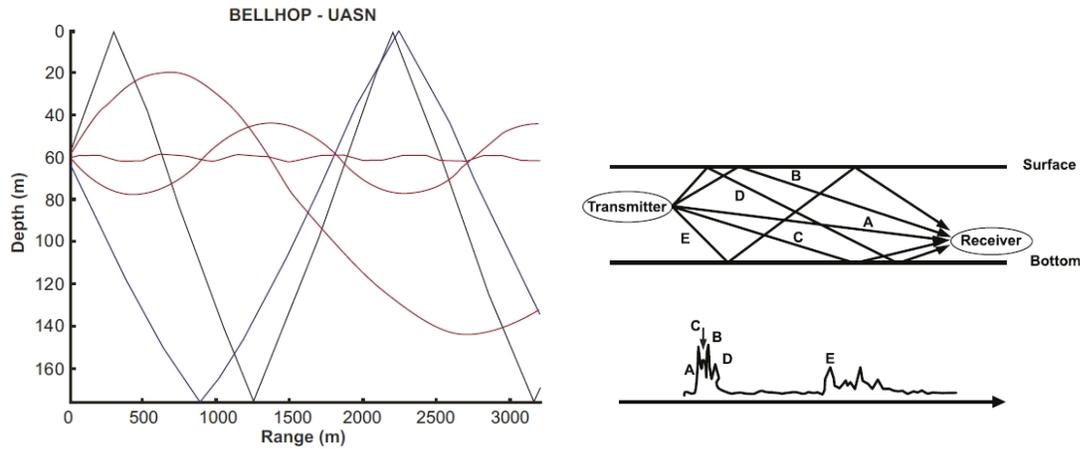
Figure 3.3: Multipath effect. Left: Eigenrays sketched in Bellhop using hydrographic data for the ocean condition from Fisheries and Oceans Canada (Fisheries-and-Oceans-Canada 2015). Right top: schematic diagram of the multipath phenomenon; A to E are different paths. Right bottom: Multipath intensity profile of the rays travelling through the A to E paths (Lurton 2002).

3.3.3 Multipath

Multipath is formed because of the sound ray reflections from the surface and bottom and also because of refractions, which are due to the sound speed variability that is a result of changing temperature, salinity and pressure with depth and location. For the sound refractions, rays tend to bend toward the region in water where the sound speed is lower according to the Snell's law (Jensen, Kuperman et al. 2011). In Figure 3.3, eigenrays, which are red, manifest the refraction effect and the other two colours are showing the reflection effect.

Figure 3.4 shows that the speed of sound increases with the increase in temperature and pressure. In the thermocline zone, temperature decrease is the reason of the decrease in the sound speed (Etter 2013) but deeper in the isothermal zone, the pressure is the main factor in the sound speed increase.

55
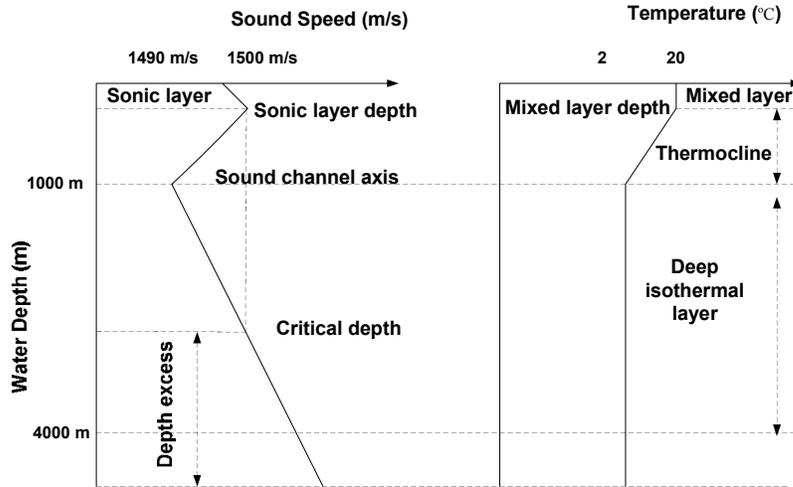
Figure 3.4: Left: Sound speed profile schematic. Right: Temperature vs. depth in the ocean.

According to Jensen et al. (Jensen, Kuperman et al. 2011) and Stefanov and Stojanovic (Stefanov and Stojanovic 2011), an intensity loss is associated with the sound ray reflections (about 3 dB from the bottom). So, if the rays could travel a straight path, they face less intensity loss and arrive sooner at the receiver. This fact along with the whole concept of multipath effect is being used throughout this paper and a solution is shown to eliminate this unwanted effect in the experimental results using the sample window technique. The technique proposed for the large-scale system deployment and an optimal depth positioning idea are described in PRACTICAL COMPLICATIONS AND SOLUTIONS FOR IMPLEMENTATION.

3.3.4 Doppler Shift

Transmitters and receivers move with the waves and the flow of the current. If v_s is the speed of the transmitters' movement in m/s and v_r is the receivers', then the Doppler shift phenomena causes a change between the emitted frequency (f_0 in [Hz]) and the observed frequency (f in [Hz]), which is associated to these movements (Gill 1965) and is expressed by Equation (3.4). In Equation (3.4), c (m/s) indicates the speed of sound in water. The Doppler shift could actually

56

affect and intervene in high rate data transfers in acoustic communications. But as proven in the next section, and as the acoustic transactions in this case are not considered as a high rate communication in the current measurement system, this shift is considered to be very small and can be totally neglected in the current monitoring process.

$$f = \frac{c+v_r}{c+v_s} f_0 \qquad\qquad (3.4)$$

3.4 Practical Complications and Solutions for Implementation

A lab-scale prototype of a current measurement system has been designed and implemented, with the schematic sketched in Figure 3.5, based on the transit time method and cross correlation technique along with synchronization of two acoustic nodes. The procedure in the lab scale prototype is described here in order to show that the similar procedure can be followed in the field between each pairs of nodes of the proposed designed networks of Chapter 4. It should be mentioned that one of the network's basic cells are shown in Figure 3.6. According to the schematic diagram, the synchronization phase is performed wirelessly outside the water. The modules which are involved in the synchronization phase are GPS (synchronization unit in Figure 3.5) and ZigBee units (wireless communication module in Figure 3.5). The underwater communication units, which consist of the transceiver and their drivers that are connected to the wireless modules, receive the commands from the wireless devices and perform the acoustic communications. More details about the process are explained later in the descriptions related to Figure 3.6. The lab-scale experiment has been performed in a tank with adjustable flow rate at Memorial University's Fluids Hydraulics Laboratory (FHL) and the details of the results are published in Attarsharghi and Masek (Attarsharghi and Masek 2014). This experiment is a basic

block of an expanded system for a larger scale implementation. Communication between two acoustic nodes and the designed driver and amplifier for the transducers have been successfully tested.
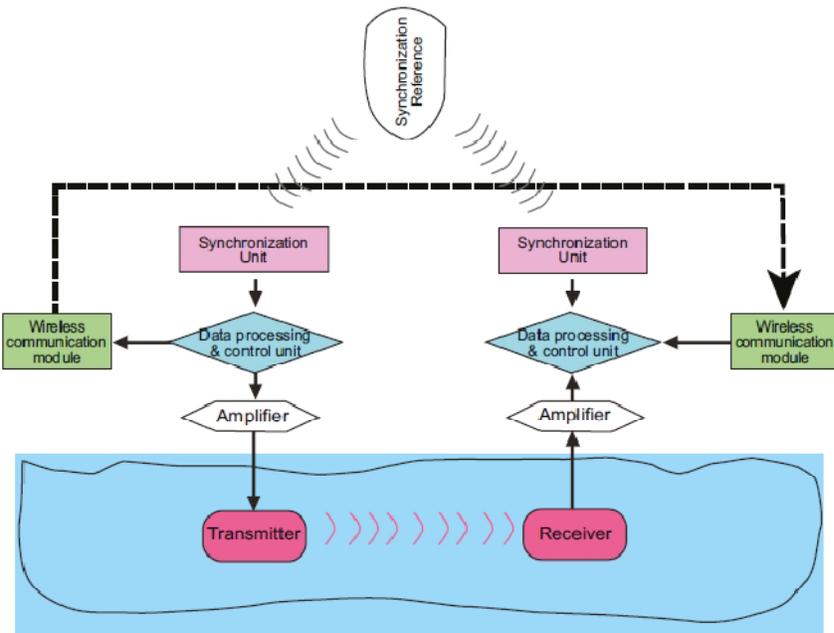
Figure 3.5: Current Measurement System Block Diagram. The wireless modules are Zigbee wireless unit, GPS is the synchronization unit. Calculations and algorithms are implemented and performed with the Arduino microprocessor.

An overview of the logic behind this process is explained in the state machine diagram of Figure 3.6 (top) in which a design of a system that could be implemented in the shallow water at the target area, which is where oil platforms are located at Jeanne d'Arc Basin in the North Atlantic Ocean, is proposed. The wireless Zigbee module at the transmitter side sends wireless signals to the receiver to alert it to be ready for the reception of the acoustic signals. After sending this message, the transmitter projects the acoustic pings into the water at the rising edge of the pulse-per-second (PPS) output of the GPS device (synchronization unit). The receiver, which is in standby mode, records the received acoustic signal, once the PPS signal arrives and the microprocessors at the receiver perform signal processing computations. More details on the

signal processing of the received acoustic waves can be found in Attarsharghi and Masek (Attarsharghi and Masek 2014).

State machine diagram at the receiver

Idle State: The slave node (Receiver Node) stays idle until the issuance of standby command from master node (Transmitter Node).

Standby State: After reception of a predefined command from master node, the slave node enters standby state. In this state the slave node seeks to detect the next rising edge of synchronization signal.

Listening State: Upon detection of the first rising edge of the synchronization signal, the slave node goes to the listening state in which it listens to hear the sonar pulse. As soon as the node begins to listen to its environment, a timer is turned on to measure time delay.

Data Processing State: By detection of the sonar signal, the timer stops counting and some initial processing takes place; and then the slave goes back to the idle state.

Figure 3.6: Top: State machine diagram at the receiver. Bottom: Basic triangular cell for measuring the current vector.

The triangle at the bottom of Figure 3.6 demonstrates the basic block of the acoustic network. Acoustic nodes form triangular cells in order to measure the average vector of the shallow water current. In Figure 3.6 top, according to the process described in the state machine diagram employing transit time method, the vector of current is measured between each two nodes, and the summation of two vectors on each node gives the final current vector at each vertex. This process gives the map of the current in the desired zone. The setup details, including drivers' and amplifiers' design, and the result of calculations in the microprocessor are explained in Attarsharghi and Masek (Attarsharghi and Masek 2014).

Now according to the fact that the prototype is functional, in the following sections, the actual situation and environment in which the whole network is supposed to be implemented is investigated. Practical concerns and solutions that are important factors affecting the functionality of the system in the ocean are also mentioned.

3.4.1 Multipath Effect

In the previous section it was mentioned how multipath propagation occurs. In order to avoid the interference of the signals that the multipath effect causes as well the inaccuracy and error of the measurements mentioned in Attarsharghi and Masek (Attarsharghi and Masek 2013A), the best depth of acoustic sensors deployment is proposed in the following section, which is especially useful in the ocean. The multipath effect in the lab was practiced and overcome with a similar technique which was a proper design of the transceivers' distance from each other, from the walls of the tank as well as from the surface of the water (Attarsharghi and Masek 2014).

3.4.1.1 Best Depth for Deploying the System in Large-Scale along with Matlab/Bellhop

Simulation Results

In this section, the best depth for transducers to be deployed is obtained and, by using Bellhop, (a

MatLab toolbox that deterministically describes underwater acoustic channels (King, Venkatesan

et al. 2010)), a real case scenario in the Northwest Atlantic Ocean, Jean d'Arc Basin region, is

simulated to prove the effectiveness of this new idea. Furthermore, it is demonstrated how this

optimal depth contributes to less measurement error as well as less energy consumption.

For the large-scale system simulations, hydrographic data for the calculations in the above

mentioned area were extracted from the Canadian Government web site (Fisheries-and-Oceans-

Canada 2015) available at Oceanography and Scientific Data, Atlantic Zone Monitoring section.

Below are the details on the location.

Hydrographic Data: Data view

Station: Station   27

Location: 47.55ºN   52.59ºW

Year: 2015

Using the above dataset for temperature (T [ºC]), salinity (S [psu]) and depth (Z [m]), Sound

Speed Profiles (SSPs) were calculated using Equation (3.5) (Etter 2013) and the graphs sketched

in MatLab (Figure 3.7). Each profile (each color) shows different characteristics of the water

changing with time (called seasons in this thesis). In the equation below, C is the speed of sound

in the water (m/s).

$$C = 1449.2 + 4.6 \times T - 0.055 \times T^2 + 0.00029 \times T^3 + (1.34 - 0.010 \times T) \times (S - 35) + 0.06 \times Z \tag{3.5}$$
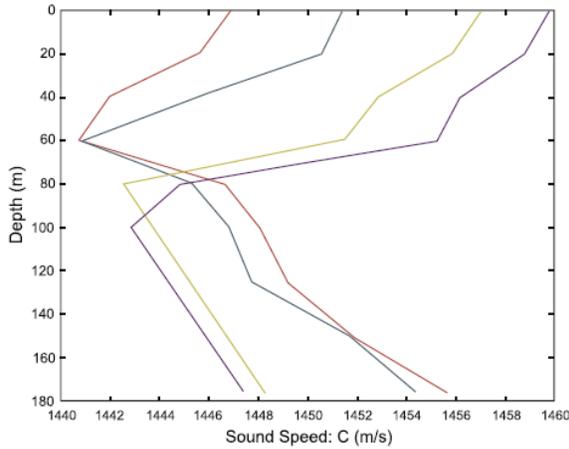
Figure 3.7: Sound speed profile in different seasons in the North Atlantic Ocean.

The SSP graphs define a sound channel, as was mentioned earlier in Figure 3.4. The SSP curves are segmented into short linear sections representing the sequence of layering. Inside the layers, sound changes slightly with a constant rate.

Propagation of sound in such layers is along an arc of a circle (Figure 3.8) and it bends towards the side of the lower speed until entering into the next layer and travelling along another circle arc with different curvature again. The size of the radii of the circles depends on the rate of the sound speed change: the slower it changes, the larger the radius. Sound ray path is composed of connecting sections of the circles. Therefore, the depth in which the sound speed profile is minimum, that is the channel axis in Figure 3.4, is located on the layer with constant sound speed where the change is almost zero. In this layer, circles have a very large radii, which means straight propagation of rays (waveguide) with the least reflection or refraction loss (Wille 2005). The increase in sound speed above the channel axis is due to the temperature and below is due to pressure (Brekhovskikh and Lysanov 2003). Below is the rationale behind this theory.
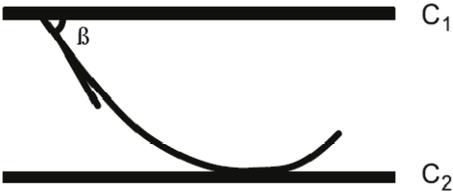
Figure 3.8: Propagation of sound along an arc of a circle.

The curvature is defined in relation to the grazing angle loss (Wille 2005) (between the ray and the constant depth plane) in Equation (3.6):

$$g_n = \frac{c_n - c_{n-1}}{z - z_{n-1}}, \quad R_{cn} = \frac{c_{n-1}}{g_n \cos \beta_{n-1}} \tag{3.6}$$

Where R is the radius of the curvature (m), g is the velocity gradient (1/s), ß is the grazing angle, c is the velocity of the sound in water (m/s), z is depth (m) and n is the index associated to the layer. Therefore, when the gradient of c is close to zero, the radius is very large.

In the next section, different depth of sources (using the specification of Aquatrans (DSPcomm 2009) transducers) in different seasons (various SSPs) with the environmental conditions at the target area of interest are simulated (Figures 3.9 and 3.10). As can be seen, if the source is placed in the channel axis with the least sound speed, c_{min}, signals arrive faster without undergoing any curvature.
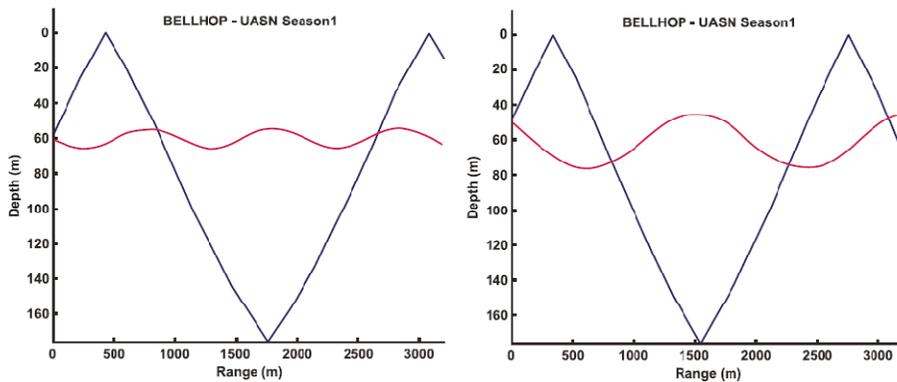
Figure 3.9: Season 1 – Best depth (d) 60 m. Left: f=7500 Hz, d=60 m. Right: f=7500 Hz, d=50 m.
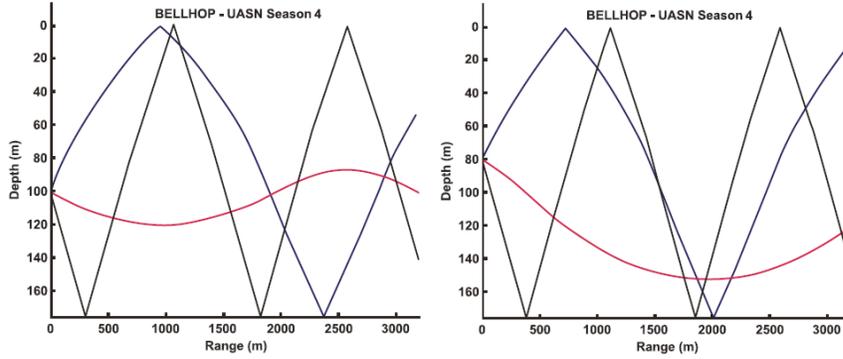
Figure 3.10: Season 4 – Best depth 100 m. Left: f=7500 Hz, d=100 m. Right: f=7500 Hz, d=80 m.

Therefore, for capturing the acoustic rays at the receiver, a sampling-time-window can be defined accordingly which has a width proportional to c_{min} in order to minimize the error caused by multipath propagation. Details about how to calculate the width of this window and when to activate it is described in Attarsharghi and Masek (Attarsharghi and Masek 2014) and was practically proven to be efficient by proper positioning of the transducers during prototype testing. Therefore, the receiver does not capture eigenrays coming after the straight fast rays. So with this optimum depth deployment, the straight path is the only one captured and others are eliminated using this windowing technique, and acoustic signals that reach the receiver face less energy loss due to the fact that there are no reflections or refractions. This means the amount of power required to be consumed in the transmitter part is less than the condition in which there is multipath effect which will results in energy savings. Providing energy is a huge concern in large-scale ocean deployments.

3.4.1.2 Eigenray Plots

Figures 3.9 and 3.10 are simulation results with Bellhop, depicting different depths of transceivers and different SSPs at different seasons. Physical parameters like depth, temperature

64

and salinity result into various speeds of sound in different seasons. Therefore, the performance of the transducers in various underwater conditions is evaluated.

As can be seen, the best depth only depends on the channel axis which is obtainable from SSP. When the transceivers are located in other depths it takes longer for the eigenrays to travel the same path as the multipath affects the rays' routes. Therefore the whole measurement system deflects from its optimal functionality. This idea could be applicable in large-scale as well. Details are explained in the following section.

3.4.1.3 Suggestion for Further Improvement

As depicted in Figure 3.8, best depth depends on the water condition (temperature, salinity, etc.) which is a variable parameter. Therefore, in order to always maintain the optimum depth, the nodes should be able to move along an anchor in a fixed column. A propeller which is installed along with the acoustic transducers could handle the vertical movement of the node. The node's microprocessor could control the movements according to the water condition and the related SSP. Therefore the system could be deployed in the ocean for the current measurement application.

In the next sections, after selecting a proper communication range, the transmission loss of the acoustic signals are plotted for AquaTrans transducers used in the lab; the optimum path is also observable in these plots. The reason that lab equipment are used as examples is to show that the setup is expandable in a large section of the ocean.

3.4.2 Sensitivity and Transmission Loss Calculations

Now the intensity loss that acoustic signals face while travelling a certain distance under the water are calculated; various conditions are simulated; and the resultant transmission losses are

plotted. For the distance that acoustic rays travel, a reference inter-node distance must be set: –

3.2 km was chosen as this distance is the range of the wireless modules that were used in the

prototype. This range imposes a limit to the node communications. The ZigBee wireless

modules' specifications can be found in the device's datasheet (Parallax n.d.). In the following, it

is shown how the lab setup, under the proposed new conditions, could be implemented in the

target zone in the ocean and the eigenrays emitted from the source node can reach the set inter-

node distance to be processed and give an accurate in-situ real-time measurement of the current.

In order to continue, Figure 3.11, which is a schematic diagram of the passive sonar equation,

depicts how each sentence in the equation can be calculated (Lurton 2002).
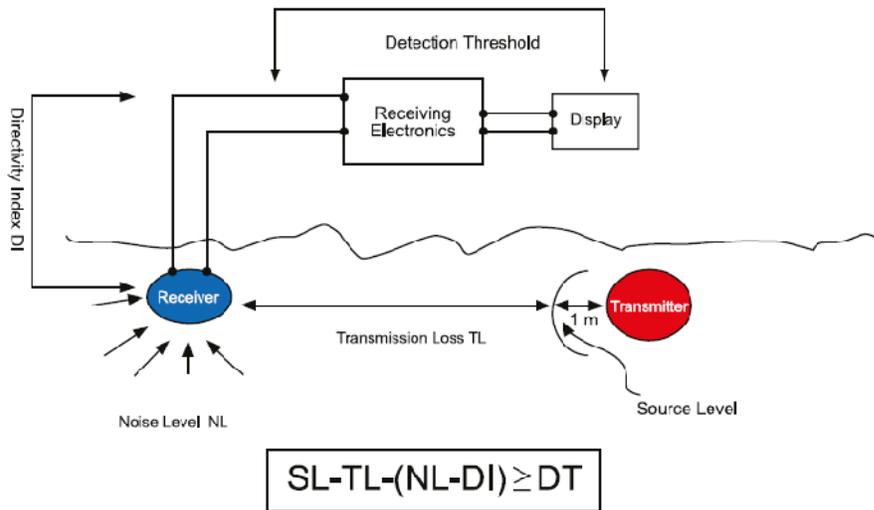
Figure 3.11: Passive sonar equation diagram. SL is the source level, NL is the noise level, DI is directivity index of the transducer, which is zero for omni-directional transducers (in the lab-scale experiment), and DT is the detection threshold (Casari and Zorzi 2011).

Start with the detection threshold in Figure 3.11. For the receiving electronics, the Arduino-Uno

(Arduino-Uno 2013) modules were used in the lab as the interface board. These modules have a

built-in microprocessor (Atmel 2016) with 8 bit A/D converter (ATmega328P ; Atmel 2016). This means in order to have a detectable voltage at the receiver, a minimum voltage of 0.02 V is required. Therefore, other parameters such as distance and transmitted voltage intensity need to be set so that the voltage that reaches the receiver is strong enough to be detected. Having the distance and the intensity of the transmitter set to 350 volts peak to peak (Attarsharghi and Masek 2013B), the conditions for the large-scale deployment are investigated.

For investigating the signal intensity at the hydrophone or the receiver, the electrical circuitry needs to be investigated. In the lab-scale experiments a low noise amplifier, LM1875, was used at the receiver, which is specifically designed for acoustic applications. It was designed to have a gain of 20 which could be cascaded to another similar amplifier, though only the first stage was used in Attarsharghi and Masek (Attarsharghi and Masek 2013B) as the intensity of signal was high enough in the lab. However, as it is mentioned in Attarsharghi and Masek (Attarsharghi and Masek 2013B), the other stage is specifically implemented for very weak signals that is useful in the large-scale conditions and will result in a gain of 400. There is also a band pass filter with a gain of almost 1 with 3 dB ripple. This gain could be designed to further boost the gain if necessary in its pass band. So the overall gain ($G_{overall}$) of the electrical circuit at the receiver which is the product of the gain of the low noise amplifier (G_{LNA}) and the gain of the filter (G_{filter}) (Attarsharghi and Masek 2013B) is defined by Equation (3.7) as:

$$G_{overall} = G_{LNA} \times G_{filter} = 400 \tag{3.7}$$

As the resolution voltage (or the minimum detectable voltage) is 0.02 V, at the analog to digital converter input pin of the microprocessor, this translates to min voltage of $0.02/400 = 5 \times 10^{-5}$ at the receiver output. Therefore the threshold voltage at the receiver (dB) is given by Equation (3.8).

$$VdB_{threshold@receiver} = 20 \times \log(5 \times 10^{-5}) = -86.02 \; dB \tag{3.8}$$

According to Figure 3.12 the passive sonar Equation (3.9) is:

$$SIL_{receiver} = SL - TL - (NL - DI) \geq DT \, (or \; VdB_{threshold@receiver}) \tag{3.9}$$

Where $SIL_{receiver}$ is signal intensity level at the receiver (dB) and DT is the detection threshold (dB) which is equivalent to $VdB_{threshold@receiver}$.

Also below is the sonar Equation (3.10) at the receiver (dB):

$$VdB_{receiver} = SIL_{receiver} + OCRR \tag{3.10}$$

The open circuit voltage response of the receiver (OCRR or OCVR) (dB re 1V/µPa) is a specification of the ultrasonic transducers (refer to APPENDIX for AquaTrans OCRR specifications). Therefore, for the above equation to be true, $SIL_{receiver}$ should be properly achieved.

As mentioned, the amplified voltage at the transmitter in the lab-scale experiment could easily reach $350V_{pk\text{-}pk}$ which is equal to 124 V_{rms}. So the transmitting voltage in dB is defined in Equation (3.11).

$$VdB_{transmitter} = 20 \times \log(124) = 41.86 \; dB \tag{3.11}$$

And according to the specification sheet of AquaTrans (see APPENDIX), transducers have a transmitting voltage response (TVR) of 132 dB at around 7500 kHz.

At the transmitter there is the following sonar Equation (3.12):

$$SIL_{transmitter} = TVR + VdB_{transmitter} \tag{3.12}$$

Where $SIL_{transmitter}$ is the sound intensity level at the transmitter. This means that the sound intensity at the transmitter is 173.86 dB according to Equation (3.13).

$$SIL_{transmitter} = 132 + 41.86 = 173.86 \; dB \tag{3.13}$$
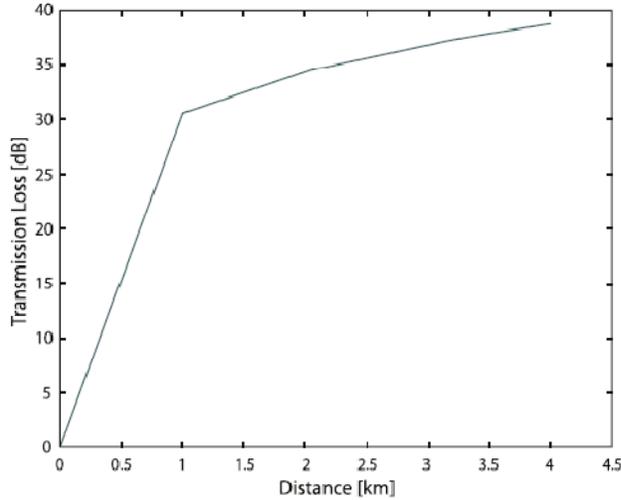
Figure 3.12: Transmission loss vs. distance at 7.5 kHz.

This is the sound level which reaches the receiver at 3.2 km (which is dictated by the limitation of the ZigBee module wireless device) distance of the transmitter.

The performance of the transceivers at 7.5 kHz at which OCRR $_{7.5kHz}$= -190, NL=32.5 dB (Figure 3.2) is investigated. By having the TL formula Equation (3.2) for cylindrical propagation of sound, Figure 3.12 gives $TL_{3.2\ km,7.5kHz}$=37.3dB which from Equation (3.9) leads to sound intensity level of 103 dB according to Equation (3.14).

$$SIL_{receiver} = 173.86 - 37.3 - 32.5 = 104.06\ dB \tag{3.14}$$

So from Equation (3.10) the receiver voltage in dB can be calculated by Equation (3.15):

$$VdB_{receiver} = SIL_{receiver} + OCRR = 103 - 190 = -85.94\ dB \tag{3.15}$$

Sonar equations in this section were adapted form (Urick and PRINCIPLES 1983).
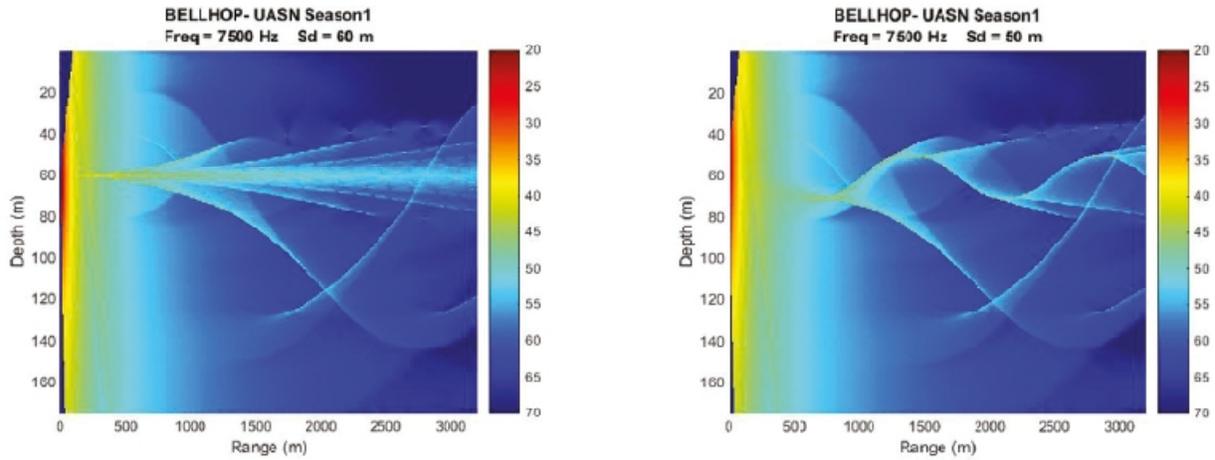
Figure 3.13A: Season 1 – Transmission loss with source or transmitter (sd) in different depths. Left: At optimum depth. Right: At a non-optimum depth.
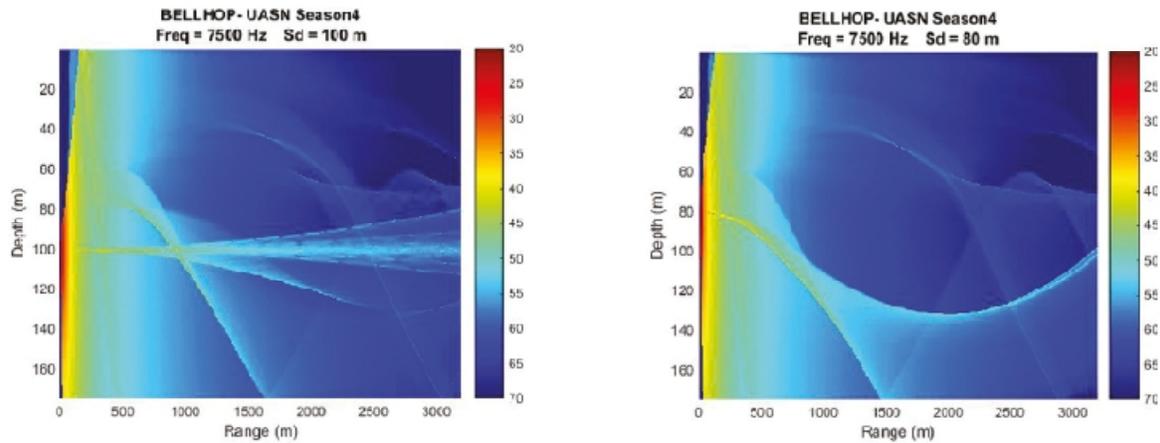
Figure 3.13B: Season 4 – Transmission loss with source or transmitter (sd) in different depths. Left figure shows that if the source is located at the proposed optimum depth, intensity loss is in a range (40 dB in this case) so that the detection threshold criteria at the receiver could be met. In the right figure it is obvious that the waves lose more intensity and take more time to reach the receiver which causes interference for the signal processing phase.
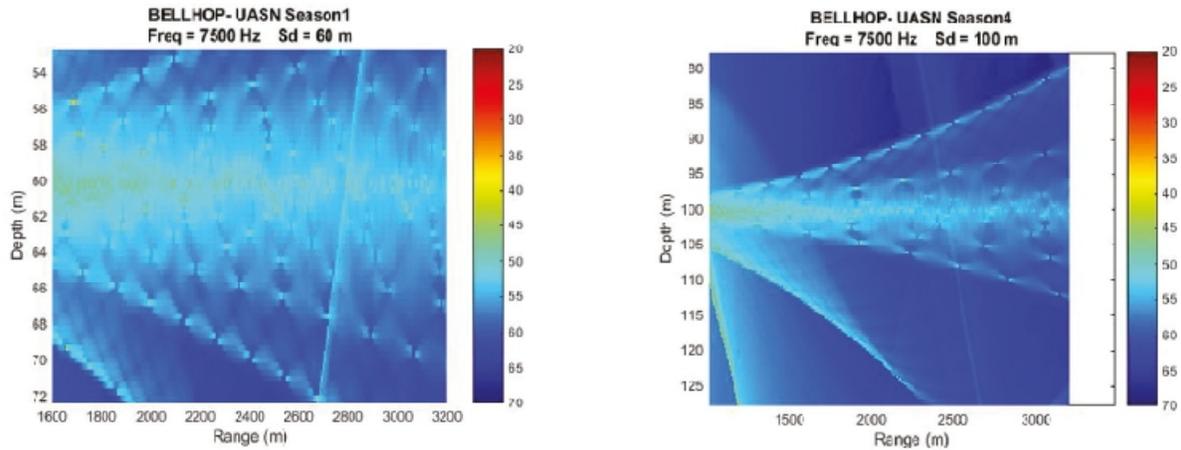
Figure 3.13C: Zooming into the signal intensity at the receiver (located at 3.2 km in this case) showing the intensity loss in optimum depth case for the two different seasons is appropriate to be detected (40 dB loss).

As can be seen $VdB_{receiver}$ is equal to the detectable threshold (-86.02 dB). So this system with the current circuitry design is suitable to be implemented in the open water in large-scale with a node distance of 3.2 km at 7.5 kHz of frequency, if the proposed optimal depth is observed so that signals do not suffer any extra intensity loss. To be able to avoid the inaccuracy and reduce error in the calculations caused by multipath interference of the signals, the right sampling window time needs to be defined similar to the method practiced in the lab.

Simulation results in the next section also confirm that the intensity of the sound waves at the receiver meets the sensitivity criteria of the AquaTrans hydrophones in the set inter-node distance in the ocean.

3.4.2.1 Transmission Loss Plots

According to the simulated environment in MatLab/Bellhop with actual hydrographic data and the previous section numerical analysis, in Figure 3.13 (A and B) TL plots are confirming the calculation results in the section above (intensity loss is about 40 dB which in the similar level of the calculation results is 37.3 dB). This is an additional remark of the effectiveness of the

71

proposed ideas that shows the lab-scale design is deployable in the open water at the target region: Jean d'Arc Basin. In Figure 3.13A (left) transmission loss is depicted in season 1 water condition with the source located at the proposed optimum depth. Intensity loss is small enough (40 dB in this case) so that the detection threshold criteria at the receiver could be met. In Figure 3.13A (right; non-optimum depth) it is obvious that the waves lose more intensity and take more time to reach the receiver which causes interference for the signal processing phase. In Figure 3.13B the same scenario has been simulated but in season 4 which has a different water condition. Figures 3.13A and 3.13B show the similar results for the optimum and non-optimum transceiver depths. Figure 3.13C shows the focused picture of the signal intensity at the receiver in the optimum depths condition in season 1 (Figure 3.13C, left) and season 4 (Figure 3.13C, right).

As can be seen in Figure 3.13, the best depth in each season is observable and, if the source depth is set at that optimum depth, signals at the receiver will be easier to detect without experiencing a severe multipath effect in the large-scale design.

The next section investigates how it is possible to neglect the Doppler effect in the large-scale measurements design.

3.4.3 Doppler Effect

Previously, it was mentioned that the Doppler shift is one of the concerns in propagation of the sound rays. Here it is explained how this interference could be avoided in the ocean current measurement process. Also more details could be found in Appendix 5. First the equations related to the Doppler effect (Equations (3.16) and (3.17)) are defined. In these equations, f is the observed frequency (Hz) and f_0 is the transmitted one (Hz), c is the speed of sound under the

water (m/s), $\Delta v = v_r - v_s$ is the difference between the speed of the transmitters' movement and the receivers' (m/s) and the Doppler effect is Δf (Hz).

$$f = (1 + \frac{\Delta v}{c})f_0 \tag{3.16}$$

$$\Delta f = \frac{\Delta v}{c}f_0 \tag{3.17}$$

As can be seen, the Doppler effect or Δf is proportional to c^{-1} that is roughly 1500^{-1} which is equal to 6.6667×10^{-4}. According to the real-time data downloaded from Ocean Surface Current Analyses Real-Time web site (NOAA n.d.D.), surface current speed is in the order of 1 m/s. So Δv is very small in comparison with c^{-1} and consequently the Doppler effect is very small and negligible. In order to compute the maximum frequency deflection, v_r and v_s could be considered in exactly opposite directions. In other words, transducers could be considered to move with current with the speed of $v_r = 1$ and $v_s = -1$. These values for the speed of current result in $\Delta f_{max} = 4Hz$. As mentioned above, this is a very small deflection and does not affect the computations. So it does not interfere with the signal's receiving process at the receiver. Actually, the Doppler effect in higher frequencies (40 K-3000 KHz) is big enough to be useful in instrumentation like ADCPs.

3.4 Conclusion

The presented work first examined the underwater acoustic wave propagation in terms of losses, noise, multipath and the Doppler effects. Then practical techniques for the deployment of a networked system for ocean current measurement were proposed and elaborated. These techniques have been implemented in the lab-scale experimental setup making it ready for a large-scale system deployment. The precision analysis in calculating the time delay provides a

practical strategy to reduce the measurement error. Also, an ideal depth placement is proposed, based on theoretical analysis, which leads to a new technique aimed to make the lab-scale verified system feasible in open water, with the least measurement error possible. This depth is only dependant to the characteristics of the water and is independent of the type of transducer. Software simulation results were provided, using actual real-time hydrographic data, in order to support the theoretical ideas and expand the lab results to an ocean-scale design of measurement system.

Currently, research on an underwater sensor network for ocean current monitoring is being conducted using the rules developed in this work. While the depth placement was discussed here, the combination and the lateral placements of acoustic nodes, aiming for an energy efficient topology, will be considered in future research.

3.5 Appendix

Below are the transmitting voltage response (TVR) and open circuit voltage response (OCR) of the AquaTrans acoustic transducers used in past lab experiments.
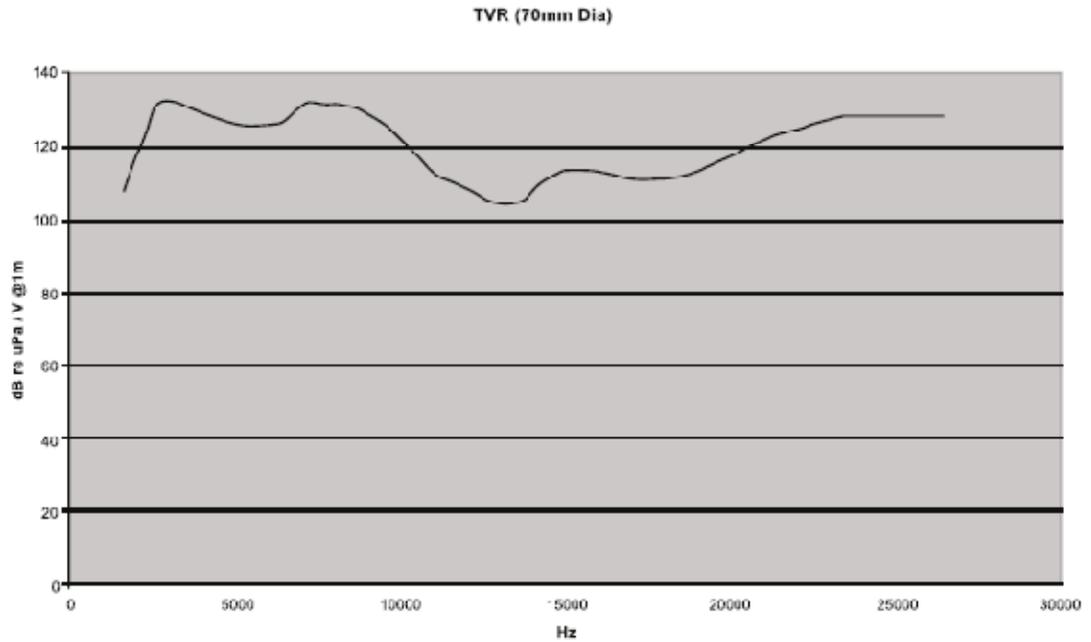
Figure A₃₋₁: AquaTrans transmitting voltage response (TVR); from producer's technical catalogue.
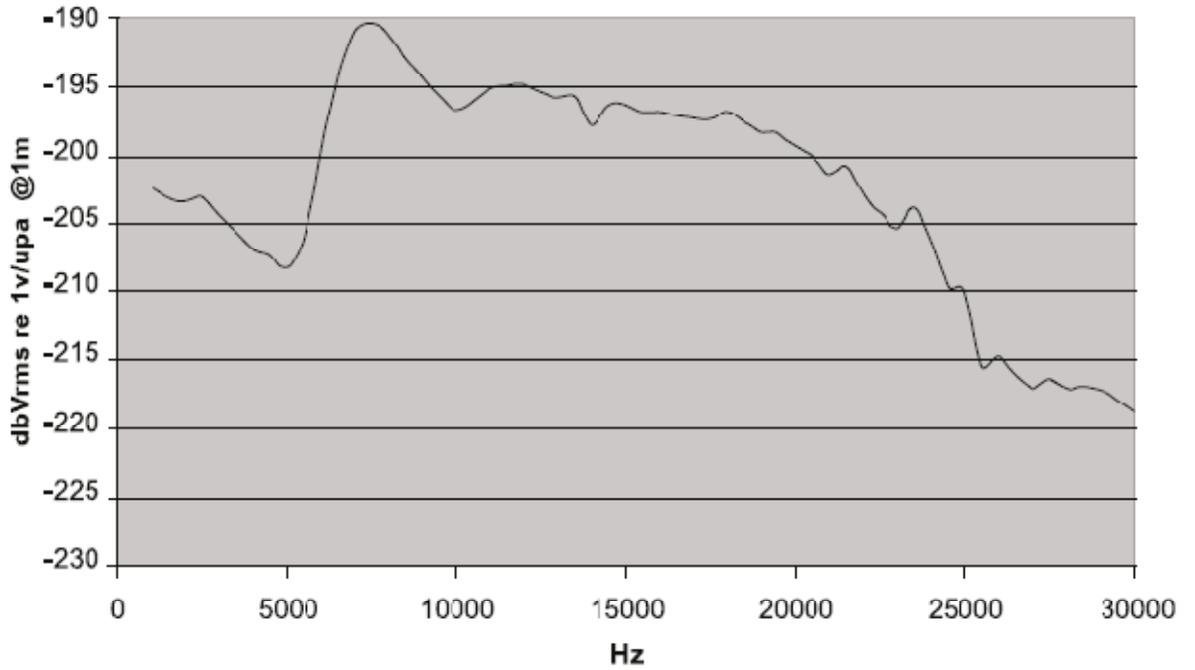
Figure A₃₋₂: AquaTrans open circuit voltage (OCV) response at the receiver; from producer's technical catalogue.

75

Chapter 4: Energy Efficient Architecture Designs of an Underwater Acoustic Sensor Network for Ocean Current Monitoring

Samareh Attarsharghi, Vlastimil Masek

A version of this chapter is in press in:

4.1 Abstract

Providing energy to an underwater sensor network has always been a challenge due to the rough condition at sea as well as the lack of access to deployed equipment for battery replacement. Moreover, the lack of solar energy excludes the use of solar cells in cold oceanic regions. In such harsh conditions, maximizing sensors' life time is an essential goal.

In the area of ocean current measurement, some of the existing methods are mostly limited to measure only the surface current and not the shallow water current, while some other methods measure the speed of water in a vertical column only at one location. There are other systems that measure and store the current data of different locations and depths at the sea over time (few days) so the current data saved in them are not real-time. This study aims to overcome some of these limitations and proposes a real-time measurement method for wide area averaged current. Thus, in this paper, novel underwater sensor network topologies and architectures have been designed and proposed.

These new proposed architecture designs specifically aim to maximize the network lifetime by minimizing the energy demand of the whole network. For this purpose, two types of network topologies, Hexagonal and Square, with two different configurations of with- and without-centre node for each type, have been designed and offered. The method used in the current measurement networks is based on transit time method and could be considered a modified version. Using the new modified measurement method, these novel architecture designs unravel the limitations of the existing current measurement methods. In this paper, the proposed architecture designs' performance has been compared to each other and also their pros and cons have been discussed.

4.2 Introduction

Underwater sensor networks provide robust communication for many applications such as underwater data collection, navigation, prevention of disasters, etc. One of the networks' applications could be precise monitoring of the ocean current. Ocean current measurements are specifically important to both ocean related industries and researchers because the currents affect the global climate (NOAA 2013; NOAA n.d.B.), work in favour or against the marine transportations, carry nutrients (NOAA 2013; NOAA n.d.C.) or steer icebergs (Eik 2009; Turnbull, Fournier et al. 2015).

In order to obtain a vast area real-time measurement of the ocean current, different architecture designs of acoustic sensor networks are proposed. Acoustic sensors are used in this study because sound waves can propagate through the ocean layers over a large distance (Urick 1983). The absorption of sound in water depends on its frequency and if the frequency is sufficiently low (e.g., 57 Hz) then sound can propagate thousands of kilometres (18,000 km) (Brekhovskikh and Lysanov 2003).

Existing methods of ocean current measurement such as remote sensing methods, acoustic Doppler current profilers (ADCPs) and Argos all have limitations for wide-area real-time shallow water current measurement. For example, remote sensing techniques (e.g., satellite and radar) only provide the surface current measurements (Dohan and Maximenko 2010; Paduan and Washburn 2013). ADCPs, on the other hand, measure a point nature profile data of the ocean current. As well, their directional accuracy depends on the accuracy of compass readings. Finally Argos yield the current data which is not real-time because they travel deep under the water for several days before the data stored in them can be downloaded (Fossette, Putman et al. 2012).

As a result, a novel proposed current monitoring technique in this paper aims to overcome these limitations.

The proposed technique in this paper is based on transit time method (Lynnworth 2013). The transit time method is actually used for measuring the speed of sound in water while collecting ocean current features. Computing the speed of sound will be the first step of the proposed current measurement method; called the self-calibration phase (step). The importance of this phase is explained in detail in STRUCTURE OF THE NOVEL ARCHITECTURE DESIGN FOR CURRENT MEASUREMENT UNDERWATER NETWORKS. Then, in the next step the arrangement of the acoustic sensors in a network is addressed. As an introduction to the networks and deployment methods, a review is done on the deployment algorithms. Han et al. (Han, Zhang et al. 2013) have divided deployment algorithms into three groups of static, self-adjustment and movement-assisted deployment (also called dynamic deployment). The static deployment is considered in this work.

Static deployment is the one which is of interest in this research because this technique results in a two dimensional deployment and therefore in saving energy. In fact, the number of nodes for achieving an acceptable coverage in a three-dimensional network is excessively higher than the two-dimensional network which will result in higher energy consumption and more costs. An example would be the three-dimensional network in Xiaoyu et al. (Xiaoyu, Lijuan et al. 2013). Therefore static topology, which forms a two-dimensional network (Han, Zhang et al. 2013), is the proper design for horizontal ocean current monitoring that meets energy saving requirements. Therefore, neither the self-adjustment nor the movement-assisted deployments are the target in this paper as they might result in three-dimensional networks. In fact, for some specific applications of ocean current monitoring, such as iceberg trajectory predictions, a three-

dimensional network is not desirable because a horizontal-section-averaged vector of the current is needed and not a vertical-column-averaged vector.

In terms of dynamic deployment, it should also be mentioned that this kind of deployment is not desirable because moving devices, such as Argos, go to a depth of up to 2,000 metres under the water (Ocean-Drifters 2016; NOAA n.d.E.) and drift for up to 10 days and then come back to the surface to communicate wirelessly to shore. Therefore, not being a real-time system is a drawback of the current measured by these devices. Furthermore, Argos can sometimes be lost or difficult to track especially in harsh sea conditions. Autonomous underwater vehicles are another example used in dynamic deployment which are popular (Mitra, Choudhary et al. 2015). In addition to not yielding a real-time measurement, they are very expensive with high costs associated with their maintenance and fuel.

In order to save energy within the network, another strategy is to maximize the network coverage, which is also an important target of this study. The proposed techniques in the new designs of the network aim for a larger area to be covered by fewer acoustic sensors in order to keep energy demand as low as possible.

In order to reinforce the importance of the power provision for instruments in open water, it should be mentioned that many reports have strived to overcome the limitations of energy in underwater acoustic sensor networks (UASN). Heidemann et al. (Heidemann, Stojanovic et al. 2012) reported the power consumption issue in UASNs through protocol. Another example is in Hu and Fei (Hu and Fei 2010) who suggest an adaptive routing algorithm to achieve an energy efficient UASN. Underwater communication protocols and routing algorithms are techniques to deal with data communication challenges. For underwater monitoring applications, which is the intent of this research, a novel approach is offered in this paper that could solve the problem of

energy deficiency in UASNs efficiently and with less complexity. Minimization of energy consumption in an UASN with data transmission application (which needs a high rate of transaction of data) is different from a network with monitoring purposes (which might need to run once or twice an hour or even less frequently) in terms of topology and architecture design. Challenges faced in designing these two types of networks are different in nature.

Jha et al. (Jha, Wettergren et al. 2015) address a surveillance network energy management (which is a type of data transmission application) where optimization of topology is advised by using genetic algorithm. Jha et al. (Jha, Wettergren et al. 2015) give a target detection model, network connectivity and protocol model, and solve the target detection problem by the equations defined in the modelling. Researchers also proposed a design on data-transmission networks in which power consumption to throughput ratio (Tilak, Abu-Ghazaleh et al. 2002; Etter 2013) and spectrum allocation (Jurdak, Lopes et al. 2004; Jornet, Stojanovic et al. 2010) are the parameters which play important role in the design of the network.

On the other hand, in monitoring-application networks, throughput ratio (the rate at which information is transferred) and update period of data is not important because the whole system is run less frequently. Among the literature (Jurdak, Lopes et al. 2004) is one of the pioneer examples that has addressed the topology of the UASN in order to maximize the network's lifetime. Although the authors use transmission frequency and update period as their design factors, they also use transmission distance and number of nodes in a cluster, which is applicable in a monitoring-application network design. Therefore the present study offers a new scheme by using the concept of increasing transmission distance and reducing the number of nodes in order to minimize energy consumption in the whole network.

Finally, there are important facts that should be mentioned here about the differences between the underwater communication environment and the terrestrial environment. The cost of the deployment and the power demands (Xiao 2010) are the two significant differences of the terrestrial and underwater networks.

These have been the underlying motivations to conduct meaningful research on a novel underwater architecture design in this study. The rest of this paper is organized as follows. In STRUCTURE OF THE NOVEL ARCHITECTURE DESIGN FOR CURRENT MEASUREMENT UNDERWATER NETWORKS, details about the structure of the basic blocks forming the new network architectures are explained. These novel architecture designs contribute to a longer lifetime of the network in order to overcome the dissipation of energy. COMPARISON OF THE PERFORMANCE OF TWO ARCHITECTURE DESIGNS provides an in-depth analysis of the factors affecting the acoustic modem energy consumption in the proposed energy-efficient UASN, such as coverage area and node density. A graphical comparison has also been provided in order to distinguish differences among the proposed designs. At the end, CONCLUSION is provided along with a future work plan.

4.3 Structure of the Novel Architecture Design for Current Measurement Underwater Networks

The design of the current measurement networks is based on experimental results described in (DSPcomm 2009; AquaTrans 2016). A schematic of the lab-scale prototype of the current measurement system is sketched in Figure 4.1. The experiment uses transit time method and cross correlation technique along with the synchronization of two nodes. As mentioned above,

this forms a fundamental block of the design of an expanded network for larger scale implementation.
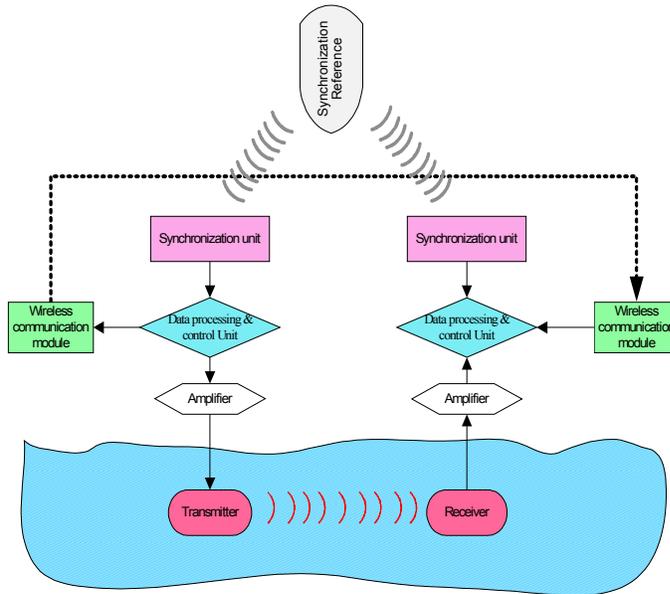
Figure 4.1: Current Measurement System Block Diagram. The wireless module are Zigbee wireless unit, GPS is the Synchronization unit. Calculations and algorithms are implemented and performed in the Arduino microprocessor

Principles of the network design are as follows. The acoustic nodes actually form basics cells of three or four nodes to measure the average vector of the shallow water current. In Figure 4.2 the procedure for the three-node-design is depicted. The vector of current is measured between each two nodes in Figure 4.2 (left). These two vectors are the components of a main current vector that is shown in Figure 4.2 (right). The resultant vector's magnitude and direction are given by Equation (4.1). The experimental setup details including drivers and amplifiers design and the result of calculations in the microprocessor are explained in Attarsharghi and Masek (Attarsharghi and Masek 2014).

A two node system (fundamental setup) was experimentally validated and thus can form a basis for a large scale shallow current measurement system.

4.3.1 The Basic Design: Without Centre Node

In Figure 4.2 (left), the magnitudes of vectors a and b are given from the measurements. Since the placements of nodes are on the vertex of an equilateral triangle, the angel on each vertex is 60°. According to the Figure 4.2 (right), the angle θ should be found from the Equation (4.1) in order to be able to find the magnitude of the resultant vector V [m/s]. The resultant current vector's (V) direction is then θ [$^{\circ}$] relative to the direction of the vector a.

Figure 4.2. Left: Basic cell for measuring the current vector. The two vector components, shown on each vertex, are measured during the process of measurement. Right: the resultant vector, V [m/s], is the original current vector that its components (vectors a and b) are measured on the vertex.

$$V = \frac{a}{cos\theta} \ or \ V = \frac{b}{cos\,(90°-\theta)} = \frac{b}{sin\theta} \tag{4.1}$$

$$\frac{Cos(60°-\theta)}{cos\theta} = \frac{b}{a},$$

In which:

$$\cos(60° - \theta) = [(cos60°)(cos\theta) + (sin60°)(sin\theta)]\big|_{\text{if devided by } (cos\theta);then}$$

$$cos60° + (sin60°)(tan\theta) = \frac{b}{a}, \qquad tan\theta = \frac{\frac{b}{a} - cos60°}{sin60°},$$

84

$$\theta = \arctan\left(\frac{\frac{b}{a} - cos60°}{sin60°}\right)$$

As the process of measurement was described in Figure 4.2 and for a network with Triangle topology, each node in the vertex of the basic cell is once a transmitter and twice a receiver. So there are two velocity vectors at each vertex that are added together to yield the average vector of the current.

This triangular topology is compared with a Square topology. The procedure described for triangular topology can actually be performed for the Square topology which is described in Figure 4.3. The Triangle and Square designs of the network map the current of the target area with three and four separate vectors, respectively.
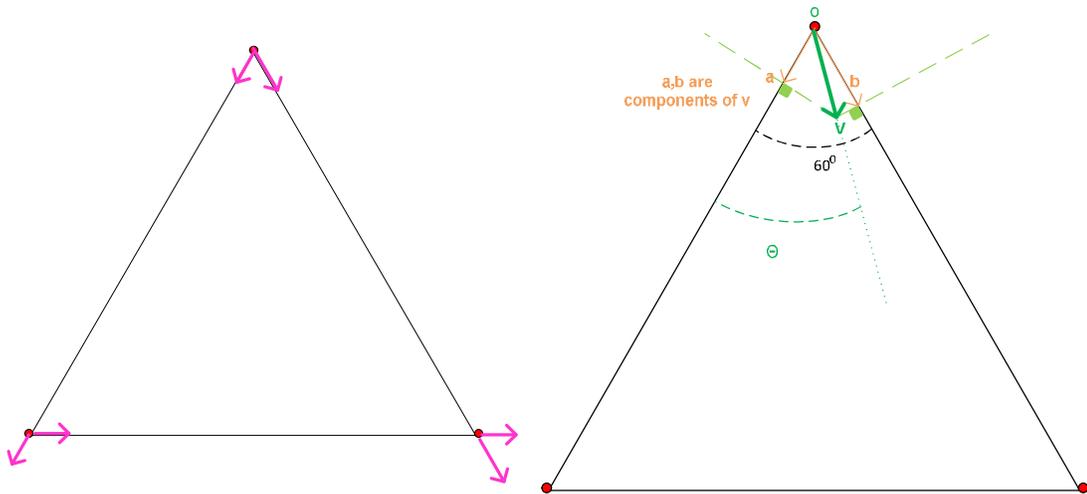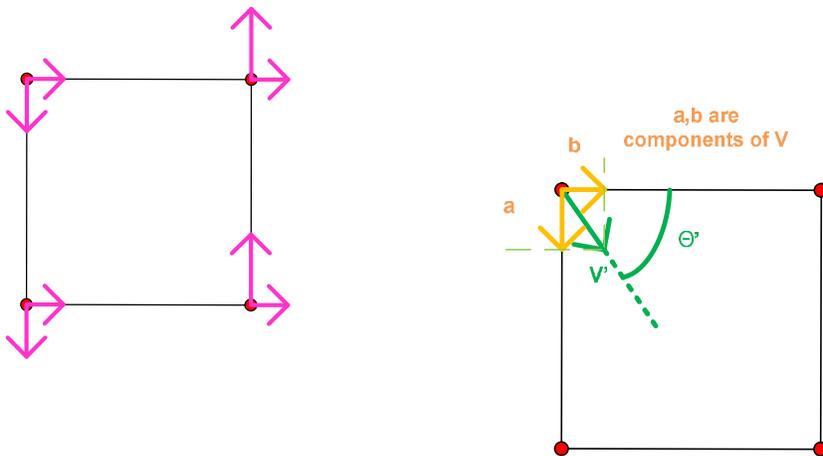

Figure 4.3. Left: Square basic cell for measuring the current vector. The two vector components, shown on each vertex, are measured during the process of measurement. Right: the resultant vector, V [m/s], is the original current vector that its components (vectors a and b) are measured on the vertex.

$$V' = \sqrt{a^2 + b^2} \tag{4.2}$$

$$\theta' = \tan^{-1}\frac{a}{b}$$

The resultant current vector's (V' [m/s]) direction (θ' [°]) is relative to the direction of the vector b.

In this section, the basic blocks of the UASN, which are a combination of either three or four acoustic sensor nodes, have been introduced. In the above introduced basic cells, transit time method is the principle of current measurement. Using the transit time between each pair of acoustic nodes, the average current will be measured. All nodes using this principle of measurement need to be once a transmitter and another time a receiver. The transmitters' power consumption is the main concern, as they use a significant amount of the energy in the underwater environment. Therefore, another method, which is a modified version of the transit time method, along with new basic blocks, is proposed in this paper. In the new proposed configurations an additional node is added in the centre of each of the above configurations. This addition converts the nodes in the vertices of the basic blocks to receivers and only the centre node is a transmitter. This way energy consumption is reduced considerably. In the next sections, details of the development of new architecture designs as well as their pros and cons are explained.

Only Square and Triangle configurations were introduced because only in these two configurations the maximum distance is even between the center and the vertices. It is shown throughout this thesis that the square configuration outperforms the triangle, but because of the fact that triangle configurations give a more accurate value for the average current, as it averages three vectors while Square configuration averages two, it has been introduces in this thesis.

4.3.2 With a Centre Node Architecture Design

In order to make the underwater network sustainable in a large scale, this paper offers new architecture designs.

Instead of measuring the current between the two nodes on the vertex, the current is measured between each vertex and the centre node in the new architecture (Figure 4.4). Traditionally a node at each vertex is both receiver and transmitter. In the proposed design, the centre node (in both Triangle and Square design) is the only transmitter (which consumes 100 times more energy (Partan, Kurose et al. 2007) than the receiver) and other nodes in the vertices are all just receivers. The travel time of underwater acoustic signals is measured at the receivers in the vertices, and thus the current vectors are calculated at the vertex nodes (receiver nodes). These calculated vectors are collected by the centre node to be sent to shore. The centre node can also do the summation and averaging of the vertices vectors and send them to shore. Therefore, in this topology (with-centre-node), sound waves only travel a single direction (despite the transit time in which waves need to travel in two directions) and thus the number of transmitters for each measurement is reduced from two transmitters to just one and thus, energy consumption which is mainly demanded by the transmitters is reduced considerably (Lynnworth 2013; Attarsharghi and Masek 2014). The principle of using this method is based on Equation (4.3) in which V [m/s] is the velocity of the current to be measured, C [m/s] is the speed of the sound which is considered to be determined by a new phase added in the process of measurement called the self calibration method, and t_{up} [s] and t_{down} [s] are the two time readings and L [m] is the distance between two nodes.
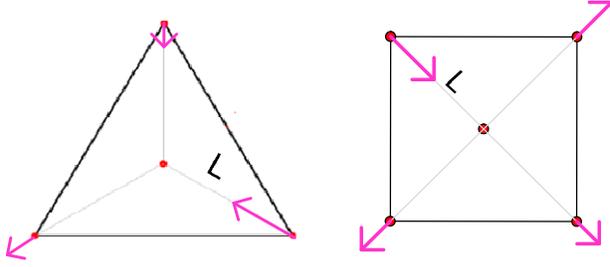
Figure 4.4: Triangle and Square topologies with centre node

According to Equation (4.3), whether the sound travels upstream (t_{up}) or downstream (t_{down}), the speed of the sound (C) in the vicinity of the nodes is needed for the current vector (V) calculations.

$$V + C = \frac{L}{t_{up}} \qquad\qquad (4.3)$$

$$C - V = \frac{L}{t_{down}}$$

The self-calibration phase is introduced in this paper as a solution to measure C which is described in the next section.

4.3.2.1 Self Calibration Phase for the Cells With-Centre-Node

In order to measure the speed of the sound (C), which is needed in the calculations of the water velocity, the calibration phase is introduced. Calibration phase is defined as the procedure of transmitting the acoustic signals between a vertex and the centre node in a cell (Figure 4.5) and calculating the speed of sound at the time of the measurements and in vicinity of the active nodes. This phase empowers the whole network to avoid extra calculations and consequently the energy consumption. Equation (4.4) explains how the value of C is calculated using t_{up} and t_{down}.
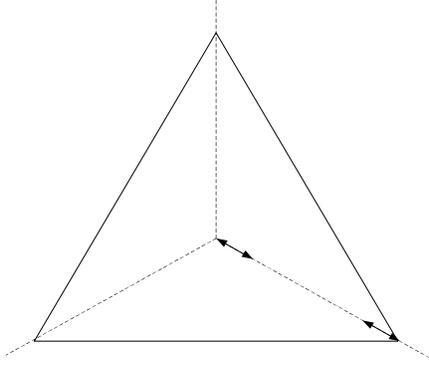
Figure 4.5: Calibration phase

$$t_{up} = \frac{L}{(c+v)} \qquad\qquad (4.4)$$

$$t_{down} = \frac{L}{(c-v)}$$

$$C = \left(\frac{L}{2}\right)\left(\frac{t_{up}+t_{down}}{(t_{up})(t_{down})}\right)$$

The calibration phase, actually, does not need to be done in all of the basic cells and can only be done in one basic cell in a large area, depending on how accurate C is needed to be considered in a region. Knowing the value of C, then by using Equation (4.3) the value of V is obtained. In fact the measured C inherently has the information of still water in it, as if it is L over t_0 which is the travel time needed for sound wave to travel in still water ($C = \frac{L}{t_0}$). Therefore, as can be seen, this phase reduces the necessity of having a transmitter circuitry in all vertices. In the calibration cell the centre node needs to have both receiver and transmitter circuitry. This is how the calibration phase helps with mitigating the power consumption of the whole network. The bigger area C can be considered to be constant, the fewer calibration cells are needed and therefore the more energy is saved.

After the calibration phase, the magnitude of the velocity vector is computed at each vertex by Equation set (4.3) and is reported to the centre node of each cell. Then at the centre node, these magnitudes, which are the components of the main current vector, are added together (similar to the procedure in Figure 4.2 right and of Figure 4.3 right). Thus the resultant vector (direction and magnitude) obtained by this procedure at the centre node is the average velocity vector of the water in the area that the cell covers.

4.4 Comparison of the Performance of Two Architecture Designs

This section elaborates on the advantages of new architecture design (with-centre-node) with extended inter-node distance and lower node density and the effects on the main goals which are energy consumption and area coverage. But before that, the structure of the networks is explained which are constructed by the triangular or Square basic cell. It should be mentioned that in the without-centre-node configuration the method used for current measurement is the traditional transit time method between each pairs of nodes. While in the with-centre-node configuration, the novel proposed method is used, which needs a calibration phase for determining the underwater sound speed in a desired area and after obtaining the sound speed, the water current speed can be measured.

In the Figure 4.6, grids (networks) of combined basic cells (triangular- & Square-cells) are sketched. In the next sections the Square and Hexagon designs will be compared to each other in terms of coverage and node density.
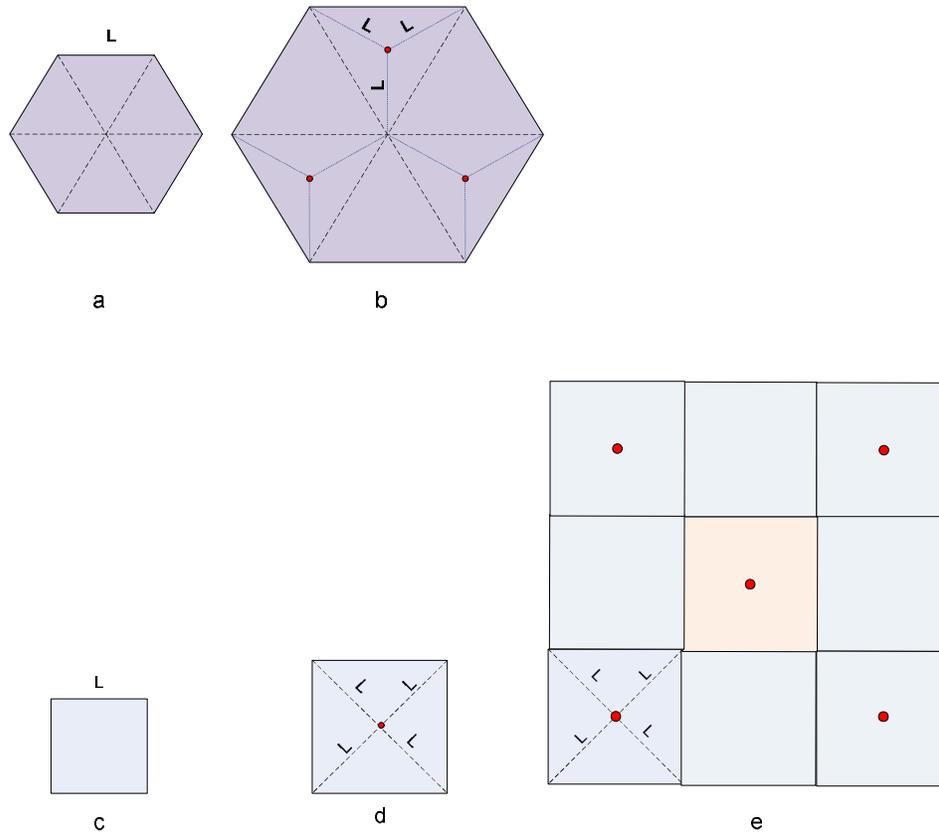
Figure 4.6: Hexagon-cells consisting of six triangular-cells: (a) Basic-triangular-cells without centre node. (b) Hexagon-cells (H-cells) with centre node. Square-Cells consisting of one Square-cell either (c) basic Squares without centre node or (d) Big-Square-cells (S-cells) with centre node which is an extended form of the basic Square cell. The center small circles represent the centre acoustic nodes which are the transmitters. Figure (e) demonstrates two layers of the big-Square-cells network consisting of S-Cells. In order to avoid redundant calculations, every second H- or S-cells has the centre node and not all of the cells.

As it can be seen in Figure 4.6 (b) and (e) in order to avoid the overlap of the coverage of adjacent basic cells and also to avoid the waste of energy in the whole grid, every second H- or S-cell in the extended grid need a centre node and not all of the cells have a centre node. In fact the redundant sensors are eliminated in the grid. Omitting the redundant sensors results in less energy consumption as well. Figure 4.7 shows the two dimensional grids with several layers of H- and S-cells.
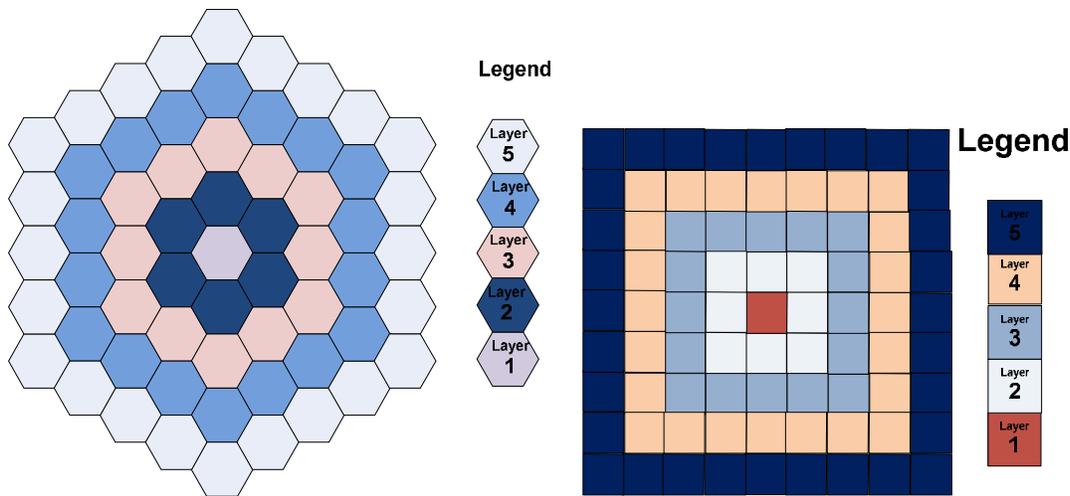
Figure 4.7: Two-dimensional wide area network configuration consisting of H-cells (on the left side of the figure) & S-cells (on the right side of the figure). Legends show the number of the layers.

In the following sections, and according to the two types of H- or S-cells introduced above, they will be referred to as with-centre-node representing the new proposed design and without-centre-node representing the basic design. According to these two types of grids, the tables are set and equations are derived. It should be mentioned that the inter-node distance (L), in the designed UASNs, is limited in length (to 3.2 km, in this paper, which is used for evaluation and comparison of the UASNs' performance) by attenuation of the electromagnetic waves. Electromagnetic waves are sent by ZigBee module (Figure 4.1) and used for synchronizing the transceivers in the designed network. Details about the synchronization process and the length limit are explained in Attarsharghi and Masek (Attarsharghi and Masek 2014; Attarsharghi 2016).

The first subsection explains the coverage area achieved by each of the architecture designs.

4.4.1 Coverage

In order to examine the coverage of the network's parametric equations of the area coverage of the basic cells are presented and compared together.

92

4.4.1.1 Without-centre-node basic cell coverage (in transit time based measurements)

In Figure 4.8, the basic-without-centre node cell is depicted.
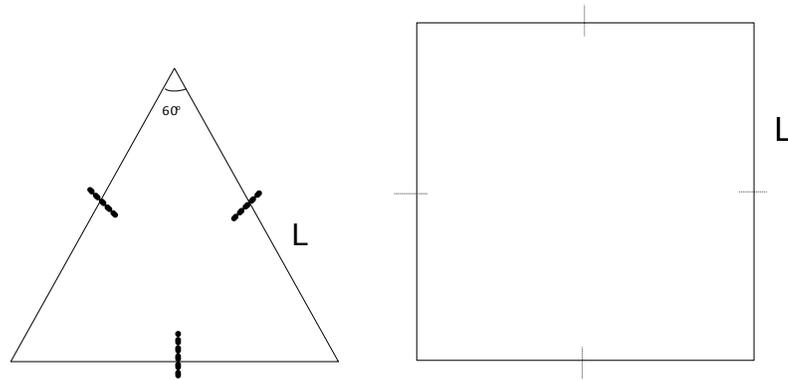
Figure 4.8: Basic cells' coverage for without-centre-node topology.

For the Triangle the area (A_{T1} [m^2]) is expressed by (4.5).

$$A_{T1} = \frac{(L)(L)(\cos 30°)}{2} = 0.5(L^2)\cos 30° \tag{4.5}$$

And for the Square the area (A_{S1} [m^2]) is calculated by (4.6).

$$A_{S1} = L^2 \tag{4.6}$$

Triangular basic cells are combined in order to form the H-cell in Figure 4.9.
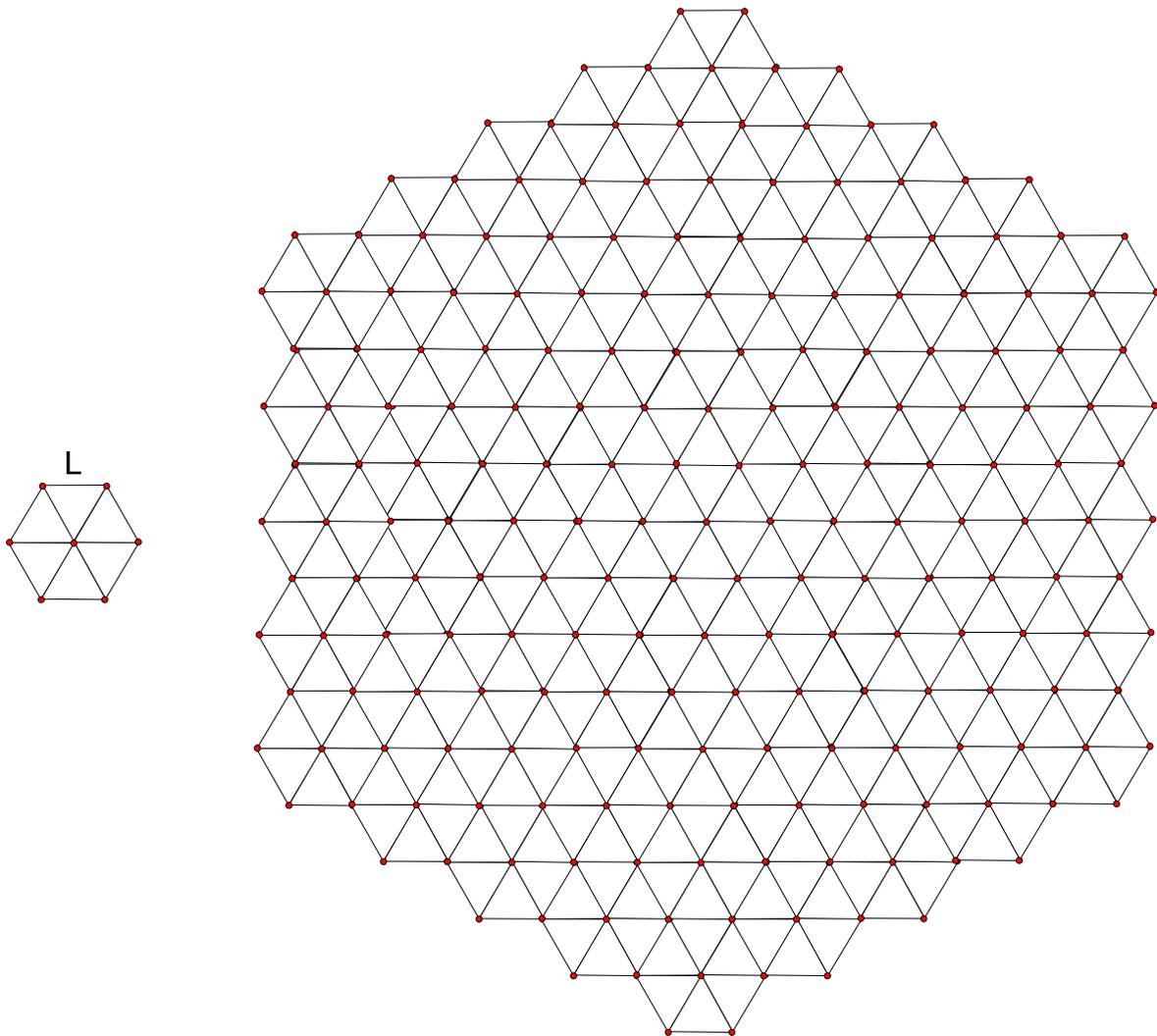
Figure 4.9: Hexagon cell's coverage consisting of without-centre-node basic cells. Dots on vertices indicate transceivers. Left: one-layer H-cell consisting of seven transceivers. Right: five-layer network consisting of 211 transceivers.

With Triangles forming the Hexagon cell, the area of the Hexagon (A_{HI} [m^2]) is given by Equation (4.7).

$$AH_1 = \frac{3\sqrt{3}L^2}{2}$$

(4.7)

In the following section, without-centre-node cell combinations are investigated.

4.4.1.2 With-Centre-Node Basic Cell Coverage (in Modified Measurement Technique with the Calibration Phase Added)

As it can be seen in the Figure 4.9, in the new with-centre-node topology, the inter-node distance is considered the distance between the centre node and each vertex. Therefore, this topology has a larger area which is expressed by the Equations (4.8-4.12).
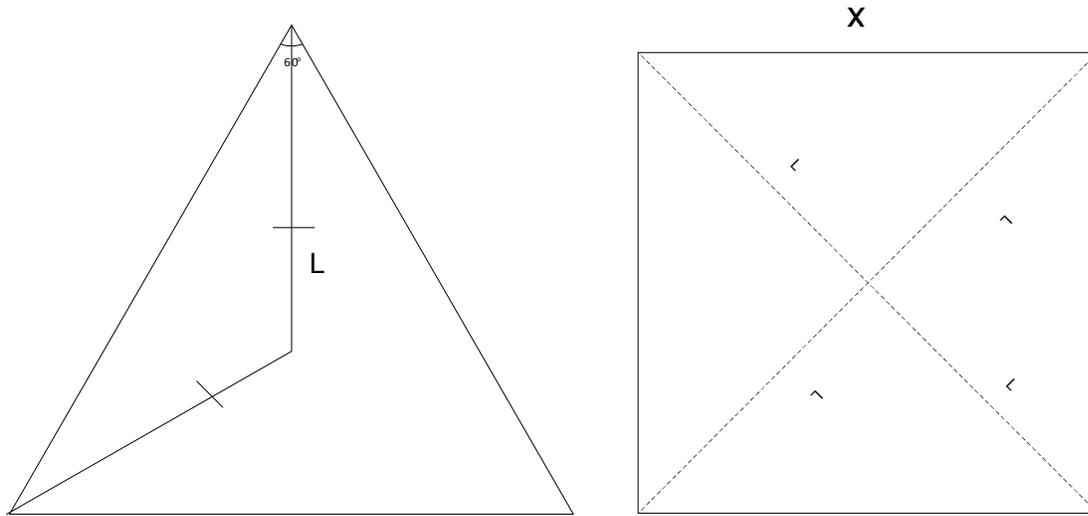
Figure 4.10: Basic cell coverage for with-centre-node topology.

According to Figure 4.10, the Triangle's area $(A_{T2}\ [\text{m}^2])$ is expressed by (4.8).

$$A_{T2} = \frac{(L)(1+sin(30°))(2(L)cos(30°))}{2} = 1.5(L^2)\,cos(30°) \tag{4.8}$$

In order to calculate the edge in the Square $(X\,[\text{m}])$, Equation (4.9) yields Equation (4.10) for the area of the S-cell $(A_{S2}\ [\text{m}^2])$ with-centre-node.

$$X = \sqrt{2}L \tag{4.9}$$

$$A_{S2} = 2L^2 \tag{4.10}$$

95
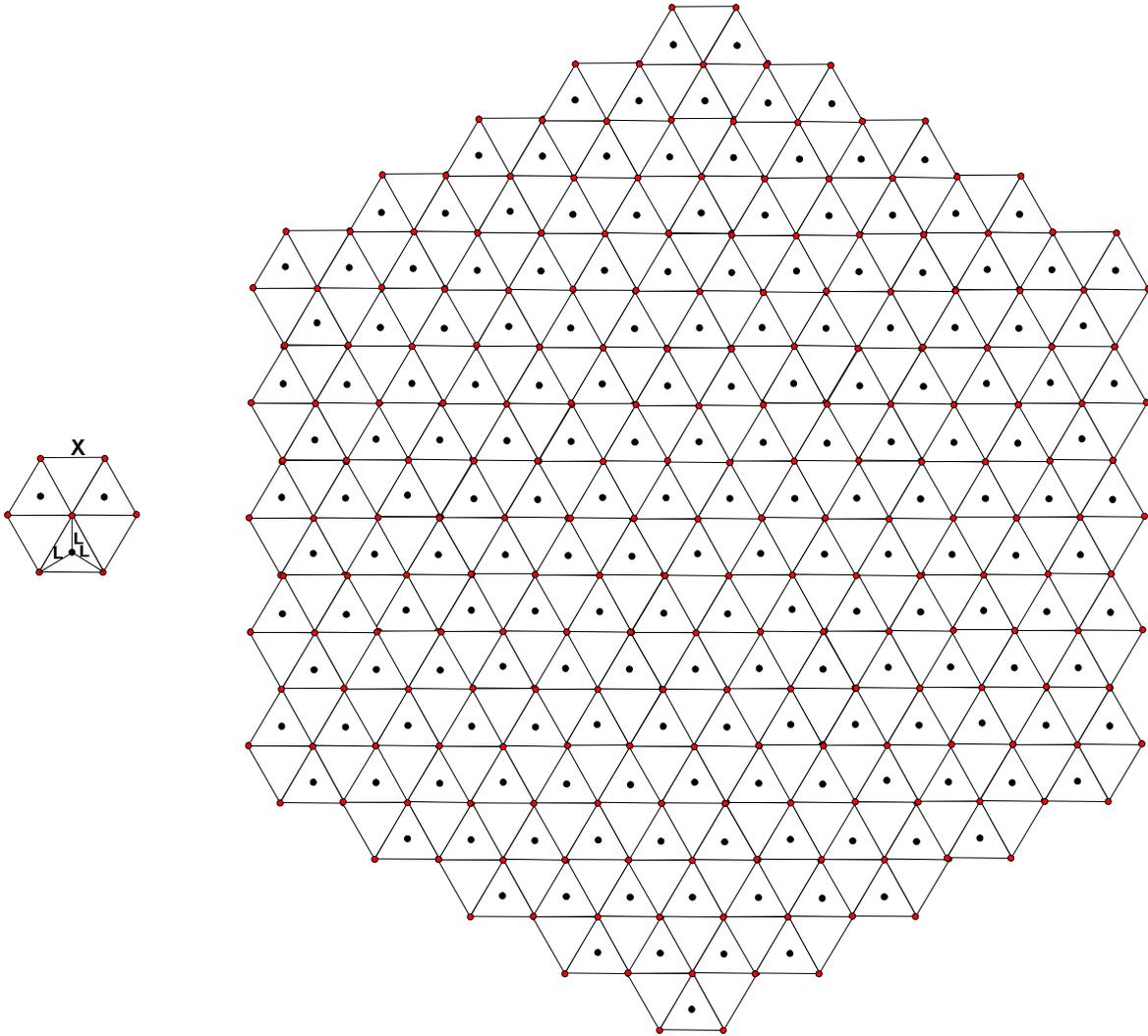
Figure 4.11: Hexagon cell coverage consisting of with-centre-node basic cells topology. Center dots are transmitters that are considered in energy consumption, dots on vertices are only receivers. Left: one-layer H-cell consisting of three transmitters. Right: five-layer network consisting of 183 transmitters.

If the Triangle cells with-centre-node form the H-cell with-centre-node, as in Figure 4.11, its edge (X [m]) is given by Equation (4.11) and its area (A_{H2} [m^2]) by Equation (4.12).

$$X = \sqrt{3}L \tag{4.11}$$

$$A_{H2} = \frac{3\sqrt{3}x^2}{2} = \frac{9\sqrt{3}L^2}{2} \ [m^2] \tag{4.12}$$

4.4.1.3 Coverage Comparisons

According to Equations (4.5)-(4.14), the coverage of the with-centre-node and without-centre-node configurations can be compared as below. Equation (4.13) shows that the with-centre-node Hexagonal design covers a three times larger area than the design without-centre-node.

$$\frac{AH_2}{AH_1} = \frac{0.5\ (L^2)\ \cos(30°)}{1.5\ (L^2)\ \cos(30°)} = \frac{\frac{9\sqrt{3}L^2}{2}}{\frac{3\sqrt{3}L^2}{2}} = 3 \tag{4.13}$$

Similarly, for the Square design, the topology consisting of big Square cells (with-centre-node) covers an area two times larger than the one consisting of basic Square cells (without-centre-node). This is calculated by Equation (4.14).

$$\frac{AS_2}{AS_1} = \frac{2L^2}{L^2} = 2 \tag{4.14}$$

As it can be seen, if the centre node is added to the basic cells of the network the modified architectures can cover a larger area in both the Hexagonal and Square topologies. This means that by applying the calibration phase in the current measurement process, instead of using just the traditional transit time method, can result in a better coverage performance of the network. The next section compares node density in the networks, which is a crucial factor affecting the energy consumption.

4.4.2 Energy Consumption

In this section, it is shown that for bigger scales of underwater sensor networks, the extended coverage correlates with lower node density and consequently lower energy consumption. The methodology used here for evaluating the networks' energy consumption is that the size (number of nodes) of each network can be calculated, which is done in the tables. Following the tables, formulations describe the performance of each design.

4.4.2.1 Energy Consumption in Hexagon Topology

For the Hexagonal topology, Table 1 shows the size of the without-centre-node configuration once a layer is added the network.

Table 4.1: Hexagon Network without-centre-node

Number of layer (L)	Number of Hexagon Cells in each layer (H_1)	Number (coefficient) of Added Nodes/H-Cell	Total number of transmitter nodes in the network of L layers: without-centre-node (N_{TI})
1	1	7	7
2	6	4	7+(4)(6)=7+24=31
3	6+6	4-3	31+(4)(6)+(3)(6)=31+42=73
4	6+12	4-3	73+(4)(6)+(3)(6)+(3)(6)=73+60=133
5	6+18	4-3	133+(4)(6)+(3)(6)+(3)(6)+(3)(6)=133+78=211

In Table 4.1 (according to Figure 4.9), the reason that the numbers of H-cells in column two is broken and not expressed as one number is that the number of nodes which is added to the H-cells are not the same for all H-cells, e.g. some H-cells take four added nodes while some others take three (the third column, shows the number of nodes relating to the previous column). And this is why two different numbers are multiplied and added together in the fourth column. As an example, according to the second and thirds columns of the third layer-row, 4-3 means that six H-cells take four added nodes and six others take three. It should be mentioned that the redundant nodes are eliminated (as in the Figure 4.9) and are not counted.

Also, the reason that the whole multiplication is broken into smaller building blocks of six (e.g in four-layer row 12 in second column breaks into two blocks of 6, multiplied by the relevant coefficients (four or three)), is to derive a closed-form formula (sum form) for the total number of added nodes in each layer.

Now for deriving a closed-form formula for the total added nodes in each layer, according to the Table 4.1, the number of layers is considered as *L*, total added number of nodes in each layer as $N_{TI}(L)$, and the coefficients four and three as *a* and *b* respectively. The first layer always has seven nodes (including the node in centre of the H-cell which is the vertex of all the basic cells put together). The others obey the Equation (4.15), as below:

$$N_{TI}(L) = \begin{cases} 7, \ L = 1 \\ (a)(6) + (L-2)(b)(6) + NT_1(L-1), \ L > 1 \end{cases} while \ a = 4, b = 3 \quad (4.15)$$

The next goal is to show that networks that are built from with-centre-node H-cells have fewer number of nodes per unit area (node/m^2) and therefore a larger area is covered with fewer acoustic sensors which results in a less energy consumption. Likewise, as the deployment of the sensors in water is very difficult and expensive as well as their maintenance, the with-centre-node configuration also reduces the costs and hassles of the network effectively.

For the network of H-cells with-centre node, the total number transmitter nodes is demonstrated in Table 4.2.

Table 4.2: Hexagon network with centre node

Number of layer (L)	Total number of H-cells (H$_2$)	Total number of transmitter nodes in the network of L layers: with-centre-node (N$_{T2}$)
1	1	3
2	7	21
3	19	57
4	37	111
5	61	183

Equation (4.16) gives the number of transmitter nodes in with-centre-node Hexagonal configuration.

$$N_{T2}(L) = (3)H_2(L) \quad (4.16)$$

It is very important to say that the key difference in the with-centre-node configuration and the without-centre-node is that in the former only the centre nodes are transmitters but in the latter all nodes need to be a transmitter at least once for each round of the measurement. As the transmitter nodes are the main consumers of the power in an underwater environment, it is obviously shown that the with-centre-node configuration has considerably lower node density than the other design and therefore uses less power.

The first column, in the Table 4.2 (according to Figure 4.11), is the number of layer L, the second one represents the number of cells which is basically the addition of the previous cells in the second column in Table 4.1 and the third column represents the total number of transmitter nodes in with-centre-node topology.

In the following section the Square topology is evaluated and compared with Hexagonal design.

4.4.2.2 Energy Consumption in Square Topology

For the without-centre-node Square topology Table 4.3 and Equation (4.17) gives the number of transmitter nodes.

Table 4.3: Square network without-centre- node

Layer (L)	Total number of S-cells	Nodes added/each layer (S_1)	Total number of transmitter nodes in the network of L layers: without-centre-node (N_{S1})
1	1	(4)(1)=4	4
2	9	(4)(3)=12	16
3	25	(4)(5)=20	36
4	49	(4)(7)=28	64
5	81	(4)(9)=36	100

The number of added nodes is shown by S_1, the total number of nodes by N_{S1} and L is the number of layer.

$$S_1(L) = (4)(L + (L - 1)) \tag{4.17}$$

$N_{S1}(L)=S_1(L)+N_{S1}(L-1)$

For the network with big S-cell configuration, which is formed by with-centre-node basic cells, Table 4.4 and Equation (4.18) can yield the number of transmitters.

Table 4.4: Square network with centre node

Layer	Total number of cells	Total transmitter nodes in the network of L layers: with-centre-node (N_{S2})
1	1	1
2	9	5
3	25	13
4	49	25
5	81	41

$$N_{S2} = \text{roundup } \left(\frac{((L)+(L-1))^2}{2}\right) \tag{4.18}$$

In the Equation (4.18), N_{S2} is the total number of transmitter nodes in the network and L represents the number of layer.

4.4.2.3 Node Density

As it was mentioned earlier, node density gives the final benchmark for the network designs and indicates which network consumes less energy. In order to calculate this parameter for each of the above architecture designs, Equation (4.19) has been used in the simulations, which is simply the result of a division of the total number of transmitters at each layer by the total area of coverage achieved by adding each level of the layers. In Equation (4.19), as in all other equations in this Section, L represents the number of layers.

Node-density(L)=number of transmitter nodes(L) /A(L) (4.19)

As a result, the efficiency can be computed which is defined as the ratio of the *covered area* to *total number of nodes*. Thus in order to compare the efficiency of each two configurations, one's efficiency is divided by the other one. Equation (4.20) is an example explaining this comparison between the big Square topology, formed by with-centre-node configuration , and the basic Square cells topology, formed by without-centre-node configuration: (*area /nodes in Square with-centre node) / (area /nodes in Square without-centre node)*). In Equation (4.20), S_1 represents Square network without-centre node and S_2 represents Square network with-centre-cell.

$$\eta_{S2\_S1} = \frac{A_{S2}/A_{S1}}{Number\ of\ transmitters_{S2}/Number\ of\ transmitters_{S1}} \tag{4.20}$$

In Figures 4.12 to 4.15 network comparisons are depicted. The first graphical comparison is the networks' coverage depicted in Figure 4.12. Equation (4.21) is the one that has been used in the simulations which computes the area that has been covered with adding each layer to the network. In Equation (4.21), $A(L)$ [m^2] represents the area covered by L layers of network and A_{cell} [m^2] is the area of a single basic block cell forming the whole network.

$$A\ (L) = (A_{Cell}\ )\ (Total\ number\ of\ cells\ (L)) \tag{4.21}$$
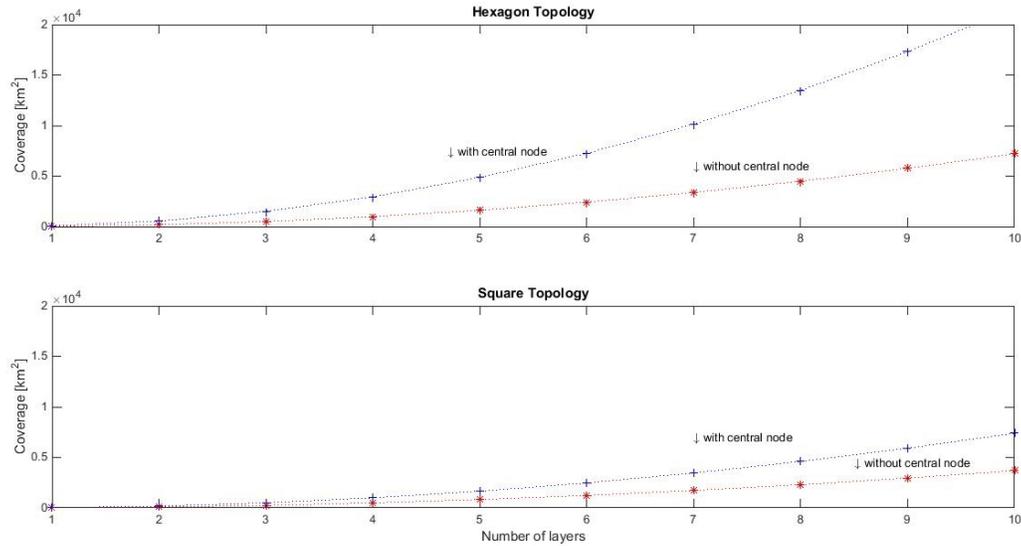
Figure 4.12: Coverage curves for with- and without-centre-node configurations. Top: Hexagon topology. Bottom: Square topology.

Figure 4.12 shows that with-centre-node configuration covers a larger area than without-centre-node configuration in both topologies. Also, the same number of layers in Hexagon topology covers a bigger area than the Square configuration.

Next is Figure 4.13 in which node density of the network is depicted by using Equations (4.20). Figure 4.13 shows that in Square topology the node density is slightly less than in the Hexagon configuration. This is an important indication that shows less power is consumed in with-centre-node Square type network, though, efficiency curves in Figures 4.14 and 4.15 show the effect of network design on power consumption more clearly.

103
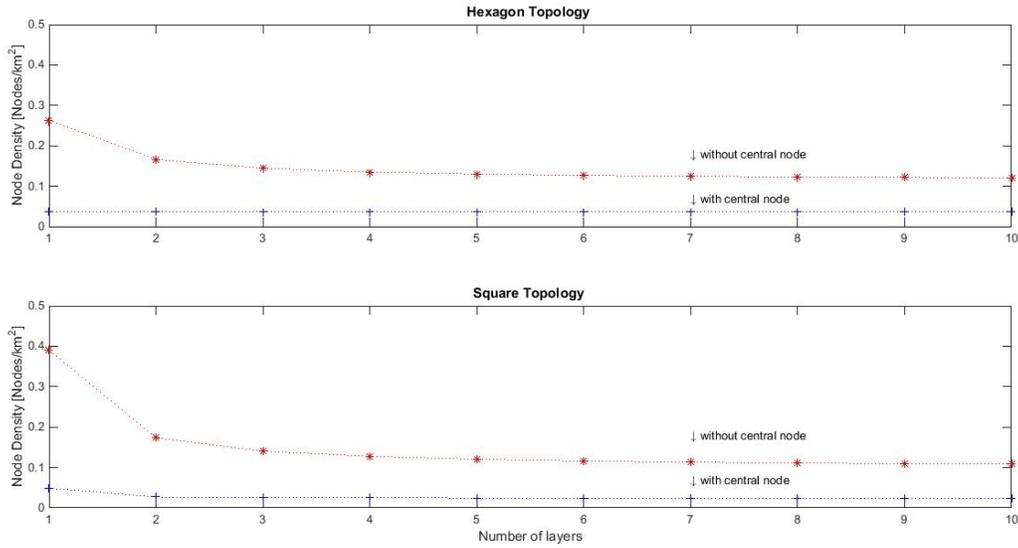
Figure 4.13: Node Density curves for with- and without-centre-node configurations. Top: Hexagon topology. Bottom: Square topology.

Figure 4.14 compares an important specification of the designed architectures that is the efficiency of the designs. Figure 4.14 is comparing the with-centre-node configuration's efficiency to without-centre-node's using Equation (4.20).
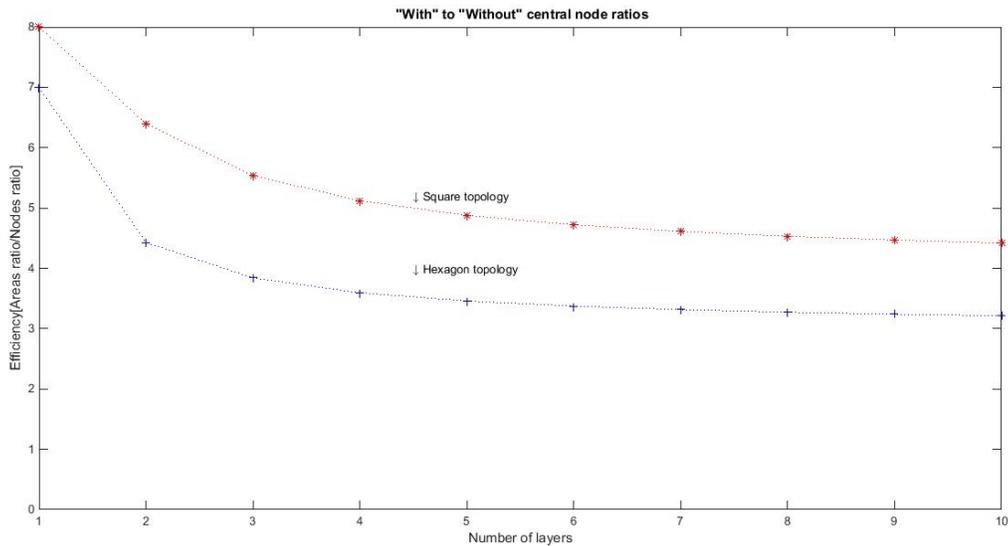
Figure 4.14: Efficiency ratio of with- to without-centre- node configuration.

As it can be seen in Figure 4.14, and according to the definition of efficiency that was previously mentioned, the efficiency of with-centre-node is better than without-centre-node design and by increasing the number of layers it converges to a constant number for both designs. Figure 4.14 also shows that the Square topology has a better efficiency than the Hexagon topology in general. Furthermore, it can be seen in Figure 4.14 that adding the centre node improves the efficiency of the network more than it does for the Hexagon configuration.

Figure 4.15 is another efficiency demonstration of Square design compared to the Hexagon each being in with- or without-centre configurations.
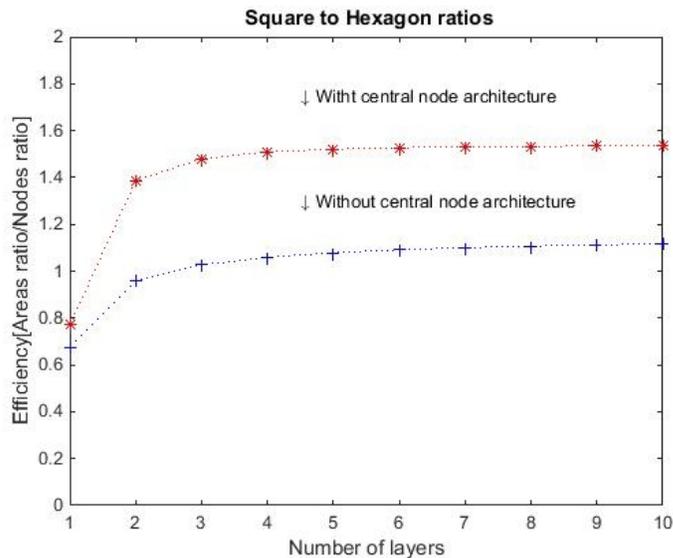
Figure 4.15: Efficiency ratio of Square to Hexagon topology.

Figure 4.15, shows that in both with- and without-centre-node configuration, Square topology has fewer nodes-per-area (especially in networks with more number of layers) and consequently is more efficient. Figure 4.15 actually confirms the results of the Figure 4.14.

In order to summarize and according to Figures 4.12-4.15 and Tables 4.1-4.4, which are presented above, it is concluded that networks of the with-centre-node type can cover a larger area at the sea with a fewer number of nodes than the without-centre-node configurations.

Consequently the new modified method that has been presented in this paper can yield a better efficiency result than the traditional transit time method.

4.4.3 Uncertainty

Lee et al. (Lee, Ho et al. 2014) conducted laboratory and field experiments using StreamPro ADCP (RDI 2008) in order to investigate the claimed data by the producer for the uncertainty of the velocity measurement. Their result shows $\pm4.55\%$ and $\pm5.24\%$ of uncertainties in the measurements done in laboratory and field conditions, respectively. The obtained deviations are greater than the uncertainty claimed by RDI for the instrument which is $\pm1\%$ or ±2 mm/s. Comparing the uncertainty values reported by Lee et al. with the RDI value shows that the environmental conditions of the measurement affect the uncertainty value. This difference might exist in the uncertainty analysis of the proposed method in this paper as well. In the conditions under which the proposed method has been developed (please see Appendix for more details), a measurement uncertainty of $\pm2\%$ (which is an acceptable uncertainty for instruments) in a long range (scale of kilometers) could be achievable. Therefore the uncertainty of the proposed technique in this paper is comparable with the uncertainty of measurements with ADCP. However, in practice and with different sets of instruments (similar to the ones reported for StreamPro by Lee et al.) the uncertainty might be different. Hence some other criteria are needed to be imposed on the instruments in order to obtain the same value for the velocity measurement uncertainty.

4.5 Conclusion

In this paper, UASNs have been designed for ocean current measurements and theoretical analyses of the designs have been provided. The measurement technique in the proposed networks is based on propagation of a sound wave through a horizontal layer of ocean and measurement of transit time. It uses the transit time method for obtaining the speed of the sound in water. The speed of sound, which is computed in the calibration phase, is considered to be constant for only a short period of time when the current measurement phase is active and also is only considered to be constant in a limited zone at the sea. The spatial distribution of the area where the speed of sound is considered constant (the constant speed zone extent) can vary depending on the required accuracy of the measurements. Having the underwater speed of sound and knowing the distances between the nodes (using GPS devices at each node) the ocean current can be measured.

The novel design of the UASNs is assessed in terms of energy consumption and the area they cover. It is shown that the modification of the transit time method helps in minimizing the energy consumption in the whole network as well as the increase in the area of coverage. Therefore the novel developed technique along with the new network designs would make a considerable progress in provision of accurate and sustainable measurement of the real-time ocean current data or other underwater environmental factors.

4.6 Apendix: Uncertainty Analysis

For a given value of $\pm 2\%$ for the uncertainty of the velocity measurements ($\frac{\Delta V}{V}\%$), Equations $A_{4.1}$-$A_{4.5}$ are used to calculate the limits for the uncertainty of the time measurement with the

instruments used in the measurement process. These calculations assure that with the equipments used in our design, the desired velocity measurement uncertainty is achievable. The time measured by the transducers in the proposed method is shown by t in (A$_{4.1}$). The distance between the transceivers is shown by d, C is the sound speed under water and v is the velocity of the water.

$$t = \frac{d}{c \pm v} \tag{A$_{4.1}$}$$

By differentiating the two sides, error in the time measurement (Δt) and then time uncertainty $(\frac{\Delta t}{t})$ is given:

$$(\Delta t = \left|\frac{\partial t}{\partial d}\right| \Delta d + \left|\frac{\partial t}{\partial V}\right| \Delta V + \left|\frac{\partial t}{\partial C}\right| \Delta C = \left|\frac{1}{c \pm v}\right| \Delta d + \left|\frac{\pm d}{(C \pm V)^2}\right| \Delta v + \left|\frac{-d}{(C \pm V)^2}\right| \Delta C) \tag{A$_{4.2}$}$$

$$\frac{\Delta t}{t} = \left|\frac{1}{d}\right| \Delta d + \left|\frac{\pm 1}{C \pm V}\right| \Delta v + \left|\frac{-1}{C \pm V}\right| \Delta c \approx \frac{\Delta d}{d} + \frac{\Delta V/V}{C \pm 1} + \frac{\Delta C}{C \pm V}$$

The second term in the right side of the equation (A$_{5.2}$) $(\frac{\Delta V/V}{C \pm 1})$ is small and negligible. The measurement error of the GPS device, used for measuring the location of the transducers, is considered to be 1.8m ($\Delta d = 1.8m$). If $t = \frac{d}{C \pm V} \sim \frac{3200}{1480 \pm 1} = 2.162162$, then provided that $C = \frac{d}{2} \frac{t_1 + t_2}{t_1 \cdot t_2}$ (measured by using transit time method to measure the C), ΔC can be calculated in (A$_{4.3}$) in which t_1 and t_2 indicate the upstream and downstream time measurement (Attarsharghi and Masek 2014).

$$\left(\Delta C = \left|\frac{d}{2} \cdot \frac{t_1 t_2 - t_2(t_1 + t_2)}{(t_1 t_2)^2}\right| \Delta t_1 + \left|\frac{d}{2} \cdot \frac{t_1 t_2 - t_1(t_1 + t_2)}{(t_1 t_2)^2}\right| \Delta t_2 + \left|\frac{1}{2} \frac{t_1 + t_2}{t_1 t_2}\right| \Delta d\right.$$

$$\left. = \left|\frac{d}{2} \cdot \frac{1}{(t_1)^2}\right| \Delta t_1 + \left|\frac{d}{2} \cdot \frac{1}{(t_2)^2}\right| \Delta t_2 + \left|\frac{1}{2} \frac{t_1 + t_2}{t_1 t_2}\right| \Delta d\right)\Bigg|_{devided \; by \; C = \frac{dt_1 + t_2}{2 \; t_1 \cdot t_2}, \frac{\Delta t_1}{t_1} = \frac{\Delta t_2}{t_2} = u_t}$$

$$\Delta C = \underbrace{\left|\frac{d}{2}\cdot\frac{1}{t_1}\right|\frac{\Delta t_1}{t_1} + \left|\frac{d}{2}\cdot\frac{1}{t_2}\right|\frac{\Delta t_2}{t_2}}_{u_t} + \underbrace{\left|\frac{1}{2}\frac{t_1+t_2}{t_1 t_2}\right|}_{\frac{1}{d}}\Delta d \tag{A$_{4.3}$}$$

$$\rightarrow t_1 = \frac{d}{C+V} = \frac{3200}{1480+1} = 2.160702, t_2 = \frac{d}{C-V} = \frac{3200}{1480-1} = 2.163624$$

Sampling interval of the analogue to digital converter of the microcontroller used in the experiment in Attarsharghi and Masek (Attarsharghi and Masek 2014) is 8μs which results in a time measurement uncertainty of $u_t = \frac{\Delta t_1}{t_1} = \frac{\Delta t_2}{t_2} \cong \frac{0.000008}{2.162162} \cong \frac{0.000008}{2.163624} \cong 3.7\mu$ (using transit time method). Thus, uncertainty in the process of sound speed measurement in the calibration phase is within the range given by (A$_{4.4}$).

$$\frac{\Delta C}{C} = u_C = u_t + u_d = \frac{0.000008}{2.162162} + \frac{1.8}{3200} = 3.7\mu + 0.0005625 = 0.000566 \tag{A$_{4.4}$}$$

Therefore, allowable uncertainty for time measurement with the given $u_V\% = 2\%$ is then calculated by (A$_{4.5}$)

$$\frac{\Delta t}{t} \approx \frac{\Delta d}{d} + \frac{\Delta V/V}{C/V\pm1} + \frac{\Delta C}{C\pm V} = 0.000563 + \frac{0.02}{1480} + 0.000566 = 0.001143 \tag{A$_{4.5}$}$$

Therefore, in order to have an uncertainty of lower than 2% in the velocity measurement, the measurement process should be able to measure the acoustic waves' traveling time with an uncertainty of $u_t \leq 0.11\%$. This margin for time measurement uncertainty is safe and achievable with the instruments used in the laboratory experiments. Actually we consider the sampling interval of the Analog to Digital Converter (ADC) in the microcontroller used in Attarsharghi (Attarsharghi 2016), which is ±8μs, as the error in the whole time measurement process. Although the actual ADC error would be ±4μs we add another ±4μs in order to include all other possible sources of errors for the time measurement such as the pulse per second inaccuracy of

the GPS device as well as the internal reference clock error of the microcontroller itself (however each of them might have an error in the scale of nanoseconds though).

Chapter 5: Conclusion

5.1 Summary and Significance of Design

This dissertation outlines problems associated with using traditional methods, including ADCP, floats and RADAR, for measuring the ocean current and offers new solutions. The popular methods are lacking in measuring the real-time near-surface current measurement because they are either measuring the current at a point or measuring the surface current. In order to overcome these problems, new designs of UASN for measuring the near-surface current are proposed which is at the same time helping with the energy saving objectives. Energy consumption and coverage maximization are the challenging issues in every underwater measurement systems. The novel method is based on transit time method and offers improving the energy consumption in the ocean measurement system with the details described in Chapter 4.

Two different types of topologies for the network has been proposed and their performance is compared to each other. One has a hexagonal shape and the other one has a square shape. If the application needs a smaller area of coverage, the hexagonal topology has a better performance according to the results explained in Chapter 4. However the topology with a square shape is more efficient at a larger scale. Both topologies are studied in two configurations each, 1) with a centre node, and 2) without a centre node. The configuration with-centre-node is the one that uses the novel proposed technique and is more efficient in terms of the energy consumption and thus is preferrable. In this configuration (with-centre-node) a calibration phase is determining the speed of sound in the desired region for a limited period of time, e.g. less than 15 minutes that the measurement process is performed. The other configuration uses the transit time method which leads to a more power consumption.

Hence, the most important improvement that is made, by using the proposed method in this study, is that a large area of ocean could be covered by a power optimized network of acoustic sensors in order to obtain real-time in-situe data of the current. The performance of the proposed network architectures have been evaluated by simulations and a comparison among the designs has been presented.

Also this research provides a new insight into practical complications of the underwater current measurement system (in Chapter 3). The multipath effect has also been considered and new techniques for transducer placement are proposed to reduce this effect. The proposed solutions have a significant impact on minimizing the energy consumption as well as the minimization of the computational error. In order to testify fundamental ideas a lab-scale prototype system has been designed and implemented with the result presented in Chapter 2. Cross correlation technique along with the transit time method has been used to measure the current in a flow tank. Positioning of the transducers along with the time-window technique, which have been applied in the experiment and explained in Chapter 2, proved to be effective in avoiding miscalculations due to the sound reflections and multipath effect.

5.2 Future Research

The presented thesis has laid a foundation for designing a wide area ocean current monitoring method. The research work was executed at a theoretical and simulation level with a limited lab based experimental study. Therefore, the future work shall focus on field validation. This part is highly demanding in terms of funding and ship time logistics and thus, a major research grant is needed to start this phase. Equally important would be the desire of the end users (public

agencies or private companies) to employ the current data. Only then this study and the related future work could become a game changer. Our method can be implemented in near future in the arctic region, where many studies related to global warming take place. Studies such as polar ice cap melting, iceberg flow and northern passage are a few of those that could largely benefit from our research.

Appendix 1- Definitions

GULF STREAM: A powerful and warm current originating in the Gulf of Mexico and following the shores of Newfoundland before passing through the Atlantic Ocean.

MEDDY: An expression to describe a large, clockwise-spinning, lens of water first discovered in a depth of 1000m off the Bahamas.

DOSITS: A website developed by the University of Rhode Island's (URI) Graduate School of Oceanography (GSO) in partnership with Marine Acoustics, Inc.(MAI) of Middletown, RI and is funded from the U.S. Office of Naval.

Appendix 2- Acronyms

ADCP	Acoustic Doppler Current Profilers
DOSTIS	Discovery of Sound in the Sea
FHL	Fluids Hydraulics Laboratory
GPS	Global Positioning System
n.d (in the references)	no date
NASA	National Aeronautics and Space Administration
NCOM	Naval Research Laboratory, Navy Coastal Ocean Model
NOAA	National Oceanic and Atmospheric
PPS	Pulse Per Second
PSD	Power Spectral Density
UASN	Underwater Acoustic Sensor Network

Apendix 3: Matlab codes and associated files

1- A sample of .env file feede into m.file for ssp plots

```
'UASnetwork, profile'              ! TITLE
3000.0                             ! FREQ (Hz)impact on ray step size!!
1                                  ! NMEDIA Dummy parameter
'CVW'                              ! SSP cubic Spline interpolation smooth.VACUUM above top .
51   0.0   176.0                   ! Dummy -Dummy -DEPTH of bottom (m)
0.0   1451.4  /                    ! Monthly varying from data downloaded from the Fisheries & Ocean Canada web site
20.0   1450.6  /
40.0   1445.5  /
60.0   1440.9  /
80.0   1445.4  /
100.0   1446.8  /
125.0   1447.7  /
150.0   1451.7  /
176.0   1454.4  /
'A*' 0.0
176.0   1459.80 0.0 1.8 0.8/
1                                  ! NSD
36.0 /                             ! SD(1:NSD) (m) for convergence zone p. 19 hardbook
308                                ! NRD
0.0 176.0  /                       ! RD(1:NRD) (m)
509                                ! NR
0.0 350.0 /                        ! R(1:NR ) (km)
'CB'                               ! 'R/C/I/S'
0                                  ! NBEAMS from computational ebook's formula.
-33.5  33.5 /                      ! ALPHA1, 2 (degrees) From Aquatrans beam pattern calculations
0.0  180.0  350.0                  ! STEP (m), ZBOX (m), RBOX (km)
```

2- A sample m.file for plotting ssp from Matlab-Bellhop toolbox (Porter 2011).

```
function plotssp( envfil )
% plotssp.m
% Plots the sound speed profile
% mike porter 3/2009

[ ~, ~, SSP, ~, fid ] = read_env( envfil, 'UASnetwork, profile' ); % read in the environmental file

%figure
hold on

for medium = 1 : SSP.NMedia
  hh = plot( real( SSP.raw( medium ).alphaR ), SSP.raw( medium ).z );
  set( hh, 'LineWidth', 2 );
  if ( any( SSP.raw( medium ).betaR ) )
    hh = plot( real( SSP.raw( medium ).betaR ), SSP.raw( medium ).z, 'r:' );
    set( hh, 'LineWidth', 2 );
  end
end

set( gca, 'YDir', 'Reverse' )   % because view messes up the zoom feature
%axis IJ
```

```
xlabel( 'Sound Speed (m/s)' )
ylabel( 'Depth (m)' )
```

Appendix 4: Quantified Comparison with other Literatures

A comparison between a network with data communication application and the network proposed in this dissertation is shown in Figure A_{4-1}.

Data used for energy consumption in the data communication network, is extracted from (Su, Venkatesan et al. 2015). Su et al. have shown in a graph the amount of energy in terms of Joules that is needed to transmit 50 packets per day versus the network size. Based on their graph, the bar graph in the right is showing the amount of energy used by the whole network for transmitting one packet. For the networks proposed in this thesis, in Figure A_{4-1} left, based on the lab-scale prototype, the energy consumption is equal to the power used to transmit the waves each time for a certain period of time per day. Base on the practical test, we can consider 35 Watts used by transmitter for 0.01 seconds multiplied by the number of transmitters in each configuration with different number of layers. As it is shown in the bar graphs, the configurations with-centre node that uses the proposed technique in this dissertation uses the least energy comparing to the ones with-out centre nodes as well as the network for data transmission. For more details on the number of transmitters in each layer please refer to tables 4.1-4 and the relevant equations.
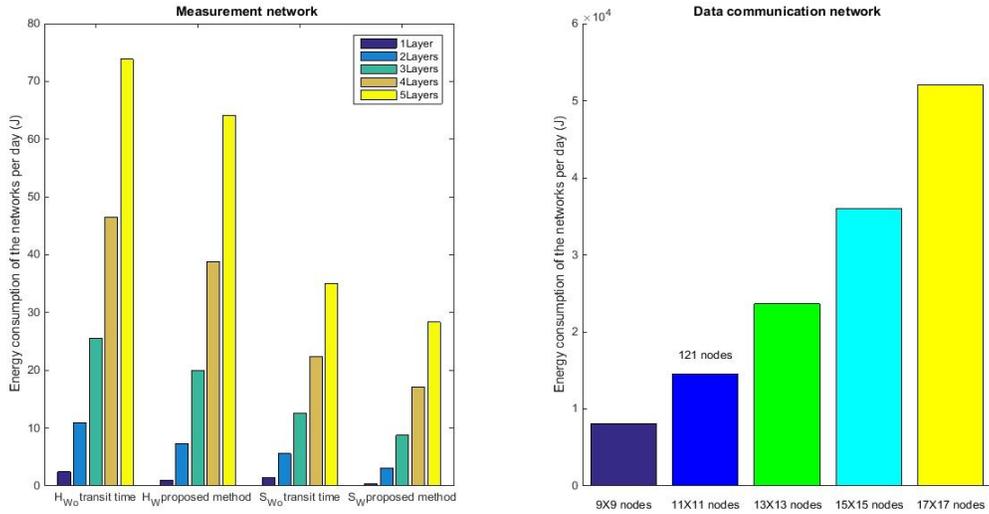
Figure A$_{4-1}$: Left: energy consumption of the network designed in this dissertation including all four designs. Without center node configurations, labeled on the figure, are those using traditional transit time method. Therefore in the left figure, networks for monitoring application using traditional method (transit time) and proposed method (in with-centre node configuration) are compared. Right: energy consumption of a network with different network sizes (in km^2) as labeled on the x-axis.

Comparison of the area that the networks can cover is also depicted in the Figure A$_{4-2}$. As it is shown, coverage of the networks with-centre node is larger among other networks.
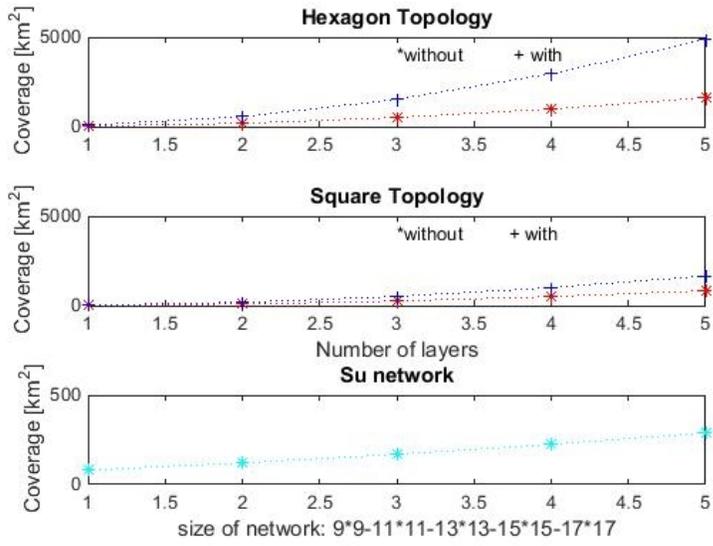
Figure A₄₋₂: Comparison between the area covered by the proposed networks in this research in Hexagonal and Square architecture versus the optimal network offered by Su et al. for data transmission.

Appendix 5: How Doppler Effect Can Interfere with Calculations

Here, it is shown though matlab simulation graphs that if the shift in frequency is large, error will be caused in calculations of the peak point of the cross correlation which represents the time of the travel of acoustic wave. Figure A_{5-1} shows the cross correlation results of a range of signals with various frequencies with a reference signal of 3KHz. Doppler shift may even cause more than one peak (e.g. if the signal being correlated has a higher frequency than 3.07 KHz).
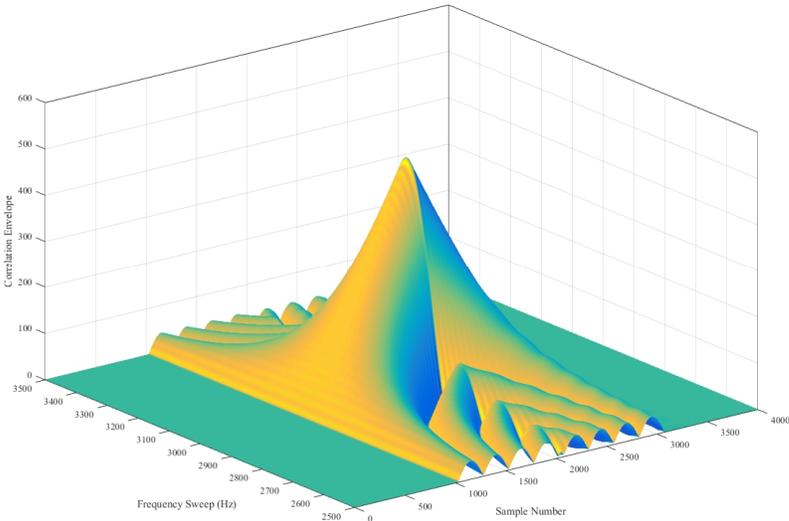

Figure A_{5-1}: 3-D result of cross-correlation of a 3KHz signal with signals of different frequencies.
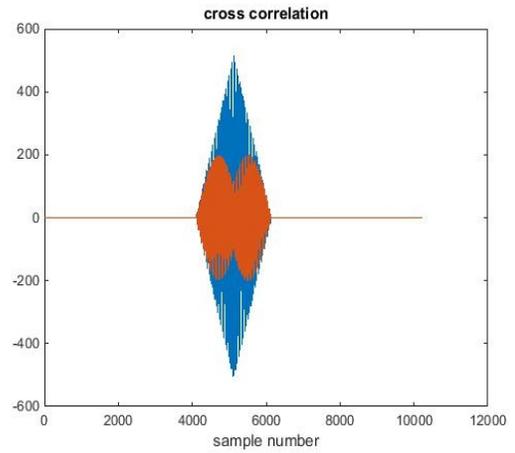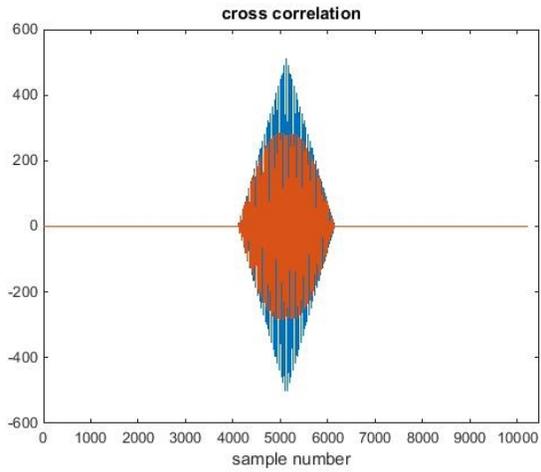
Figure A$_{5-2}$: 2-D result of cross-correlation of a 3KHz signal with: Left: a Doppler shift of 70 Hz (3.07KHz signal).

Right: a Doppler shift of 100 Hz (3.1 KHz signal).

Appendix 6: Multipath Effect Can Be Reduced Using Proper Transducer

Figure A_{6-1} and table T_{6-1} show how half-beamwidth (α) of transducer affects error. Figure A_{6-1} also shows how transceivers can be deployed underwater using anchor, and damper (represented by dashboard b and spring K).
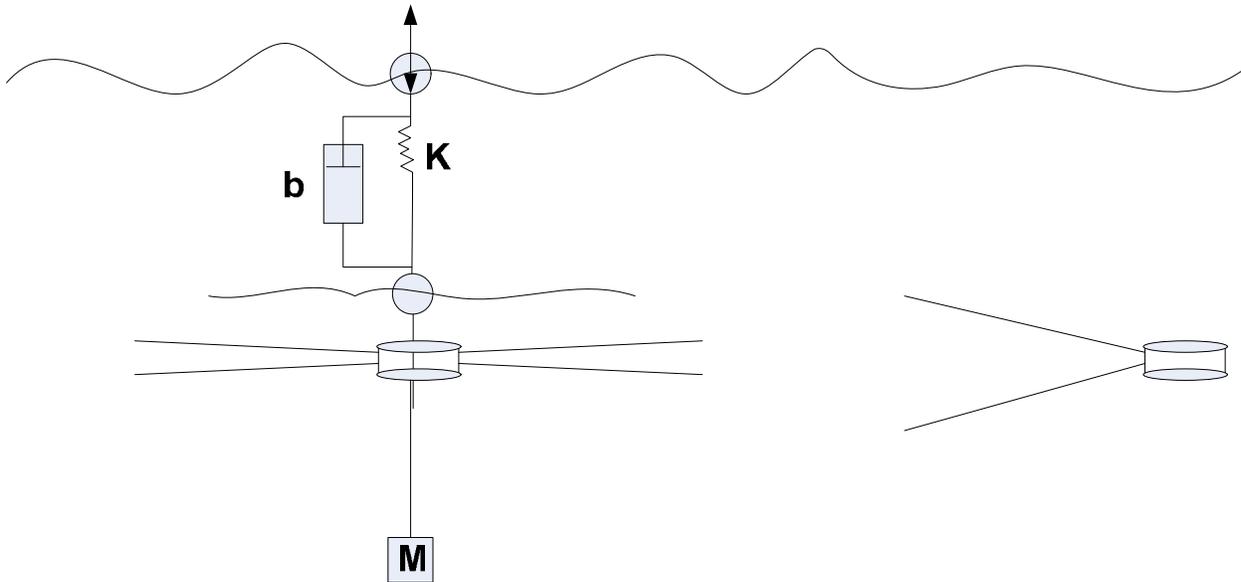
Figure A_{6-1}: How transceivers can be deployed underwater using anchor, and damper (represented by dashboard b and spring K).

Table T_{6-1}: Measurement error.

Angle (deg)	Angle (rad) ($\alpha<<,\sin \alpha \sim \alpha$)	Angle^2 (rad) * 100%
3	0.05	0.25%
6	0.1	1%

References

AquaTrans (2016).

Arduino-Uno (2013). "Uno microcontroller board and XbeeShield overview." from www.arduino.cc/en/Main/ArduinoBoardUno.

ATmega328P. from http://www.atmel.com/Images/doc8161.pdf.

Atmel (2016). "8-bit Atmel microcontroller, ATmega328P." from www.atmel.com/devices/atmega328.aspx.

Attarsharghi, S. (2016). "Design Criteria And Practical Insights Into An Underwater Current Measurement System Along With Simulation Results Of A Real-Case Scenario In The Northwest Atlantic Ocean." Journal of Ocean Technology **11**(1).

Attarsharghi, S. and V. Masek (2013). Modeling Underwater Multiple Path Effect on the Measurement of Water Velocity.

Attarsharghi, S. and V. Masek (2013). "Underwater Acoustic Driver/Amplifier Design and Implementation."

Attarsharghi, S. and V. Masek (2013A). "Modeling Underwater Multiple Path Effect on the Measurement of Water Velocity."

Attarsharghi, S. and V. Masek (2013B). Underwater Acoustic Driver/Amplifier Design and Implementation.

Attarsharghi, S. and V. Masek (2014). Ocean current monitoring via cross-correlation technique and node synchronisation. Oceans-St. John's, 2014, IEEE.

Baldev, R. (1999). Science and technology of ultrasonics, Narosa Publishing House.

Boyce, T. (2014). Introduction to Live Sound Reinforcement: The Science, the Art, and the Practice, FriesenPress.

Brekhovskikh, L. M. and I. U. r. P. Lysanov (2003). Fundamentals of ocean acoustics, Springer Science & Business Media.

Broström, G., A. Melsom, et al. (2009). "Iceberg modeling at met. no: Validation of iceberg model." Journal of Geophysical Research **99**(17): 3337-3350.

Casari, P. and M. Zorzi (2011). "Protocol design issues in underwater acoustic networks." Computer Communications **34**(17): 2013-2025.

Chapman, P., D. Wills, et al. (1999). "Visualizing underwater environments using multifrequency sonar." IEEE Computer Graphics and Applications(5): 61-65.

Chassignet, E. P., H. E. Hurlburt, et al. (2006). Ocean prediction with the hybrid coordinate ocean model (HYCOM). Ocean weather forecasting, Springer**: 413-426.

Cheng, Y., X. Li, et al. (2011). "SAR observation and model tracking of an oil spill event in coastal waters." Marine pollution bulletin **62**(2): 350-363.

Crabtree, M. A. (2009). "Industrial flow measurement." University of Huddersfield.

De Margerie, S. (1986). An operational iceberg trajectory forecasting model for the Grand Banks of Newfoundland, Environmental Studies Revolving Funds.

Deines, K. L. (1999). Backscatter estimation using broadband acoustic Doppler current profilers. Current measurement, 1999. proceedings of the ieee sixth working conference on, IEEE.

Dinehart, R. L. and C. Sacramento (2003). Spatial analysis of ADCP data in streams. Proceedings of the Federal Interagency Sediment Monitoring Instrument and Analysis Research Workshop.

Dinehart, R. L. and C. Sacramento (2003). Spatial analysis of ADCP data in streams. Proceedings of the workshop, Sediment Monitoring Instrument and Analysis Research, Flagstaff, AZ.

Dmitriev, N. Y. and A. V. Nesterov (2007). Iceberg Drift in the Barents Sea According to the Observation Data and Simulation Results. The Seventeenth International Offshore and Polar Engineering Conference, International Society of Offshore and Polar Engineers.

Dohan, K. and N. Maximenko (2010). "Monitoring ocean currents with satellite sensors." Oceanography **23**(4): 94.

DOSTIS (2016). "Discovery of Sound in the Sea." from http://www.dosits.org/galleries/scientist/interactive/?CFID=21009390&CFTOKEN=49147621w.

DSPcomm (2009). from http://www.dspcomm.com/products_aquatrans.html.

DSPcomm (2009). "AquaTrans – underwater acoustic dunking hydrophone transducer." from www.dspcomm.com/products_aquatrans.html.

Dushaw, B. A., W.; Beszcynska-Moller, A.; Brainard, R.; Cornuelle, B.; Duda, T.; Dzieciuch, M.; Forbers, A.; Freitag, L.; Gascard, J.-C.; Gavrilov, A.; Gould, J.; Howe, B.; Jayne, S.; Johannessen, O.; Lynch, J.; Martin, D.; Menemenlis, D.; Mikhalevsky, P.; Miller, J.; Moore, S.; Munk, W.; Nystuen, J.; Odom, R.; Orcutt, J.; Rossby, T.; Sagen, H.; Sandven, S.; Simmen, J.;

Skarsoulis, E.; Southall, B.; Stafford, K.; Stephen, R.; Vigness-Raposa, K.; Vinogradov, S.; Wong, K.; Worchester, P.; and Wunsch, C. (2009). A global ocean acoustic observing network.

Ehrhardt, M. (2015). Mathematical Modelling and Numerical Simulation of Oil Pollution Problems, Springer.

Eik, K. (2009). "Iceberg drift modelling and validation of applied metocean hindcast data." Cold Regions Science and Technology **57**(2): 67-90.

Eik, K. and O. T. Gudmestad (2010). "Iceberg management and impact on design of offshore structures." Cold Regions Science and Technology **63**(1): 15-28.

Erol-Kantarci, M., H. T. Mouftah, et al. (2011). "A survey of architectures and localization techniques for underwater acoustic sensor networks." IEEE Communications Surveys & Tutorials **13**(3): 487-502.

Etter, P. C. (2013). Underwater acoustic modeling and simulation, CRC Press.

Fisheries-and-Oceans-Canada (2015). Hydrographic data: data view.

Fofonoff, N. (1981). "The Gulf Stream." Evolution of Physical Oceanography: scientific surveys in honor of Henry Stommel: 112-139.

Fossette, S., N. F. Putman, et al. (2012). "A biologist's guide to assessing ocean currents: a review." Marine Ecology Progress Series **457**: 285-301.

Gill, T. P. (1965). The Doppler effect: an introduction to the theory of the effect, Academic Press.

Gough, P. and D. Hawkins (1998). A short history of synthetic aperture sonar. Geoscience and Remote Sensing Symposium Proceedings, 1998. IGARSS'98. 1998 IEEE International, IEEE.

Groen, J., J. Sabel, et al. (2001). "Synthetic aperture processing techniques applied to rail experiments with a mine hunting sonar." Proc. UDT Europe.

Guerra, F., P. Casari, et al. (2009). World Ocean Simulation System (WOSS): a simulation tool for underwater networks with realistic propagation modeling. Proceedings of the Fourth ACM International Workshop on UnderWater Networks, ACM.

Han, G., C. Zhang, et al. (2013). "A survey on deployment algorithms in underwater acoustic sensor networks." International Journal of Distributed Sensor Networks **2013**.

Heidemann, J., M. Stojanovic, et al. (2012). "Underwater sensor networks: applications, advances and challenges." Philosophical Transactions of the Royal Society of London A: Mathematical, Physical and Engineering Sciences **370**(1958): 158-175.

Hu, T. and Y. Fei (2010). "QELAR: a machine-learning-based adaptive routing protocol for energy-efficient and lifetime-extended underwater sensor networks." Mobile Computing, IEEE Transactions on **9**(6): 796-809.

Hunke, E. C. and D. Comeau (2011). "Sea ice and iceberg dynamic interaction." Journal of Geophysical Research: Oceans **116**(C5).

Jensen, F. B., W. A. Kuperman, et al. (2011). Computational ocean acoustics, Springer Science & Business Media.

Jha, D. K., T. A. Wettergren, et al. (2015). "Topology optimisation for energy management in underwater sensor networks." International Journal of Control(ahead-of-print): 1-14.

Jornet, J. M., M. Stojanovic, et al. (2010). "On joint frequency and power allocation in a cross-layer protocol for underwater acoustic networks." Oceanic Engineering, IEEE Journal of **35**(4): 936-947.

Joseph, A. (2013). Measuring ocean currents: tools, technologies, and data, Newnes.

Jurdak, R., C. V. Lopes, et al. (2004). "Battery lifetime estimation and optimization for underwater sensor networks." IEEE Sensor Network Operations **2006**: 397-420.

Jurdak, R., C. V. Lopes, et al. (2005). Programming Model for Supporting Complex Optimizations in Sensor Networks. Proc. Fourth International IEEE/ACM Conference on Information Processing in Sensor Networks (IPSN05) Work-in-Progress. Los Angeles, CA.

King, P., R. Venkatesan, et al. (2010). "Modeling a shallow water acoustic communication channel using environmental data for seafloor sensor networks." Wireless Communications and Mobile Computing **10**(11): 1521-1532.

Klemas, V. (2012). "Remote sensing of coastal and ocean currents: an overview." Journal of Coastal Research **28**(3): 576-586.

Lee, K., H.-C. Ho, et al. (2014). "Uncertainty in open channel discharge measurements acquired with StreamPro ADCP." Journal of Hydrology **509**: 101-114.

Liptak, B. G. (2003). Instrument Engineers' Handbook, Fourth Edi-tion: Volume 1, Process Measurement and Analysis, CRC Press.

Liu, Y., R. H. Weisberg, et al. (2011). "Tracking the Deepwater Horizon oil spill: A modeling perspective." Eos Trans. AGU **92**(6): 45-52.

Liu, Y. Y., R. H. Weisberg, et al. (2011). "Trajectory forecast as a rapid response to the Deepwater Horizon oil spill." <u>Monitoring and Modeling the Deepwater Horizon Oil Spill: A Record-Breaking Enterprise</u>: 153-165.

Lurton, X. (2002). <u>An introduction to underwater acoustics: principles and applications</u>, Springer Science & Business Media.

Lynnworth, L. and Y. Liu (2006). "Ultrasonic flowmeters: Half-century progress report, 1955–2005." <u>Ultrasonics</u> **44**: e1371-e1378.

Lynnworth, L. C. (2013). <u>Ultrasonic measurements for process control: theory, techniques, applications</u>, Academic press.

Mariano, A., V. Kourafalou, et al. (2011). "On the modeling of the 2010 Gulf of Mexico oil spill." <u>Dynamics of Atmospheres and Oceans</u> **52**(1): 322-340.

Mitra, U., S. Choudhary, et al. (2015). "Structured sparse methods for active ocean observation systems with communication constraints." <u>Communications Magazine, IEEE</u> **53**(11): 88-96.

NASA, N. A. a. S. A. (n.d.A.). "Ocean motion and surface currents: ship drift." from http://oceanmotion.org/html/gatheringdata/shipdrift.htm.

NASA, N. A. a. S. A. (n.d.B). "Ocean motion and surface currents." from http://oceanmotion.org.

NCOM (n.d.). "Naval Research Laboratory, Navy Coastal Ocean Model (NCOM)." from http://www7320.nrlssc.navy.mil/global_ncom/glb8_3b/html/index.html.

NOAA, n. d. A. (2013). "How does the ocean affect climate and weather on land?". from http://oceanexplorer.noaa.gov/facts/climate.html.

NOAA, n. d. B. (2013). "Currents and Marine Life." from http://oceanexplorer.noaa.gov/edu/learning/8_ocean_currents/activities/currents.html.

NOAA, N. O. a. A. A. (n.d. A). "Atlantic Oceanographic and Meteorological Laboratory." from www.aoml.noaa.gov.

NOAA, N. O. a. A. A. (n.d.B.). "How does the ocean affect climate and weather on land?". from http://oceanexplorer.noaa.gov/facts/climate.html.

NOAA, N. O. a. A. A. (n.d.C.). "Currents and Marine Life.". from http://oceanservice.noaa.gov/education/tutorial_currents.

NOAA, N. O. a. A. A. (n.d.D.). "Ocean surface current analyses – real time." from www.oscar.noaa.gov/index.html.

NOAA, N. O. a. A. A. (n.d.E.). "Deep ocean drifter.". from http://oceanservice.noaa.gov/education/tutorial_currents/06measure4.html.

NOAA, N. O. a. A. A. (n.d.F.). "Ocean surface current analyses – real time." from http://www.oscar.noaa.gov/index.html.

Ocean-Drifters (2016). from http://oceanservice.noaa.gov/education/tutorial_currents/06measure4.html.

Paduan, J. D. and H. Graber (1997). "Introduction to high-frequency radar: reality and myth." OCEANOGRAPHY-WASHINGTON DC-OCEANOGRAPHY SOCIETY- **10**: 36-39.

Paduan, J. D. and L. Washburn (2013). "High-frequency radar observations of ocean surface currents." Annual review of marine science **5**: 115-136.

Pandian, P. K., O. Emmanuel, et al. (2010). "An overview of recent technologies on wave and current measurement in coastal and marine applications." Journal of Oceanography and Marine Science **11**(1): 1-10.

Parallax (n.d.). XBee-PRO ZB S2B extended range module.

Partan, J., J. Kurose, et al. (2007). "A survey of practical issues in underwater networks." ACM SIGMOBILE Mobile Computing and Communications Review **11**(4): 23-33.

Peter M. D., T. R. (2001). "The Doubble Irony of the Meddy." from http://www.gso.uri.edu/maritimes/Back_Issues/00%20Fall/Text%20(htm)/meddy.htm.

Petrioli, C., R. Petroccia, et al. (2011). From underwater simulation to at-sea testing using the ns-2 network simulator. OCEANS 2011 IEEE-Spain, IEEE.

Pompili, D., T. Melodia, et al. (2009). "Three-dimensional and two-dimensional deployment analysis for underwater acoustic sensor networks." Ad Hoc Networks **7**(4): 778-790.

Porter, M. (2011). "The BELLHOP Manual and User's Guide." from http://oalib.hlsresearch.com/Rays/index.html.

Porter, M. B. (2011). "The bellhop manual and user's guide: Preliminary draft." Heat, Light, and Sound Research, Inc., La Jolla, CA, USA, Tech. Rep.

Rabiner, L. R. and B. Gold (1975). "Theory and application of digital signal processing." Englewood Cliffs, NJ, Prentice-Hall, Inc., 1975. 777 p. **1**.

Rajalakshmy, P. (2013). "Ultrasonic Flowmeter using Cross-Correlation Technique." International Journal of Computer Applications **66**(10).

RDI (2008). "StreamPro ADCP Guide, Teledyne RD Instruments, Poway, CA.". from www.otronix.com/kr/data/p03/StreamPro_ADCP_Operationa_Manual.pdf.

Rossby, T. (2016). "Visualizing and quantifying oceanic motion." Annual Review of Marine Science **8**: 35-57.

Rossby, T. and D. Webb (1970). Observing abyssal motions by tracking Swallow floats in the SOFAR channel. Deep Sea Research and Oceanographic Abstracts, Elsevier.

Schavemaker, P. and L. Van Der Sluis (2008). Electrical power system essentials, John Wiley & Sons.

Sedra, A. S. and K. C. Smith (2013). Microelectronic circuits: theory and applications, Oxford University Press.

Shin, K. and J. Hammond (2008). Fundamentals of signal processing for sound and vibration engineers, John Wiley & Sons.

SmartAtlanticAlliance (n.d.). "
Smart Atlantic buoy." from http://www.smartatlantic.ca/Home/.

Stefanov, A. and M. Stojanovic (2011). "Design and performance analysis of underwater acoustic networks." Selected Areas in Communications, IEEE Journal on **29**(10): 2012-2021.

Su, R., R. Venkatesan, et al. (2015). "An energy-efficient asynchronous wake-up scheme for underwater acoustic sensor networks." Wireless Communications and Mobile Computing.

Tan, C., Y. Cao, et al. (2012). Cross Correlation Based Dispersed Phase Velocity Profile Measurement of Two-Phase Pipe Flow. Instrumentation and Measurement Technology Conference (I2MTC), 2012 IEEE International, IEEE.

Texas-Instruments (2002). LM1875 Power Amplifier.

Tilak, S., N. B. Abu-Ghazaleh, et al. (2002). Infrastructure tradeoffs for sensor networks. Proceedings of the 1st ACM international workshop on Wireless sensor networks and applications, ACM.

Turnbull, I. D., N. Fournier, et al. (2015). "Operational iceberg drift forecasting in Northwest Greenland." Cold Regions Science and Technology **110**: 1-18.

Urick, J. R. (1983). Principles of underwater sound, McGraw-Hill, New York.

Urick, R. and O. U. S. PRINCIPLES (1983). MC-GRAW-HILL, NEW-YORK.

Valera, A., P. W. Lee, et al. (2009). Implementation and evaluation of multihop ARQ for reliable communications in underwater acoustic networks. OCEANS 2009-EUROPE, IEEE.

Vander Vorst, A., A. Rosen, et al. (2006). RF/microwave interaction with biological tissues, John Wiley & Sons.

Wang, Y., Y. Liu, et al. (2012). "Three-dimensional ocean sensor networks: A survey." Journal of Ocean University of China **11**(4): 436-450.

WHOI, W. H. O. I. (n.d.). "Moored profiler." from http://www.whoi.edu/page.do?pid=8415&tid=3622&cid=10978.

Wille, P. (2005). Sound images of the ocean: in research and monitoring, Springer Science & Business Media.

Wilson, W. D., R. Heitsenrether, et al. (2015). NOAA's Recent Field Testing of Current and Wave Measurement Systems–Part II. IEEE\ OES 11th Current, Waves and Turbulence Measurements Conference.

XB24-Z7WIT-004 (2016). XBee ZB Low-Power Module, Wire Antenna (XB24-Z7WIT-004).

Xiao, Y. (2010). Underwater acoustic sensor networks, CRC Press.

Xiaoyu, D., S. Lijuan, et al. (2013). "Coverage optimization Algorithm based on sampling for 3D underwater sensor networks." International Journal of Distributed Sensor Networks **2013**.

Zedel, L. and A. E. Hay (1999). "A coherent Doppler profiler for high-resolution particle velocimetry in the ocean: Laboratory measurements of turbulence and particle flux." Journal of Atmospheric and Oceanic Technology **16**(8): 1102-1117.

Zorzi, M., P. Casari, et al. (2008). "Energy-efficient routing schemes for underwater acoustic networks." IEEE Journal on Selected Areas in Communications **26**(9): 1754-1766.

Zuckerman, S. a. A., S. (2014). Advances in passive remote sensing of ocean currents and depths. IEEE International Geoscience and Remote Sensing Symposium IGARSS'2014.